Mitigating edge-localized modes on the Mega-Ampere Spherical Tokamak using resonant magnetic perturbations

Peter John Denner

Ph.D.

The University of York

Department of Physics

July 2012

Abstract

Type-I ELMy H-mode is planned to be the reference inductive operational scenario for ITER. However, unmitigated type-I ELMs would cause unacceptable damage to ITER's divertor, so a way of mitigating their effect must be found. This thesis focuses on the ergodization of the plasma edge using RMPs as a means of ELM control, and on related topics relevant to ergodic magnetic fields in MAST.

Chapter 1 provides an introduction to nuclear fusion and chapter 2 provides an overview of ELMs. In chapter 3, the effect of ergodic fields on L-mode temperature profiles is calculated. It is found that no flattening of the temperature profile should be expected in MAST plasmas, which is in agreement with experimental results.

In chapter 4, various metrics characterizing the degree of ergodicity in both L- and H-mode plasmas are calculated using vacuum modelling and compared with the amount of density pump-out observed experimentally in the those plasmas during the application of RMPs. The only parameter to show a correlation with the amount of density pump-out is the width of the laminar region. However, plasma response modelling provides a robust criterion for the occurrence of density pump-out that applies both to L- and H-mode plasmas.

In chapter 5, the results of lower single-null H-mode ELM mitigation experiments using $n = 4$ and $n = 6$ RMPs are presented. ELM mitigation is achieved and refuelling of plasmas that had begun to undergo pump-out is successfully demonstrated. Both ELM frequency and density pump-out are

found to increase with ELM coil current above a certain threshold.

An analysis of an ergodic magnetic field formed by a current sheet on a rational surface is presented in chapter 6. Various properties of this ergodic field are calculated and compared with experimental effects observed in the plasma. Some agreement is found between the experimental data and the modelling. Finally, a summary of the thesis is given in chapter 7.

Contents

List of Figures

Acknowledgments

First of all, I'd like to acknowledge the University of York and Culham Centre for Fusion Energy for giving me the opportunity to do a Ph.D. and for hosting me for three and a half years between them. I also have to thank York for my undergradute eduction, including a summer project with Roddy Vann that first set me down this path.

Secondly, I'd like to acknowledge all my fellow Ph.D. students, especially those with whom I've shared an office, for helping to make the time spent on my Ph.D. so enjoyable, even if writing this thesis has been possibly the least enjoyable experience of my life! Scientific writing doesn't come naturally to me, and I've struggled both to write well and to find the motivation to continue writing, so it's such a relief to have finally finished.

The most important acknowledgments have to go to my two supervisors Nigel Woolsey and Andrew Kirk. I'd like to take this opportunity to thank them for all their guidance, support and patience, which I know I've tested a few times! I'd also like to acknowledge Éric Nardon for his help and for writing the ERGOS code, which I've used extensively throughout my Ph.D. Without Éric, this thesis would be completely different. Acknowledgments also go to everyone else who has helped me during my Ph.D. There are too many people to mention them all by name.

I'd also like to acknowledge my parents, who have always supported my education, and my wonderful wife Diana, who has been nothing but supportive despite all the evenings I've spent working on this thesis instead of spending time with her.

Author's declaration

I declare that the work presented in this thesis, except where otherwise stated, is based on my own research and has not been submitted previously for a degree at this or any other university.

Some of the original work presented in chapter 4 has been published in the following journal article:

Denner P, Liu Y Q, Nardon E, Kirk A and the MAST team 2012 *Nucl. Fusion* **52** 054007

The MARS-F modelling presented in chapter 4 was carried out by Yueqiang Liu. Some other pieces of work presented in this thesis were carried out with assistance from Éric Nardon and Andrew Kirk.

References to other researchers have been given in the bibliography as appropriate.

Chapter 1

Introduction

1.1 Nuclear fusion

1.1.1 The need for nuclear fusion

Worldwide, there is growing concern about the consequences of anthropogenic climate change caused by greenhouse gas emissions. In addition, we are faced with the prospect of dwindling fossil fuel reserves and fears over energy security. Therefore, it is more important than ever to find a sustainable alternative energy source that can provide the base load of our electricity supply without releasing harmful emissions.

Renewable energy sources such as wind, solar, hydroelectric and wave power could play an important role in reducing carbon dioxide emissions but may not be able to supply all of our electricity needs. Wind and solar power are reliant upon the weather, so there are few locations where they can generate electricity all of the time, and most of these locations are situated far from large population centres where the electricity is needed [1]. In developed countries, where electricity demand is greatest, few suitable locations for hydroelectric power have not already been exploited [2]. The UK is comparatively well endowed with potential wave power, but even here, the amount of electricity that could feasibly be produced is only a small fraction of that from wind or solar power [3].

Nuclear fission does not directly produce any greenhouse gas emissions, but fears over safety and the disposal of large quantities of long-lived radioactive waste have led many governments to decide against building new nuclear fission plants. Nuclear fusion has the potential to produce large amounts of energy on demand from abundant deuterium and lithium while producing no greenhouse gas emissions (except in the construction of power plants). The only radioactive waste would consist of neutron-activated components of the reactor and residual tritium absorbed by the vessel walls. Compared to fission plants, there would be only small quantities of relatively short-lived radioactive waste.

1.1.2 Fusion reactions

Nuclear fusion is the process whereby light nuclei combine to form a heavier nucleus. If the binding energy of the products is greater than that of the reactants then the difference in binding energy will be carried off by the reactants as kinetic energy and can be used to generate electricity.

Nuclear fusion occurs in stars and is the process that converts matter to energy within stars. The fusion reaction that takes place in the Sun converts hydrogen to helium by the following process:

$$ {}^{1}_{1}\mathrm{H} + {}^{1}_{1}\mathrm{H} \rightarrow {}^{2}_{1}\mathrm{D} + \mathrm{e}^{+} + \nu_{\mathrm{e}} \tag{1.1} $$

$$ {}^{2}_{1}\mathrm{D} + {}^{1}_{1}\mathrm{H} \rightarrow {}^{3}_{2}\mathrm{He} + \gamma \tag{1.2} $$

$$ {}^{3}_{2}\mathrm{He} + {}^{3}_{2}\mathrm{He} \rightarrow {}^{4}_{2}\mathrm{He} + {}^{1}_{1}\mathrm{H} + {}^{1}_{1}\mathrm{H}. \tag{1.3} $$

The whole process converts six hydrogen nuclei (or simply protons) into a helium nucleus, two positrons, two neutrinos, two photons and two more hydrogen nuclei, and releases 26.7 MeV of energy. The cross-section for (1.1) is very small, which creates a bottle-neck and causes the chain of reactions to proceed very slowly, which is why it takes hundreds of millions or billions of years for stars to burn all of their hydrogen. Unfortunately, this means that this particular reaction is not a viable option for a fusion power plant. The fusion reaction with the most favourable cross-section is the deuterium–tritium (D–T) reaction

$$ {}^{2}_{1}\mathrm{D} + {}^{3}_{1}\mathrm{T} \rightarrow {}^{4}_{2}\mathrm{He} + {}^{1}_{0}\mathrm{n}, \tag{1.4}$$

which releases 17.6 MeV of energy.

In the centre-of-momentum frame, the magnitude of the momentum of the neutron must be equal to that of the helium nucleus. According to classical mechanics, this implies

$$m_{\mathrm{n}} v_{\mathrm{n}} = m_{\mathrm{He}} v_{\mathrm{He}}, \tag{1.5}$$

where m represents mass, v represents speed and the subscripts n and He refer to the neutron and the helium nucleus respectively. Therefore, the ratio of the (classical) kinetic energy of the neutron to that of the helium nucleus is given by

$$\frac{\frac{1}{2} m_{\mathrm{n}} v_{\mathrm{n}}^2}{\frac{1}{2} m_{\mathrm{He}} v_{\mathrm{He}}^2} = \frac{v_{\mathrm{n}}}{v_{\mathrm{He}}} = \frac{m_{\mathrm{He}}}{m_{\mathrm{n}}} \approx 4, \tag{1.6}$$

meaning that around $\frac{4}{5}$ of the energy released (i.e. 14.1 MeV) is carried off by the neutron and around $\frac{1}{5}$ (i.e. 3.5 MeV) by the helium nucleus. This helium nucleus should be confined within the D–T fuel for long enough to transfer most of its energy to the deuterium and tritium nuclei through collisions in order to help to keep the temperature of the fuel high enough for the reaction to continue. However, it should not be confined for so long that a significant amount of helium ‘ash’ accumulates in the D–T fuel. In a fusion reactor, the neutron would heat some fluid in a blanket surrounding the vessel. This heat would be used to boil water via a heat exchanger, and the steam produced would then be used to drive a turbine to generate electricity as in a conventional fossil fuel or nuclear fission power plant.

Deuterium occurs naturally in water. Tritium, however, is radioactive with a half-life of 12.3 years [4], so it does not occur naturally and must be bred from lithium through one of the following reactions:

$$ {}^{6}_{3}\mathrm{Li} + {}^{1}_{0}\mathrm{n} \rightarrow {}^{4}_{2}\mathrm{He} + {}^{3}_{1}\mathrm{T} \tag{1.7} $$

$$ {}^{7}_{3}\mathrm{Li} + {}^{1}_{0}\mathrm{n} \rightarrow {}^{4}_{2}\mathrm{He} + {}^{3}_{1}\mathrm{T} + {}^{1}_{0}\mathrm{n}. \tag{1.8} $$

In a fusion reactor, the neutrons for breeding tritium from lithium would be produced as a result of the fusion reactions (1.4) and would pass through a neutron multiplier before reaching the lithium in order to maximize the breeding ratio. The second of the two breeding reactions (1.8) has the advantage that an additional neutron is produced, which could go on to react with another lithium nucleus, thereby increasing the tritium yield. However, this reaction has the disadvantage that it is endothermic and so reduces the amount of energy available to be converted to electricity.

Every litre of water contains 33 mg of deuterium, while lithium is relatively abundant in the Earth's crust [4]. Theoretically, just 1 kg of deuterium and tritium is enough to power a 1 GW (electrical) power station for a day [5], so reserves of deuterium and lithium are large enough to meet the world's energy needs for thousands of years to come.

Since there is no chain reaction involved as there is with fission, there is no possibility of a runaway reaction and so nuclear fusion is inherently safe. During the operation of a fusion power plant, the walls of the reactor would be irradiated with neutrons and would therefore become radioactive. However, if low-activation materials were chosen for the reactor walls, after just 300 years, the radiotoxicity of this waste would be similar to that of ash in a coal-fired power station [6].

1.1.3 Plasma

Deuterium and tritium nuclei are both positively charged, so they must have enough energy to overcome their electrostatic repulsion in order for fusion to occur. Consequently, the cross-section for the reaction only becomes favourable for temperatures of at least 10 keV ($\sim 10^8$ K) [5]. At these temperatures, the deuterium and tritium atoms become ionized.

An ionized gas displays markedly different properties from a neutral gas. For example, a region with a higher concentration of ions than electrons, or *vice versa*, will result in an electric field, while motion of charged particles will generate electric currents and hence magnetic fields. Electric and magnetic fields can influence the behaviour of particles a long way from their source. Furthermore, the behaviour of particles can alter the electromagnetic fields, so certain feedback mechanisms can arise and lead to complex wave–particle phenomena. Therefore, ionized gases can be said to exhibit ‘collective behaviour’. The collective behaviour of an ionized gas is different from that of other fluids in that motion depends not only on local conditions via collisions but also on remote regions via long-range electromagnetic forces [7]. Note that gases need not be fully ionized in order to exhibit such behaviour.

In fact, the behaviour of ionized gases is so different from that of neutral gases that they are generally thought of as a distinct state of matter called ‘plasma’, which comes from the Greek word ‘$\pi\lambda\acute{\alpha}\sigma\mu\alpha$’, meaning ‘molded’ or ‘fabricated’ [7].

The net charge of a plasma is zero. In addition, electric fields within a plasma will cause the ions and electrons to counteract large-scale charge imbalances. Therefore, plasmas are electrically neutral over large scales, although they may consist of separate regions of positive and negative charge at small scales. This is known as quasi-neutrality. Note that this does not imply that large-scale electric fields in plasmas are negligible – due to the strength of electromagnetic forces, a very small charge imbalance will still result in a significant electric field.

A plasma is any quasi-neutral gas – whether fully or only partially ionized – that exhibits the collective behaviour described above [7]. As much as 99 % of all matter in the universe may be in the plasma state since stars and much of the the interstellar medium are plasmas. Examples of plasmas on Earth include lightning bolts, the aurorae borealis and australis, and the gas inside fluorescent light tubes and plasma television screens [8]. Plasmas also play an important role in many industrial processes such as metal cutting [9], microchip manufacturing, surface coating, and welding [10].

1.2 Plasma confinement methods

1.2.1 Introduction

Due to the very high temperatures of fusion plasmas, they cannot be confined by conventional containers because contact between the plasma and the walls of the container would both cool the plasma and damage the walls, and would also contaminate the plasma with impurities from the walls. The plasma that makes up the Sun is confined by its own gravitational field, but gravitational confinement is not viable on Earth because of the enormous quantities of matter that would be necessary. Most current fusion research focuses on one of two confinement methods: magnetic confinement and inertial confinement. This thesis focuses on the magnetic confinement method.

Inertial confinement fusion (ICF) involves irradiating a frozen pellet of deuterium and tritium with high-power lasers, high-energy ions or soft X-ray radiation. This causes the outer layer of the pellet to vaporize, which compresses the core of the pellet through momentum balance. This results in the core becoming dense enough to trap neutrons. The pellet is then heated by the convergence of shock waves at its centre, becoming hot enough for fusion to occur.

1.2.2 Magnetic confinement fusion

In magnetic confinement fusion (MCF), charged particles are constrained to gyrate about magnetic field lines. The equation of motion for a charged particle in a magnetic field is

$$m\frac{d\boldsymbol{v}}{dt} = q\boldsymbol{v} \times \boldsymbol{B}, \tag{1.9}$$

where m, $\boldsymbol{v}$ and q are the mass, velocity and charge of the particle respectively, and $\boldsymbol{B}$ is the magnetic field vector.

Assuming that the magnetic field is uniform, homogeneous and parallel to the z-axis, decomposing the velocity into its x-, y- and z-components gives

$$m\frac{dv_x}{dt} = qv_yB \tag{1.10}$$

$$m\frac{dv_y}{dt} = -qv_xB \tag{1.11}$$

$$m\frac{dv_z}{dt} = 0. \tag{1.12}$$

Assuming the magnetic field is constant in time, differentiating (1.10) and (1.11) with respect to time leads to

$$m\frac{d^2v_x}{dt^2} = q\frac{dv_y}{dt}B \tag{1.13}$$

$$m\frac{d^2v_y}{dt^2} = -q\frac{dv_x}{dt}B. \tag{1.14}$$

Substituting (1.11) into (1.13) and (1.10) into (1.14) produces

$$\frac{d^2v_x}{dt^2} = -\frac{q^2B^2}{m^2}v_x \tag{1.15}$$

$$\frac{d^2v_y}{dt^2} = -\frac{q^2B^2}{m^2}v_y. \tag{1.16}$$

These are the equations of simple harmonic motion.

The equations require some initial conditions in order to yield a solution. The initial conditions used here are that when $dv_x/dt = 0$, $v_x = \pm v_\perp$, and likewise for v_y, and that when $t = 0$, $v_x = 0$ and $v_y = v_\perp$. Solving the equations using these initial conditions gives

$$v_x = -v_\perp \sin \omega_\mathrm{c} t \tag{1.17}$$

$$v_y = v_\perp \cos \omega_\mathrm{c} t, \tag{1.18}$$

where $v_\perp^2 = v_x^2 + v_y^2$ is the magnitude of the velocity of the particle perpendicular to the magnetic field and $\omega_\mathrm{c} = qB/m$ is the angular frequency at which the particle gyrates about the z-axis, known as the cyclotron frequency or gyro-frequency.

Integrating (1.17) and (1.18) with respect to time leads to

$$x - x_0 = \rho_\mathrm{L} \cos \omega_\mathrm{c} t \tag{1.19}$$

$$y - y_0 = \rho_\mathrm{L} \sin \omega_\mathrm{c} t, \tag{1.20}$$

where $\rho_\mathrm{L} = v_\perp/\omega_\mathrm{c}$ is the radius of the particle's orbit about the z-axis, known as the Larmor radius, and (x_0, y_0) is the location of the centre of the particle's orbit, known as the gyro-centre.

Equations (1.10) and (1.11) show that a charged particle in a uniform, homogeneous magnetic field is free to move arbitrarily in the direction of the magnetic field; equations (1.19) and (1.20) show that the particle is constrained to orbit magnetic field lines with radius ρ_L and angular frequency ω_c in the plane perpendicular to the magnetic field. This principle forms the basis of magnetic confinement.

1.3 Tokamaks

Early MCF devices consisted of linear magnetic fields. In such devices, the ions and electrons are constrained to gyrate about field lines but can move freely along the field lines. Magnetic mirrors are placed at either end of the device to prevent the particles from leaving via the ends. However, it was found that particles travelling with sufficient velocity parallel to the magnetic field still left the device.

The logical next step was to join the ends of the device together to form a torus in order to prevent end losses. In section 1.2, the electric field was neglected and it was assumed that the magnetic field was homogeneous and linear. In these toroidal devices, the magnetic field is both inhomogeneous and curved, which causes the ions and electrons to feel additional forces $\boldsymbol{F}$ as they travel along the field lines. Therefore, the equation of motion becomes

$$m\frac{d\boldsymbol{v}}{dt} = \boldsymbol{F} + q\boldsymbol{v} \times \boldsymbol{B} \tag{1.21}$$

and decomposing the velocity into its x-, y- and z-components now gives

$$m\frac{dv_x}{dt} = F_x + qv_yB \tag{1.22}$$

$$m\frac{dv_y}{dt} = F_y - qv_xB \tag{1.23}$$

$$m\frac{dv_z}{dt} = F_z. \tag{1.24}$$

Assuming the additional forces are constant in time, (1.13) and (1.14) are still valid. Substituting (1.23) into (1.13) and (1.22) into (1.14) produces

$$\frac{d^2v_x}{dt^2} = \frac{qB}{m^2}F_y - \frac{q^2B^2}{m^2}v_x \tag{1.25}$$

$$\frac{d^2v_y}{dt^2} = -\frac{qB}{m^2}F_x - \frac{q^2B^2}{m^2}v_y. \tag{1.26}$$

Solving these equations gives

$$v_x = \frac{F_y}{qB} - v_\perp \sin\omega_\mathrm{c}t \tag{1.27}$$

$$v_y = -\frac{F_x}{qB} + v_\perp \cos\omega_\mathrm{c}t. \tag{1.28}$$

This shows that, in addition to the circular motion of the particles about magnetic field lines, they drift across the field lines with a drift velocity $\boldsymbol{v}_\mathrm{D}$ given by

$$\boldsymbol{v}_\mathrm{D} = \frac{F_y}{qB}\boldsymbol{i} - \frac{F_x}{qB}\boldsymbol{j} = \frac{\boldsymbol{F} \times \boldsymbol{B}}{qB^2}. \tag{1.29}$$

Equation (1.29) shows that forces that are independent of charge cause oppositely charged particles to drift in opposite directions, while forces that are proportional to a particle's charge, such as the force due to an electric field $\boldsymbol{E}$, which is equal to $q\boldsymbol{E}$, cause all charged particles to drift in the same direction.

The forces due to the inhomogeneity and curvature of the magnetic field, which the particles feel as they travel along the field lines, are independent of charge, so they cause the ions and electrons to drift in opposite directions, leading to charge separation, which produces an electric field. The force due to this electric field is proportional to a particle's charge, so it causes both ions and electrons to drift in the same direction and leave the device.

There are distinct types of toroidal device and they differ from each other in the way that they address the issue of particle drifts. Arguably the most developed type of toroidal device is the tokamak. It was invented in the USSR and its name comes from the Russian for 'toroidal chamber with magnetic coils'. In a tokamak, a current is passed through the plasma in the toroidal direction (the long way around the torus), which generates a secondary magnetic field in the poloidal direction (the short way around) in addition to the dominant externally applied toroidal field, resulting in a helical magnetic field. This gives particles travelling along field lines a poloidal component to their motion and prevents the charge separation that would otherwise produce an electric field and consequently cause a loss of confinement.

Figure 1.1 shows a cut-away diagram of a tokamak. The helical magnetic field lines can be seen in the plasma. The coils that produce the toroidal field are also shown, along with the transformer used to drive the plasma current that produces the poloidal field.

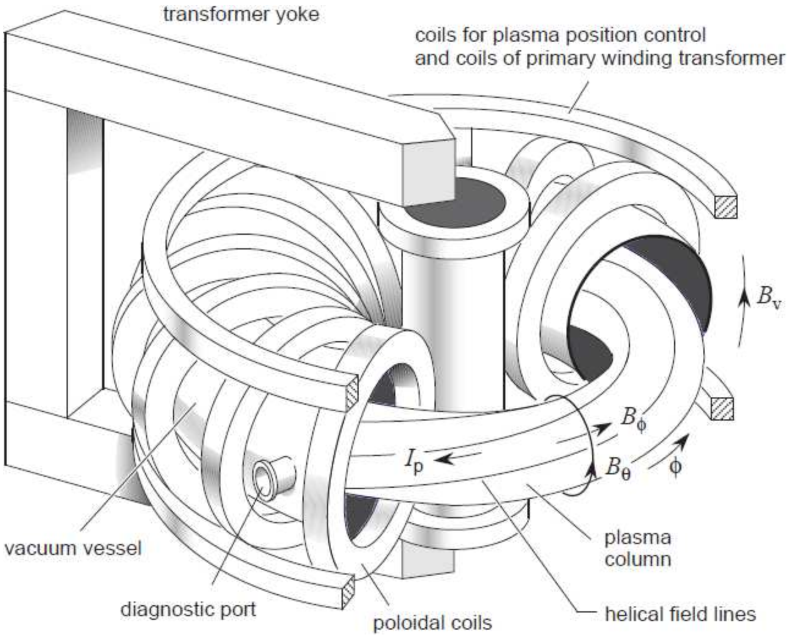

Figure 1.1 Cut-away diagram of a tokamak showing the plasma with helical magnetic field lines, the toroidal field coils and the transformer. ϕ and θ represent the toroidal and poloidal directions respectively. From [11].

The two other common forms of toroidal device are stellarators and reversed-field pinches. Reversed-field pinches differ from tokamaks in that the dominant magnetic field is the poloidal field generated by the plasma current, rather than the externally applied toroidal field. In stellarators, both the toroidal and poloidal fields are externally applied and no plasma current is required.

The next step for tokamak research will be ITER, which is Latin for 'the way' and is currently being built at Cadarache in Provence, France. It is planned to produce ten times more power (thermal, not electrical) than is required to heat the plasma, and to demonstrate the feasibility of sustained nuclear fusion as a potential power source. Figure 1.2 shows a cut-away diagram of ITER. The person at the bottom gives an idea of its scale. It will be around twice as big in linear dimensions as the Joint European Torus (JET), which is currently the largest tokamak in the world. A demonstration fusion reactor that would produce significant amounts of electricity is likely to be around 15 % bigger again in linear dimensions.

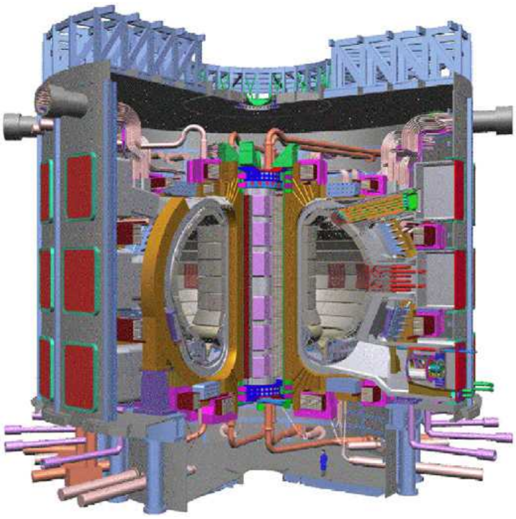

Figure 1.2 Cut-away diagram of the ITER tokamak showing, among other components, the vacuum vessel, the toroidal field coils and the large cryostat that surrounds the device. From [12].

1.4 The Mega-Ampere Spherical Tokamak

The Mega-Ampere Spherical Tokamak (MAST) at the Culham Centre for Fusion Energy (CCFE) in Oxfordshire, UK, is an innovative concept that has a more spherical shape than a conventional tokamak. This allows it to achieve better confinement for a given magnetic field strength and makes it more economical than a conventional tokamak. However, the compact shape of a spherical tokamak means that there is no space for shielding around the centre-column to protect it from the neutron damage that would occur in a large tokamak with a significant amount of fusion reactions. Suggestions for overcoming this drawback include replacing the damaged centre-column regularly, quickly retracting the centre-column after plasma start-up, and substituting the centre-column for a plasma arc. These suggestions have not yet been shown to be feasible. Figure 1.3 shows a MAST plasma.

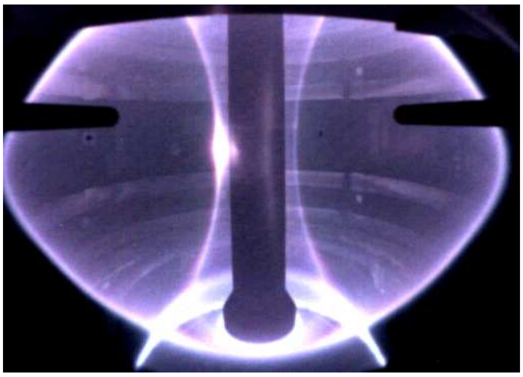

Figure 1.3 View inside MAST taken with visible light, showing the spherical shape of MAST plasmas. It can be seen that there is little space between the plasma and the centre-column.

Aspect ratio is a measure of how spherical or torus-shaped a tokamak is, and is defined as the ratio of a torus's major radius (the distance from the vertical axis that passes through the hole in the middle of the torus) to its minor radius (the distance from the circular axis that passes through the middle of the plasma). Figure 1.4 (*a*) illustrates the definition of the major and minor radii of a torus. MAST has an aspect ratio of approximately 1.3, whereas a typical conventional tokamak has an aspect ratio around 3 or 4 [13]. JET and ITER both have an aspect ration of approximately 3. The difference in shape between a spherical tokamak and a conventional tokamak is shown in figure 1.4 (*b*).

In addition to its more spherical shape, the name also reflects the fact that MAST plasmas can have a plasma current I_{P} of up to $I_{\mathrm{P}} \approx 1\,\mathrm{MA}$, which is higher than some larger conventional tokamaks. Other parameters include a toroidal field $B_\phi \approx 0.5\,\mathrm{T}$, major radius $R_0 \approx 1\,\mathrm{m}$ and minor radius $a \approx 0.7\,\mathrm{m}$ at the midplane, which is the horizontal plane through the centre of the plasma. MAST plasmas can be highly shaped with the minor radius being considerably greater in the vertical direction than in the horizontal direction for some plasmas. This elongation is beneficial for plasma confinement.

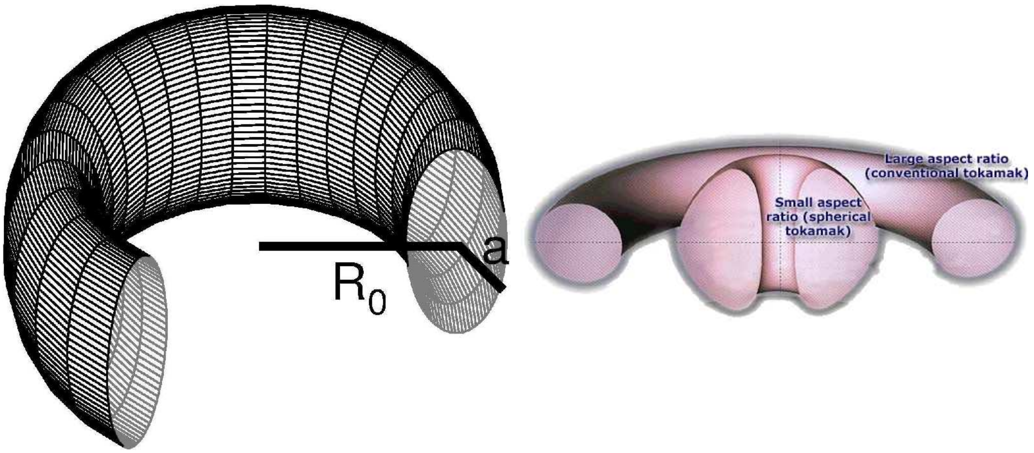

(a) *(b)*

Figure 1.4 (a) The major radius R_0 and minor radius a of a torus. From [14]. (b) The difference in aspect ratio between a spherical tokamak and a conventional tokamak (courtesy of CCFE).

Chapter 2

Edge-localized modes

2.1 High-confinement mode

In the majority of magnetic confinement devices, when the heating power exceeds a certain threshold, an abrupt bifurcation to a higher-confinement regime occurs, where 'confinement' refers to the length of time that particles or energy remain within the plasma before escaping. This regime is called high-confinement mode (H-mode) and the original lower-confinement regime is known as low-confinement mode (L-mode). In conventional (large aspect ratio) tokamaks, the confinement in H-mode is approximately twice that in L-mode [15]. In spherical tokamaks, the difference in confinement is somewhat less.

The transition from L-mode to H-mode, known as the L–H transition, coincides with the formation of an edge transport barrier (a barrier to particles and heat leaving the plasma) and a rapid increase in the pressure gradient in the edge of the plasma [15]. The pressure gradient in the plasma core changes little, but the pressure profile in the core is raised due to the increase in the edge pressure gradient. For this reason, the region over which this increase in the pressure gradient takes place is known as the pedestal. This pedestal is shown in figure 2.1 along with L- and H-mode pressure profiles.

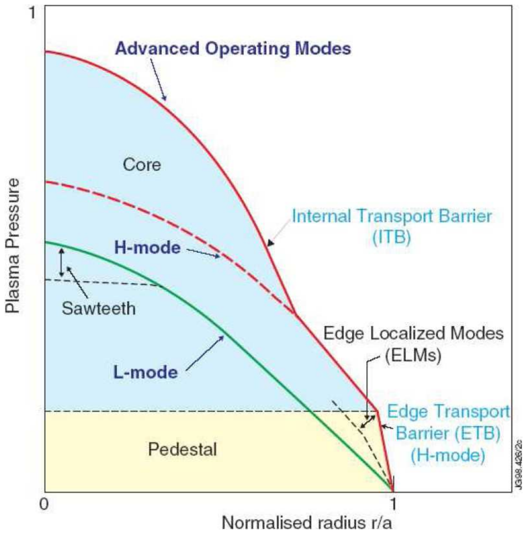

Figure 2.1 Plot of different pressure profiles showing the edge transport barrier and the difference between L- and H-mode. From [11].

The underlying mechanism behind the L–H transition is poorly understood. However, it is believed to be caused by large flow shears in the plasma edge that tear apart turbulent eddies. In L-mode, this turbulence increases transport, so suppressing this turbulence would improve confinement. The particle flow velocity perpendicular to the magnetic field is related to the radial electric field, and the L–H transition is associated with changes in the gradient of the electric field. In addition, fluctuations in the edge density have been observed to decrease suddenly at the onset of H-mode, which supports the theory that turbulence is being suppressed [15].

2.2 Description of ELMs

In H-mode, the pedestal height increases steadily, typically over the order of milliseconds or tens of milliseconds, until an instability known as an edge-localized mode (ELM) is triggered [16]. ELMs are short, regular perturbations of the plasma edge that briefly degrade the edge transport barrier, leading to the ejection of particles and energy from the plasma [17] and a corresponding rapid drop in the pedestal height. Then the ELM cycle begins again as the pedestal height steadily increases once more.

In MAST plasmas, an axisymmetric poloidal field null, i.e. a point where the poloidal magnetic field strength is zero, is formed in order to direct the particle and energy exhaust from the plasma onto a plasma-facing component called the divertor. In what are known as single-null plasmas, only one such poloidal null is formed, usually at the bottom of the plasma. In double-null plasmas, two such poloidal nulls are formed – one at the bottom and one at the top of the plasma. If there are field lines connecting the upper and lower nulls then the plasma is known as a connected double-null plasma. Figure 1.3 depicts such a connected double-null plasma, of which the lower null is visible as the point at the bottom of the plasma on either side of the centre-column where the plasma outlines cross. Poloidal field nulls are also identified as X-points.

The particles ejected during ELMs cause large heat fluxes to the divertor and to the vessel walls [16]. The amount of energy ejected from the plasma is proportional to the amount of energy stored in the pedestal region, which increases with machine size. Therefore, the power load on the plasma-facing components could cause serious damage in a large, high-power tokamak like ITER [18].

Despite the problem that ELMs present, there is also a positive side to them – in ELM-free H-mode plasmas, impurities are very well confined, and such plasmas normally terminate due to the build-up of impurities [18]. ELMs increase the impurity exhaust and prevent the accumulation of impurities in the plasma [16].

2.3 Magnetohydrodynamics

2.3.1 Background

Kinetic and gyro-kinetic (where the gyratory motion of particles around field lines is averaged over their gyro-orbits [19]) models are intractable analytically and require computationally expensive codes to solve numerically. Therefore, a simpler model, known as magnetohydrodynamics (MHD) is often used instead [11]. MHD describes plasma as a single magnetic fluid [20]. MHD describes a range of plasma instabilities, including peeling–ballooning modes, which are thought to be the cause of ELMs.

2.3.2 Mass continuity

The rate of change of mass within a fixed volume V is given by

$$\int_V \frac{\partial \rho}{\partial t} dV, \tag{2.1}$$

where ρ is the mass density.

The rate at which mass flows through the surface S enclosing the volume V is given by

$$\oint_S \rho \boldsymbol{v} \cdot d\boldsymbol{S}, \tag{2.2}$$

where $\boldsymbol{v}$ is the flow velocity.

Applying the divergence theorem yields

$$\oint_S \rho \boldsymbol{v} \cdot d\boldsymbol{S} = \int_V \boldsymbol{\nabla} \cdot (\rho \boldsymbol{v})\, dV. \tag{2.3}$$

Since $d\boldsymbol{S}$ always points outwards from the volume V, $\boldsymbol{v} \cdot d\boldsymbol{S}$ must be positive where mass leaves the volume and negative where mass enters. This means that (2.2) is the rate at which mass leaves the volume minus the rate at which it enters. Provided there are no sources or sinks of mass inside the volume, the rate of increase in mass within the volume must be equal to the rate at which mass enters minus the rate at which it leaves, i.e.

$$\int_V \frac{\partial \rho}{\partial t} dV = -\oint_S \rho \boldsymbol{v} \cdot d\boldsymbol{S} = -\int_V \boldsymbol{\nabla} \cdot (\rho \boldsymbol{v})\, dV. \tag{2.4}$$

This integrand is arbitrary. Therefore,

$$\frac{\partial \rho}{\partial t} = -\boldsymbol{\nabla} \cdot (\rho \boldsymbol{v}) = -\rho \boldsymbol{\nabla} \cdot \boldsymbol{v} - (\boldsymbol{v} \cdot \boldsymbol{\nabla})\, \rho. \tag{2.5}$$

This is the mass continuity equation [21].

2.3.3 Force balance

The equation of motion for a charged particle in an electromagnetic field is

$$m \frac{d\boldsymbol{v}}{dt} = q\left(\boldsymbol{E} + \boldsymbol{v} \times \boldsymbol{B}\right), \tag{2.6}$$

This equation also describes a macroscopic collisionless fluid consisting of identical particles if m and $\boldsymbol{v}$ instead represent the mass of the fluid and the flow velocity respectively [21]. However, when (2.6) refers to an entire fluid, the time derivative is not very convenient because it describes the time evolution of the flow velocity in a reference frame moving with the fluid.

In Cartesian co-ordinates, $\boldsymbol{v} = \boldsymbol{v}(x, y, z, t)$. Therefore,

$$\frac{d\boldsymbol{v}}{dt} = \frac{\partial \boldsymbol{v}}{\partial t} + \frac{\partial \boldsymbol{v}}{\partial x}\frac{dx}{dt} + \frac{\partial \boldsymbol{v}}{\partial y}\frac{dy}{dt} + \frac{\partial \boldsymbol{v}}{\partial z}\frac{dz}{dt} = \frac{\partial \boldsymbol{v}}{\partial t} + (\boldsymbol{v} \cdot \boldsymbol{\nabla})\, \boldsymbol{v}, \tag{2.7}$$

where $\partial \boldsymbol{v}/\partial t$ describes the time evolution of the flow velocity in a fixed reference frame [21].

The ions and electrons in a plasma can each be thought of as a separate macroscopic fluid consisting of identical particles. However, these ‘fluids’ are not collisionless, which gives rise to pressure gradients and shear stress. To account for these effects, an additional term $\boldsymbol{\nabla} \cdot \mathsf{P}$ is introduced. Assuming the ions are singly ionized, i.e. $n_\mathrm{e} = n_\mathrm{i}$, this gives the two-fluid force balance equations

$$n_\mathrm{i} m_\mathrm{i} \left(\frac{\partial \boldsymbol{v}_\mathrm{i}}{\partial t} + (\boldsymbol{v}_\mathrm{i} \cdot \boldsymbol{\nabla}) \, \boldsymbol{v}_\mathrm{i} \right) = -\boldsymbol{\nabla} \cdot \mathbf{P}_\mathrm{i} + n_\mathrm{i} e \left(\boldsymbol{E} + \boldsymbol{v}_\mathrm{i} \times \boldsymbol{B} \right) \tag{2.8}$$

$$n_\mathrm{e} m_\mathrm{e} \left(\frac{\partial \boldsymbol{v}_\mathrm{e}}{\partial t} + (\boldsymbol{v}_\mathrm{e} \cdot \boldsymbol{\nabla}) \, \boldsymbol{v}_\mathrm{e} \right) = -\boldsymbol{\nabla} \cdot \mathbf{P}_\mathrm{e} - n_\mathrm{e} e \left(\boldsymbol{E} + \boldsymbol{v}_\mathrm{e} \times \boldsymbol{B} \right), \tag{2.9}$$

where n represents number density, e is the magnitude of the charge on the electron, $\mathbf{P}$ is the stress tensor and the subscripts 'i' and 'e' denote 'ion' and 'electron' respectively [22]. Note that viscous and gravitational forces, and the transfer of momentum between ions and electrons, have been neglected.

If the distribution function is both isotropic and Maxwellian then

$$\boldsymbol{\nabla} \cdot \mathbf{P}_\mathrm{i} = \boldsymbol{\nabla} p_\mathrm{i} \tag{2.10}$$

$$\boldsymbol{\nabla} \cdot \mathbf{P}_\mathrm{e} = \boldsymbol{\nabla} p_\mathrm{e}, \tag{2.11}$$

where p represents pressure [21].

Therefore, combining (2.8) and (2.9) for an isotropic Maxwellian distribution function and assuming

$$n_\mathrm{i} = n_\mathrm{e} = n \tag{2.12}$$

and

$$\frac{m_\mathrm{i}}{m_\mathrm{i} + m_\mathrm{e}} \approx 1 \tag{2.13}$$

$$\frac{m_\mathrm{e}}{m_\mathrm{i} + m_\mathrm{e}} \approx 0 \tag{2.14}$$

produces the single-fluid force balance equation [22]

$$\rho \left(\frac{\partial \boldsymbol{v}}{\partial t} + (\boldsymbol{v} \cdot \boldsymbol{\nabla}) \, \boldsymbol{v} \right) = \boldsymbol{J} \times \boldsymbol{B} - \boldsymbol{\nabla} p, \tag{2.15}$$

where the mass density ρ, the single-fluid flow velocity $\boldsymbol{v}$, the current density $\boldsymbol{J}$ and the total pressure p are given by

$$\rho = n\left(m_{\mathrm{i}} + m_{\mathrm{e}}\right) \tag{2.16}$$

$$\boldsymbol{v} = \frac{m_{\mathrm{i}}\boldsymbol{v}_{\mathrm{i}} + m_{\mathrm{e}}\boldsymbol{v}_{\mathrm{e}}}{m_{\mathrm{i}} + m_{\mathrm{e}}} \tag{2.17}$$

$$\boldsymbol{J} = ne\left(\boldsymbol{v}_{\mathrm{i}} - \boldsymbol{v}_{\mathrm{e}}\right) \tag{2.18}$$

$$p = p_{\mathrm{i}} + p_{\mathrm{e}}. \tag{2.19}$$

If the plasma is in equilibrium then it can be assumed that $\boldsymbol{v}$ is constant and (2.15) becomes

$$\boldsymbol{J} \times \boldsymbol{B} = \boldsymbol{\nabla} p, \tag{2.20}$$

known as the equilibrium equation.

2.3.4 Equation of state

The ideal equation of state is

$$p = C\rho^{\gamma}, \tag{2.21}$$

where C is a constant and γ is the ratio of specific heat at constant pressure to specific heat at constant volume [21].

It follows that

$$\frac{d}{dt}\left(p\rho^{-\gamma}\right) = 0. \tag{2.22}$$

Since $p = p(x, y, z, t)$, $\rho = \rho(x, y, z, t)$ and γ is constant, the same procedure can be applied as in (2.7) to obtain

$$\left(\frac{\partial}{\partial t} + \boldsymbol{v} \cdot \boldsymbol{\nabla}\right)\left(p\rho^{-\gamma}\right) = 0. \tag{2.23}$$

This can be expanded to produce

$$\frac{\partial p}{\partial t} + (\boldsymbol{v} \cdot \boldsymbol{\nabla})\, p - \gamma \frac{p}{\rho} \left(\frac{\partial \rho}{\partial t} + (\boldsymbol{v} \cdot \boldsymbol{\nabla})\, \rho \right) = 0. \tag{2.24}$$

Combining this with the continuity equation (2.5) gives

$$\frac{\partial p}{\partial t} = -\,(\boldsymbol{v} \cdot \boldsymbol{\nabla})\, p - \gamma p \boldsymbol{\nabla} \cdot \boldsymbol{v}. \tag{2.25}$$

2.3.5 Maxwell's equations

Two of Maxwell's equations are used in MHD, namely Ampère's circuital law (generally neglecting the displacement current $\varepsilon_0 \partial \boldsymbol{E}/\partial t$)

$$\boldsymbol{\nabla} \times \boldsymbol{B} = \mu_0 \boldsymbol{J} \tag{2.26}$$

and Faraday's law of induction

$$\boldsymbol{\nabla} \times \boldsymbol{E} = -\frac{\partial \boldsymbol{B}}{\partial t}. \tag{2.27}$$

2.3.6 Ohm's law

Multiplying the two-fluid force balance equations (2.8) and (2.9) by m_{e} and m_{i} respectively and then subtracting one from the other produces

$$\frac{n m_{\mathrm{i}} m_{\mathrm{e}}}{e} \frac{d}{dt} \left(\frac{\boldsymbol{J}}{n} \right) = \rho e \boldsymbol{E} + ne \left(m_{\mathrm{e}} \boldsymbol{v}_{\mathrm{i}} + m_{\mathrm{i}} \boldsymbol{v}_{\mathrm{e}} \right) \times \boldsymbol{B} + m_{\mathrm{i}} \boldsymbol{\nabla} p_{\mathrm{e}} - m_{\mathrm{e}} \boldsymbol{\nabla} p_{\mathrm{i}}, \tag{2.28}$$

assuming $n_{\mathrm{i}} = n_{\mathrm{e}} = n$ and that the distribution function is isotropic and Maxwellian, and recalling (2.16) and (2.18).

However,

$$m_{\mathrm{e}} \boldsymbol{v}_{\mathrm{i}} + m_{\mathrm{i}} \boldsymbol{v}_{\mathrm{e}} = (m_{\mathrm{e}} - m_{\mathrm{i}}) (\boldsymbol{v}_{\mathrm{i}} - \boldsymbol{v}_{\mathrm{e}}) + m_{\mathrm{i}} \boldsymbol{v}_{\mathrm{i}} + m_{\mathrm{e}} \boldsymbol{v}_{\mathrm{e}}. \tag{2.29}$$

Substituting (2.29) into (2.28), recalling (2.17) and neglecting m_e gives

$$\boldsymbol{E} + \boldsymbol{v} \times \boldsymbol{B} = \frac{1}{ne} \left(\boldsymbol{J} \times \boldsymbol{B} - \boldsymbol{\nabla} p_\mathrm{e} \right). \tag{2.30}$$

A comparison of the magnitude of terms in (2.30) yields

$$\frac{|\boldsymbol{J} \times \boldsymbol{B}|}{|ne\boldsymbol{v} \times \boldsymbol{B}|} \sim \frac{|\boldsymbol{\nabla} p_\mathrm{e}|}{|ne\boldsymbol{v} \times \boldsymbol{B}|} \sim \frac{\rho_{\mathrm{L\,i}}}{a}, \tag{2.31}$$

where a is the length scale of interest [23]. Therefore, for length scales much greater than the ion Larmor radius (i.e. $a \gg \rho_{\mathrm{L\,i}}$), the $\boldsymbol{J} \times \boldsymbol{B}$ and $\boldsymbol{\nabla} p_\mathrm{e}$ terms can be neglected, leaving

$$\boldsymbol{E} + \boldsymbol{v} \times \boldsymbol{B} = 0. \tag{2.32}$$

Note that the transfer of momentum between ions and electrons was neglected in the two-fluid force balance equations (2.8) and (2.9). If this effect is included then (2.32) becomes

$$\boldsymbol{E} + \boldsymbol{v} \times \boldsymbol{B} = \eta \boldsymbol{J}, \tag{2.33}$$

where η is the specific resistivity of the plasma [24].

Equations (2.32) and (2.33) are the ideal and resistive forms of Ohm's law respectively. If (2.32) is used then the set of equations is known as ideal MHD; if (2.33) is used then it is called resistive MHD.

2.3.7 Linearized ideal MHD equations

A common method for solving MHD problems is to linearize the equations. This method is based on the assumption that each of the variables can be described as a small perturbation to some equilibrium value, e.g. $p = p_0 + p_1$ etc. where a subscript 0 denotes an equilibrium value and a subscript 1 denotes a small perturbation to this value. The equations are then expanded in terms of equilibrium and perturbed parts, and any terms containing the product of two perturbed quantities are assumed to be negligible [25]. Time derivatives of equilibrium quantities are also neglected and it is generally assumed that there is no equilibrium flow, i.e. $\boldsymbol{v}_0 = 0$.

The ideal MHD equations can be combined and linearized to give

$$\frac{\partial \rho_1}{\partial t} = -\rho_0 \boldsymbol{\nabla} \cdot \boldsymbol{v}_1 - (\boldsymbol{v}_1 \cdot \boldsymbol{\nabla})\, \rho_0 \tag{2.34}$$

$$\rho_0 \frac{\partial \boldsymbol{v}_1}{\partial t} = \boldsymbol{J}_0 \times \boldsymbol{B}_1 + \boldsymbol{J}_1 \times \boldsymbol{B}_0 - \boldsymbol{\nabla} p_1 \tag{2.35}$$

$$\frac{\partial p_1}{\partial t} = -\gamma p_0 \boldsymbol{\nabla} \cdot \boldsymbol{v}_1 - (\boldsymbol{v}_1 \cdot \boldsymbol{\nabla})\, p_0 \tag{2.36}$$

$$\frac{\partial \boldsymbol{B}_1}{\partial t} = \boldsymbol{\nabla} \times (\boldsymbol{v}_1 \times \boldsymbol{B}_0) \tag{2.37}$$

$$\mu_0 \boldsymbol{J}_1 = \boldsymbol{\nabla} \times \boldsymbol{B}_1. \tag{2.38}$$

This new set of equations can be simplified by introducing the plasma displacement $\boldsymbol{\xi}$ given by

$$\frac{\partial \boldsymbol{\xi}}{\partial t} = \boldsymbol{v}_1. \tag{2.39}$$

Under these assumptions, this is the same as

$$\frac{\partial \boldsymbol{\xi}}{\partial t} = \boldsymbol{v} \tag{2.40}$$

since it is assumed that $\boldsymbol{v}_0 = 0$.

Using the plasma displacement $\boldsymbol{\xi}$, equations (2.34), (2.35), (2.36), (2.37) and

(2.38) become

$$\rho_1 = -\rho_0 \boldsymbol{\nabla} \cdot \boldsymbol{\xi} - (\boldsymbol{\xi} \cdot \boldsymbol{\nabla})\, \rho_0 \tag{2.41}$$

$$\rho_0 \frac{\partial^2 \boldsymbol{\xi}}{\partial t^2} = \boldsymbol{J}_0 \times \boldsymbol{B}_1 + \boldsymbol{J}_1 \times \boldsymbol{B}_0 - \boldsymbol{\nabla} p_1 \tag{2.42}$$

$$p_1 = -\gamma p_0 \boldsymbol{\nabla} \cdot \boldsymbol{\xi} - (\boldsymbol{\xi} \cdot \boldsymbol{\nabla})\, p_0 \tag{2.43}$$

$$\boldsymbol{B}_1 = \boldsymbol{\nabla} \times (\boldsymbol{\xi} \times \boldsymbol{B}_0) \tag{2.44}$$

$$\mu_0 \boldsymbol{J}_1 = \boldsymbol{\nabla} \times \boldsymbol{\nabla} \times (\boldsymbol{\xi} \times \boldsymbol{B}_0)\,. \tag{2.45}$$

The time derivatives have been removed from (2.41), (2.43), (2.44) and (2.45), and each of the perturbed quantities ρ_1, p_1, $\boldsymbol{B}_1$ and $\boldsymbol{J}_1$ is a function of only $\boldsymbol{\xi}$ and an equilibrium quantity. Equation (2.42) represents force per unit volume.

2.4 Peeling–ballooning instabilities

With the ideal MHD equations linearized about an equilibrium state and the perturbed quantities expressed as functions of the displacement $\boldsymbol{\xi}$ with respect to that equilibrium state, the change in potential energy δW caused by a perturbation to the equilibrium can also be expressed as a function of $\boldsymbol{\xi}$ [11].

If a small perturbation to an equilibrium state causes an increase in potential energy then the system will tend to move back to its previous lower-energy state; the system is said to be in a stable equilibrium. This is analagous to a marble at the bottom of a bowl – if moved a short distance, the marble will roll back down again to where it was before. On the other hand, if a small perturbation causes a decrease in potential energy then the system will tend to continue to move away from its previous equilibrium state; the system is said to be in an unstable equilibrium. This is analagous to a ball at the top of a hill – if left undisturbed, the ball will stay where it is, but if moved a short distance, it will keep rolling down the hill.

A third possibility is that a small perturbation causes no change in potential energy, in which case the system is said to be in a marginally stable equilibrium. This is analagous to a ball on level ground. Finally, it may be that a small perturbation in one direction causes an increase in potential energy while a small perturbation in another direction causes a decrease. This is analagous to a ball on a saddle – if moved to a higher part of the saddle, the ball may roll back down again to where it was before but is likely to fall off sooner or later. Such a system is also in an unstable equilibrium.

Therefore, in order for a plasma to be in a stable equilibrium, all possible small perturbations must cause an increase in potential energy, i.e. δW must be positive for all small values of $\boldsymbol{\xi}$. The value of δW can be calculated using the volume integral

$$\delta W = -\frac{1}{2}\int_V \boldsymbol{\xi} \cdot \boldsymbol{F} dV, \tag{2.46}$$

where the force per unit volume $\boldsymbol{F}$ is given by

$$\boldsymbol{F}\left(\boldsymbol{\xi}\right) = \rho_0 \frac{\partial^2 \boldsymbol{\xi}}{\partial t^2} = \boldsymbol{J}_0 \times \boldsymbol{B}_1 + \boldsymbol{J}_1 \times \boldsymbol{B}_0 - \boldsymbol{\nabla} p_1 \tag{2.47}$$

as in (2.42) [26].

It follows that δW is explicitly given by

$$\begin{aligned}\delta W = \frac{1}{2}\int_V \Bigg(& \left|\boldsymbol{B}_{1\perp}\right|^2 + B_0^2 \left|\boldsymbol{\nabla} \cdot \boldsymbol{\xi}_\perp + 2\boldsymbol{\xi}_\perp \cdot \boldsymbol{\kappa}\right|^2 + \gamma p_0 \left|\boldsymbol{\nabla} \cdot \boldsymbol{\xi}\right|^2 \\ & - 2\left(\boldsymbol{\xi}_\perp \cdot \boldsymbol{\nabla} p_0\right)\left(\boldsymbol{\kappa} \cdot \boldsymbol{\xi}_\perp^*\right) - \frac{J_{0\parallel}}{B_0}\left(\boldsymbol{\xi}_\perp^* \times \boldsymbol{B}_0\right) \cdot \boldsymbol{B}_{1\perp}\Bigg) dV, \end{aligned} \tag{2.48}$$

where asterisks denote complex conjugates, $\parallel$ and $\perp$ denote components in the direction parallel and perpendicular to the equilibrium magnetic field $\boldsymbol{B}_0$ respectively, and $\boldsymbol{\kappa}$ is the curvature of the equilibrium magnetic field $\boldsymbol{B}_0$

given by

$$\boldsymbol{\kappa} = \left(\hat{\boldsymbol{b}} \cdot \boldsymbol{\nabla}\right) \hat{\boldsymbol{b}}, \tag{2.49}$$

where $\hat{\boldsymbol{b}}$ is the unit vector in the direction of the equilibrium magnetic field $\boldsymbol{B}_0$ [11].

Solutions to (2.48) where δW is negative correspond to instabilities [26]. The first three terms are always positive and therefore always stabilizing. The fourth term can be negative and therefore destabilizing, depending on the relative direction of $\boldsymbol{\nabla} p$ and $\boldsymbol{\kappa}$, which varies throughout the plasma. The region where this term is negative is said to have 'bad curvature' and is found on the outboard side of tokamaks, whereas the region where it is positive is said to have 'good curvature' and is found on the inboard side. This fourth term is large when the pressure gradient is large, and the instability that results from this large pressure gradient is called a 'ballooning mode'. The fifth term can also be negative and therefore destabilizing. This fifth term is large when the current density is large, and the instability that results from this large current density is called a 'peeling mode'. These modes may occur together and are collectively known as 'peeling–ballooning modes'.

Large pressure gradients and current densities are found in the edge of H-mode plasmas – precisely where ELMs occur. Furthermore, ELMs have been observed to occur when modelling calculates the plasma to be near the stability limit for peeling–ballooning modes [27, 28], suggesting that ELMs are triggered by peeling–ballooning modes.

This analysis of peeling–ballooning modes is based on linearized MHD equations, i.e. perturbed quantities are assumed to be small in comparison to equilibrium quantities, and any terms containing the product of two perturbed quantities are assumed to be negligible. However, as the peeling–ballooning mode grows, this assumption is no longer valid and the mode evolution enters a non-linear phase in which particles and heat are explosively ejected from the plasma towards the divertor. Since charged particles are constrained to gyrate about magnetic field lines but are free to move along them, transport parallel to the magnetic field is much faster than perpendicular transport.

Therefore, these ejected particles spread out very rapidly along field lines, forming characteristic filamentary structures as can be seen in figure 2.3. The number of filaments corresponds with the mode number of the underlying unstable peeling–ballooning mode.

2.5 ELM structure

2.5.1 D_α emission

The divertor region of a tokamak is cooler than the plasma, and is cool enough for many of the ions and electrons to recombine, forming neutral atoms. In some of these neutral atoms, the electron will initially occupy a higher energy level and later decay to a lower level, emitting a photon, the frequency ν of which depends on the difference in energy levels ΔE according to the Planck equation

$$\Delta E = h\nu, \tag{2.50}$$

where h is Planck's constant.

The series of spectral lines produced by electrons decaying to the $n = 1$ level in hydrogen is not in the visible region of the electromagnetic spectrum. The series produced by electrons decaying to the $n = 2$ level is in the visible region and is called the Balmer series. The lowest-frequency line in the Balmer series, which is produced by decay from the $n = 3$ level, is called the H_α line for protonic hydrogen and the D_α line for deuterium. D_α emission has a wavelength of 656 nm [29]. Since this is in the visible region of the electromagnetic spectrum, it can be easily recorded using a visible light camera. ELMs can be observed as sharp peaks in line-integrated D_α signals such as in the bottom pane of figure 2.2 (a), and the size of an ELM is correlated with the height of its D_α peak.

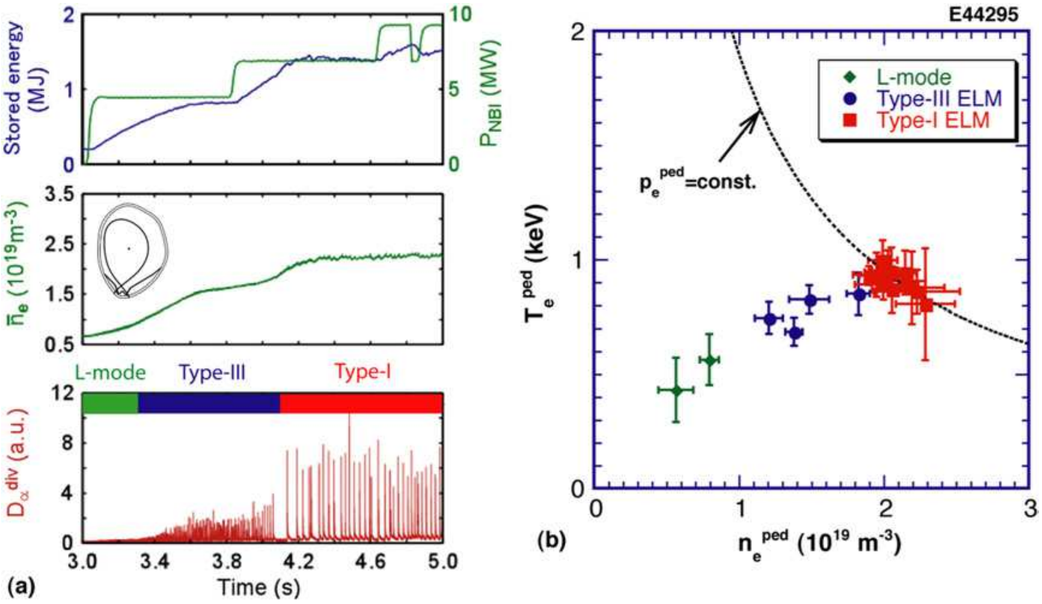

Figure 2.2 (*a*) As P_{in} is increased in the JT-60U tokamak (top), first type-III ELMs and then type-I ELMs are observed (bottom). (*b*) Type-I ELMs correspond to the highest pedestal temperature and density. From [30].

2.5.2 Fast camera images

MAST has an open divertor and no cryo-pumps, which means that neutral atoms formed at the divertor tend to spread out and fill the whole vessel outside of the plasma. Therefore, MAST has a high level of D_α emission compared to tokamaks with closed, pumped divertors. In addition, its geometry allows a camera to be placed such that the whole plasma is in its field of view. This puts MAST foremost among tokamaks in terms of how well the plasma can be viewed. MAST is equipped with a fast camera that records images of the plasma using D_α light. It has a frame rate of up to 100 kHz, which is fast enough to observe ELM dynamics. However, high frame rates come at the expense of spatial resolution.

The good view of the plasma in MAST enables ELM filaments to be clearly seen using the camera, and their location, width and intensity can be measured using the images taken by the camera, such as figure 2.3. The fast camera allows ELM filaments to be tracked from one frame to the next, which enables their velocity to be measured as well.

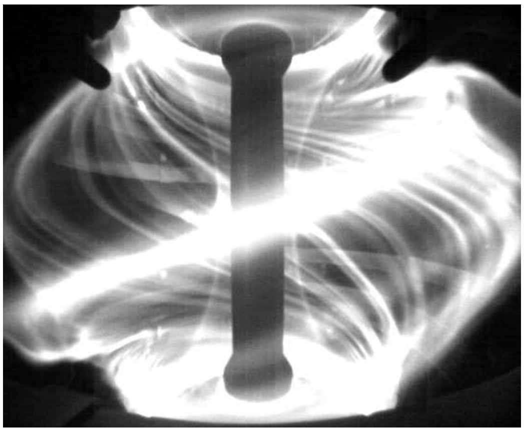

Figure 2.3 Image taken in D_α light with the fast camera, displaying ELMs, which appear as bright filaments.

2.6 ELM types

ELMs are classified from an empirical and phenomenological perspective [31]. The numbering convention was introduced by E J Doyle *et al.* for the Doublet III-D (DIII-D) tokamak [32].

As the heating power P_{in} in a tokamak with an L-mode plasma is increased, it reaches the L–H transition threshold power $P_{\mathrm{L-H}}$ and the plasma enters H-mode. For values of P_{in} only slightly greater than $P_{\mathrm{L-H}}$, low-amplitude 'dithering' ELMs are sometimes observed, which are thought to be brief transitions from H-mode to L-mode and back again [17].

As P_{in} is increased further, type-III or 'small' ELMs are observed (figure 2.2). The frequency f_{ELM} at which they occur is quite high, usually a few hundred hertz [30], but this frequency decreases with increasing P_{in} (figure 2.4) until the ELMs disappear completely and the plasma goes into ELM-free H-mode [17]. In some ELM-free plasmas, impurities are very well confined and accumulate, which can cause the plasma to terminate in a disruption [18].

However, some ELM-free plasmas contain other edge modes that enhance transport sufficiently to prevent an accumulation of impurities.

At greater values of P_{in}, type-I or 'giant' ELMs are observed (figure 2.2). f_{ELM} for type-I ELMs is at least an order of magnitude lower than for type-III ELMs [30], and unlike with type-III ELMs, f_{ELM} increases with increasing P_{in} (figure 2.4).

It is necessary to define some new quantities here. Firstly, plasma β is defined as the ratio of plasma pressure p to magnetic pressure $B^2/(2\mu_0)$. It can be thought of as a measure of how efficiently the plasma is confined by the magnetic field. Spherical tokamaks tend to have higher values of β than conventional tokamaks. Secondly, the safety factor q is defined as the number of times that a magnetic field line travels around the tokamak in the toroidal direction for each time that it travels around in the poloidal direction. It is called the safety factor because certain instabilities tend to occur for $q < 1$. Finally, triangularity is a measure of how triangular the shape of the poloidal cross-section of the plasma is.

Low-amplitude type-II and 'grassy' ELMs are irregular with high f_{ELM} [32]. Type-II ELMs usually only occur in highly collisional plasmas that are close to connected double-null (CDN) configuration and below a certain critical value of plasma β. Grassy ELMs usually only occur in high-triangularity plasmas that have high β and a particular value of the safety factor q. The required values differ between tokamaks. For example, on the JT-60U tokamak in Japan, grassy ELMs only occur for triangularity $\kappa > 0.34$ and poloidal $\beta \gtrsim 1.5$ [18].

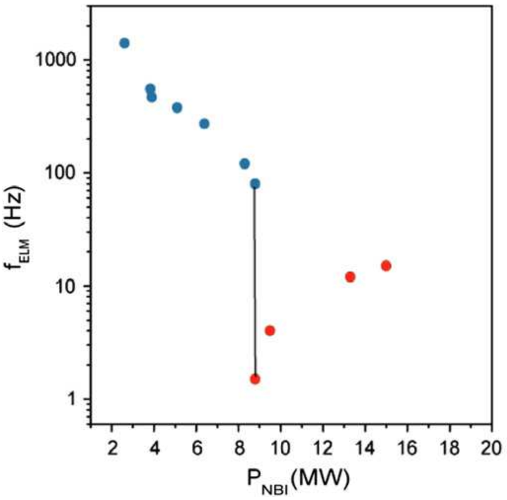

Figure 2.4 As P_{in} is increased in the JET tokamak, f_{ELM} decreases for type-III ELMs but increases for type-I ELMs. From [30].

2.7 ELM mitigation

Type-I ELMs are found in the plasmas with the best confinement and performance [16], so type-I ELMy H-mode is planned to be the reference inductive operational scenario for ITER [30]. However, a single type-I ELM can eject up to 20 % of the energy stored in the pedestal region [30] in around 250 µs [33]. This would lead to unacceptably large heat loads on ITER's divertor [16]. Therefore, there are two options: either develop an alternative ITER-relevant regime with comparable performance to type-I ELMy H-mode (passive control) or find a way to mitigate the effects of type-I ELMs (active control) [11].

Active ELM control involves either eliminating ELMs completely (ELM suppression) or making them more frequent and smaller, and therefore more manageable (ELM mitigation). ELM control methods include ELM pacemaking through pellet injection [34], magnetic triggering based on giving the plasma vertical 'kicks' [35], modification of the density profile through lithium wall coatings [36], and ergodization of the plasma edge through resonant magnetic perturbations (RMPs) produced by external coils. This thesis concerns the latter.

2.8 Resonant magnetic perturbations

If a plasma is toroidally symmetric (axisymmetric) then magnetic field lines will lie on nested toroidal magnetic surfaces. The magnetic flux Ψ within each of these surfaces must be constant on that surface. Therefore, the magnetic flux Ψ can be used to label these surfaces, which are known as flux surfaces.

It can be seen from the equilibrium equation (2.20) that

$$\boldsymbol{B} \cdot \boldsymbol{\nabla} p = 0 \tag{2.51}$$

if the plasma is in equilibrium, i.e. pressure is also constant on a flux surface [37].

A quantity that is constant on a flux surface is known as a flux function. Many other quantities are also at least approximately flux functions, so it is often convenient to plot quantities against Ψ and to use Ψ as the minor radial co-ordinate. When this is done, Ψ is typically normalized such that the normalized flux $\Psi_{\mathrm{N}} = 0$ on the magnetic axis (in the middle of the plasma) and $\Psi_{\mathrm{N}} = 1$ on the last closed flux surface (LCFS). Unless otherwise stated, this generally refers to poloidal flux. Often, $\Psi_{\mathrm{N}}^{1/2}$ is used instead, since in a cylindrical plasma with circular poloidal cross-section and uniform toroidal current density (or for toroidal flux, uniform toroidal field), this corresponds exactly to the normalized geometrical minor radius.

A rational or resonant surface is a flux surface on which the value of the safety factor q is a rational number. On such surfaces, magnetic field lines join up with themselves after m toroidal turns and n poloidal turns, where $q = m/n$. If there is a perturbation to the magnetic field with toroidal mode number n and poloidal mode number m then a field line on the $q = m/n$ surface will always see the same phase of this perturbation. In contrast, a field line on a non-rational surface will sample all phases of the perturbation equally, so the integral of the perturbation along a field line on a non-rational surface will be zero.

Magnetic perturbations perpendicular to flux surfaces can cause magnetic islands to form on resonant surfaces [38]. Such perturbations are called resonant magnetic perturbations (RMPs). Magnetic islands on adjacent resonant surfaces can overlap, causing the field lines to trace out chaotic paths and destroying all the closed flux surfaces between the two resonant surfaces [11]. The resulting magnetic field is said to be stochastic or ergodic. Figure 2.5 shows Poincaré plots (see section 3.2) for a MAST plasma with and without the application of RMPs. Without RMPs, the magnetic field consists entirely of unperturbed, unbroken flux surfaces. With RMPs, the bulk of the plasma ($\Psi_{\mathrm{N}}^{1/2} \lesssim 0.7$) also consists entirely of unbroken, although slightly perturbed, flux surfaces. However, nearer the edge ($0.7 \lesssim \Psi_{\mathrm{N}}^{1/2} \lesssim 0.9$), these closed flux surfaces gradually give way to chains of magnetic islands. The magnetic shear (the normalized gradient of the safety factor q) increases towards the plasma edge, which means that low-order rational surfaces become more closely spaced. Therefore, in the plasma edge ($\Psi_{\mathrm{N}}^{1/2} \gtrsim 0.9$), the magnetic islands overlap, destroying the closed flux surfaces and forming a stochastic field.

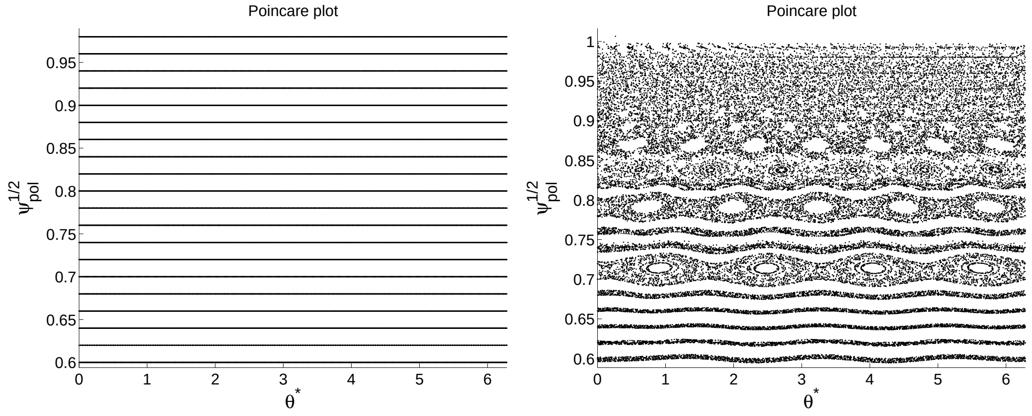

(a) (b)

Figure 2.5 Poincaré plots (a) without and (b) with the application of RMPs, showing closed flux surfaces, magnetic islands and stochastic regions.

The destruction of flux surfaces in the plasma edge causes parallel transport to have a radial component and therefore significantly enhances radial transport in the edge. This could reduce the pedestal pressure gradient below the peeling–ballooning threshold gradient and thus eliminate ELMs. Therefore, RMPs could be used as a form of ELM suppression. On the other hand, RMPs could trigger instabilities in the plasma edge and cause ELMs to occur at lower pressure gradients earlier in the ELM cycle than they would naturally. These triggered ELMs would be smaller and more frequent than natural ELMs, so RMPs could also be used as a form of ELM mitigation.

2.9 Effect of RMPs in MAST experiments

The application of RMPs has been successfully implemented to achieve complete suppression of type-I ELMs on DIII-D [39, 40] and mitigation of type-I ELMs on JET [41, 42] and ASDEX Upgrade [43]. MAST is equipped with two off-midplane rows of ELM coils [44] similar to those used on DIII-D. The ELM coils on MAST originally consisted of six upper and six lower coils. Later, six additional lower coils were installed in time for campaign M8, which began in 2011. These additional coils have made a wider range of coil configurations possible. The ELM coils can be seen in figure 2.6.

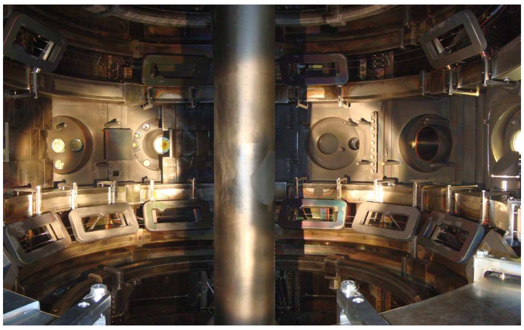

Figure 2.6 View inside the MAST vessel, showing the ELM coils, which are rectangular in shape. Four of the six upper coils and six of the twelve lower coils are fully visible. A seventh lower coil is obscured from view behind the centre column, while the remaining coils are located on the near side of the vessel.

The application of RMPs produced by these ELM coils causes a clear decrease in line-averaged electron density n_e (density pump-out) of up to 35 % in a wide range of L-mode plasmas, but only when there is an alignment between the perturbation and the equilibrium magnetic field [44, 45] that maximizes the size of the resonant components of the applied magnetic field. This density pump-out is the result of increased particle transport, which is thought to be caused by the formation of a stochastic magnetic field in the plasma edge. In addition, the application of RMPs in L-mode discharges can cause the rotation profile to change and the radial electric field E_r to become less negative [46].

In H-mode, the occurrence of density pump-out is limited to a much narrower range of q_{95} (the value of the safety factor q at $\Psi_\mathrm{N} = 0.95$) and appears to be much more sensitive to the pitch of the equilibrium magnetic field lines than in L-mode [45]. When density pump-out does occur, it is typically accompanied by an increase in ELM frequency and a corresponding decrease in ELM energy loss, or by a back-transition to L-mode [45].

In CDN H-mode discharges on MAST, a brief initial drop in line-averaged density coincides with a short burst of very rapid ELMs. This is followed by a more gradual decrease in density consistent with what would be expected due to the increase in ELM frequency above that of unmitigated ELMs. However, it is difficult to ascertain whether or not the brief initial drop in density is consistent what would be expected due to the very rapid ELMs. In lower single-null (LSN) H-mode discharges on MAST, the brief initial drop in density and the short burst of very rapid ELMs are not observed. The gradual decrease in density appears to be consistent with what would be expected due to the increase in ELM frequency.

When density pump-out occurs, there is no significant corresponding change in temperature. Figure 2.7 shows typical examples of density pump-out occurring in L- and H-mode plasmas, while figures 2.8 and 2.9 show the corresponding density and temperature profiles during the pump-out phase. It can be seen that the density pump-out is not accompanied by a significant change in temperature in either L- or H-mode.

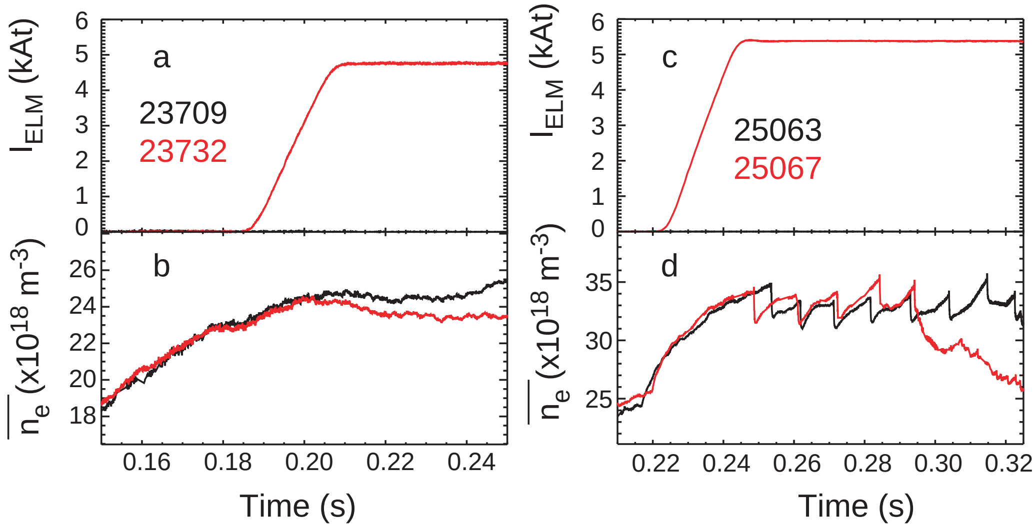

Figure 2.7 Comparison of line-averaged electron density n_e for discharges with and without applied RMPs, showing density pump-out (*b* and *d*) shortly after current is ramped in the ELM coils (*a* and *c*) for typical L- (*a* and *b*) and H-mode (*c* and *d*) discharges. The time delay in H-mode suggests a longer penetration time for the RMPs, which may be due to differences in screening between L- and H-mode.

The effect of RMPs in MAST experiments and related analyses of stochastic magnetic field structure in MAST plasmas form the subject of this thesis. In chapter 3, the effect that stochastic fields in L-mode plasmas have on temperature profiles is calculated. In chapter 4, various metrics characterizing the degree of stochasticity in both L- and H-mode plasmas are calculated and compared with the amount of density pump-out observed experimentally in those plasmas during the application of RMPs. In chapter 5, the results of lower single-null H-mode ELM mitigation experiments using $n = 4$ and $n = 6$ RMPs are presented. Finally, an analysis of a stochastic magnetic field formed by a current sheet on a rational surface in a MAST plasma is presented in chapter 6, and a summary of the thesis is given in chapter 7.

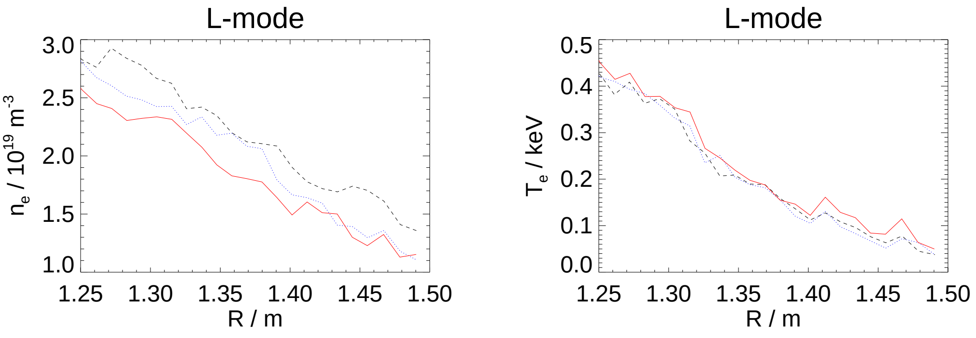

(a) *(b)*

Figure 2.8 (*a*) Density and (*b*) temperature profiles taken at 208 ms (dashed line), 212 ms (dotted line) and 216 ms (solid line) for the L-mode discharge in figure 2.7. The reduction in density is not accompanied by a significant change in temperature.

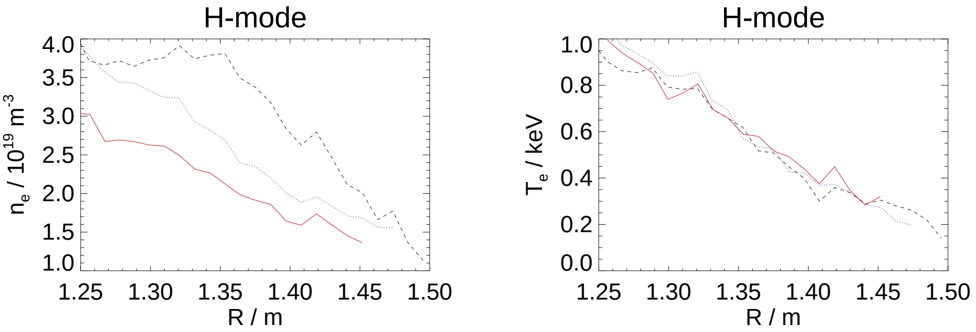

(a) *(b)*

Figure 2.9 (*a*) Density and (*b*) temperature profiles taken at 295 ms (dashed line), 308 ms (dotted line) and 320 ms (solid line) for the H-mode discharge in figure 2.7. The reduction in density is not accompanied by a significant change in temperature.

Chapter 3

Radial thermal diffusivity in a stochastic magnetic field

3.1 Background

As discussed in section 1.1, very high temperatures are required for nuclear fusion to occur. The temperature reached in a tokamak or other fusion device depends on the amount of heating power injected into the plasma and produced by fusion reactions, and on the flux of heat leaving the plasma. This outward or (minor) radial heat flux is directly proportional to the plasma's volumetric heat capacity (i.e. the product of its specific heat capacity and its density), the magnitude of the radial temperature gradient and a quantity known as the radial thermal diffusivity. This is described in more detail in section 3.3.

Therefore, the radial thermal diffusivity plays a role in determining the temperature that can be obtained in the plasma. The magnetic field structure in a tokamak can have an effect on the value of the radial thermal diffusivity, and in this chapter, the effect of a stochastic magnetic field on the radial thermal diffusivity is explored.

3.2 The ERGOS code

ERGOS is a code for modelling ergodic vacuum magnetic fields [47]. It can be used to compute many properties of these ergodic fields, several of which are calculated using field line tracing with a Runge–Kutta algorithm. This method has been employed extensively to obtain many of the results presented in this thesis, including calculations of the radial thermal diffusivity.

The field lines are all started in one poloidal cross-section, i.e. at one toroidal angle. They are then followed either for a given number of turns or until they reach a given field line length. Every time that each field line completes a toroidal turn, its radial and poloidal locations are recorded and can be used to calculate various properties of the magnetic field structure. These radial and poloidal locations can also be plotted to make what is known as a Poincaré plot (figure 3.1), which provides an intuitive way of visualizing magnetic field structure and the effect of RMPs, and also of understanding the nature of field line tracing.

ERGOS can perform this field line tracing either in cylindrical polar co-ordinates (R, ϕ, Z) or in field-aligned co-ordinates (s, ϕ, θ^*), where $s = \Psi_{\mathrm{N}}^{1/2}$, ϕ is the toroidal angle and θ^* is the field-aligned poloidal angle, i.e. it is defined such that field lines are straight lines in (ϕ, θ^*).

The Runge–Kutta algorithm is computationally more efficient when a larger toroidal step size is used. However, using too large a step size can introduce significant numerical error to the calculations. In order to determine the maximum step size that does not introduce significant numerical error, the algorithm was carried out without RMPs, i.e. using only the axisymmetric equilibrium, with different toroidal step sizes. If field lines were found to deviate noticeably from the flux surface on which they were started then this deviation was assumed to be due to numerical error and the toroidal step size was deemed to be too large.

When field-aligned co-ordinates were used, as few as 400 toroidal discretization points were found to be sufficient, corresponding to a toroidal step size

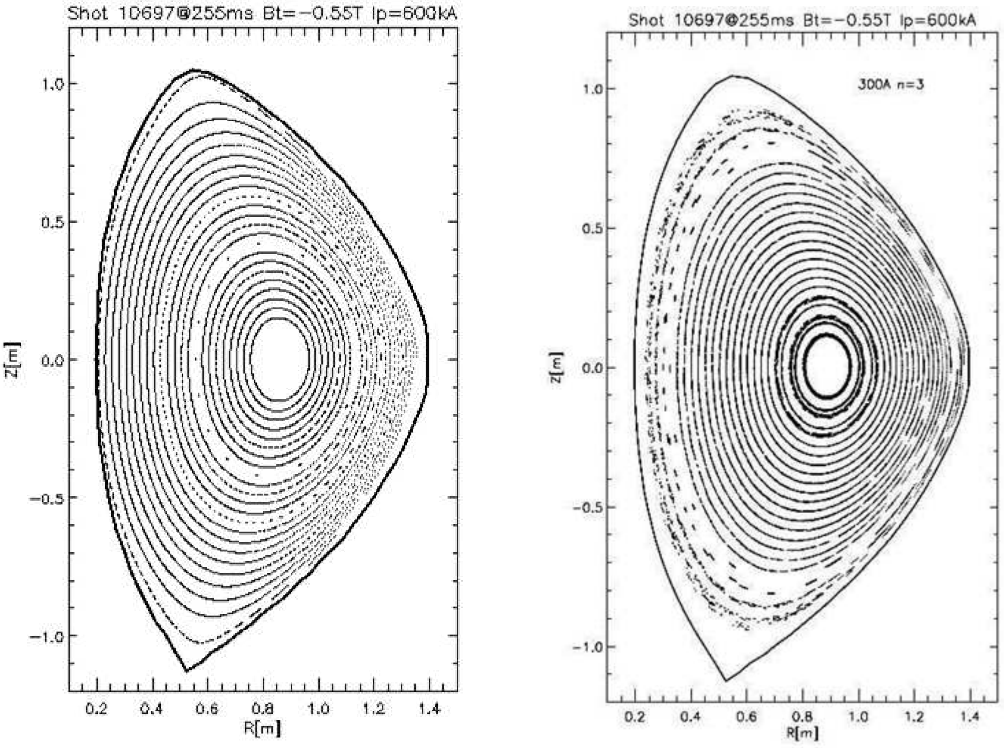

(a) *(b)*

Figure 3.1 Poincaré plots of the magnetic field in a MAST plasma (*a*) without and (*b*) with the application of RMPs. Without RMPs, the magnetic field consists purely of closed magnetic flux surfaces; with RMPs, magnetic island chains and stochastic regions appear in the edge of the plasma.

of 0.9°. However, in ERGOS, the field-aligned poloidal angle θ^* is undefined outside the LCFS, meaning that field-aligned co-ordinates can only be used for field line tracing when the field lines are confined to the plasma for the entire distance over which they are followed. When cylindrical polar co-ordinates were used, up to 1000 toroidal discretization points were found to be necessary, corresponding to a toroidal step size of 0.36°. However, cylindrical polar co-ordinates are defined both inside and outside the LCFS, so they can be used for field line tracing outside the LCFS.

EFIT is a code designed to reconstruct axisymmetric plasma equilibria consisting of the plasma shape, plasma parameter profiles and the magnetic field structure. These reconstructed equilibria are consistent with MHD equilibrium constraints from external experimental measurements [48]. EFIT equilibria are required for ERGOS calculations. For the ERGOS calculations presented in this thesis, standard scheduler EFIT was used with a grid resolution of 65×65 points.

3.3 Thermal conduction

Fourier's law of thermal conduction states that heat flux density $\boldsymbol{q}$ is proportional to the negative temperature gradient $-\boldsymbol{\nabla} T$:

$$\boldsymbol{q} = -\kappa \boldsymbol{\nabla} T, \tag{3.1}$$

where κ is the thermal conductivity of the medium through which the heat is flowing, which is proportional to the medium's density ρ and specific heat capacity c:

$$\kappa = \rho c \chi, \tag{3.2}$$

where χ is the thermal diffusivity of the medium.

The heat continuity equation can be derived in an analagous manner to the mass continuity equation in section 2.3 with mass density ρ replaced by heat density $\rho c T$ and mass flux density $\rho \boldsymbol{v}$ replaced by heat flux density $\boldsymbol{q}$:

$$\rho c \frac{\partial T}{\partial t} = -\boldsymbol{\nabla} \cdot \boldsymbol{q}, \tag{3.3}$$

assuming ρ and c are constant.

Substituting (3.1) and (3.2) into (3.3) produces the heat equation

$$\frac{\partial T}{\partial t} = \boldsymbol{\nabla} \cdot \left(\chi \boldsymbol{\nabla} T \right). \tag{3.4}$$

This shows that the rate of change of temperature is proportional to the thermal diffusivity χ and depends on the temperature profile.

3.4 Field line tracing

3.4.1 Kolmogorov length

In a stochastic magnetic field, two initially close field lines will diverge from each other as they travel around the tokamak. The distance d between them increases exponentially, and the rate of this exponential increase is quantified by the Kolmogorov length L_K:

$$d \propto \exp\left(\frac{L_\parallel}{L_\mathrm{K}}\right), \tag{3.5}$$

where $L_\parallel$ is the length over which the field lines are followed [49].

3.4.2 Field line dispersion

In a stochastic magnetic field, the radial excursion of field lines follows a random walk process. The root mean square radial excursion of field lines is proportional to the square root of their length $L_\parallel$, meaning that the radial excursion Δr is given by

$$\left\langle (\Delta r)^2 \right\rangle = 2 D_\mathrm{FL} L_\parallel, \tag{3.6}$$

where the constant of proportionality D_FL is the field line diffusion coefficient. However, as seen in figure 3.2, in fields that are not fully ergodic, i.e. that contain some remnant magnetic islands and closed flux surfaces as is the case for this vacuum modelling, the radial excursion of field lines does not follow a truly random walk process and the linear relationship between $\langle (\Delta r)^2 \rangle$ and $L_\parallel$ only applies up to a certain number of toroidal turns (in this case ~ 25), after which $\langle (\Delta r)^2 \rangle$ increases more slowly. Since no truly random walk process occurs, this process should more properly be referred to as 'field line dispersion' rather than 'field line diffusion'.

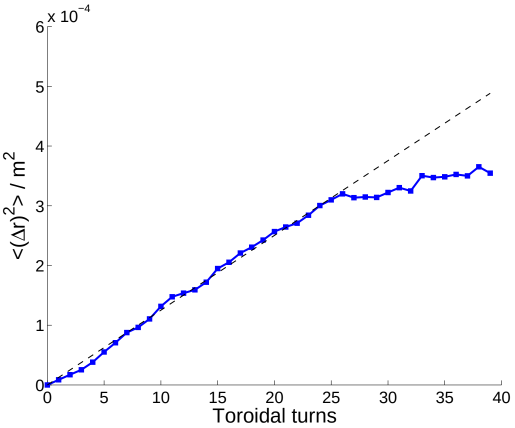

Figure 3.2 Variation of $\langle(\Delta r)^2\rangle$, for field lines traced from the same equilibrium flux surface, with the number of toroidal turns over which they are traced.

3.5 Rechester–Rosenbluth theory

The Rechester–Rosenbluth theory predicts a value for the radial thermal diffusivity χ_r in a stochastic magnetic field based on the motion of electrons along diverging field lines [50]. The motion of ions is less important because they are a factor of $(m_\mathrm{i}/m_\mathrm{e})^{1/2}$ less mobile. The equation used to calculate χ_r depends on whether the plasma is in a collisional or collisionless regime, which is characterized by the electron mean free path λ_e and the Kolmogorov length L_K.

If $\lambda_\mathrm{e} \gg L_\mathrm{K}$ then electrons travelling along initially close field lines will follow these field lines for a distance of many Kolmogorov lengths before undergoing a collision (collisionless regime). During this time, the trajectories of these electrons will have diverged from each other significantly. In this case, the radial thermal diffusivity χ_r is given by

$$\chi_r = D_\mathrm{FL} v_\mathrm{th\,e}, \tag{3.7}$$

where $v_\mathrm{th\,e}$ is the magnitude of the thermal velocity of the electrons [50].

On the other hand, if $\lambda_\mathrm{e} \ll L_\mathrm{K}$ then electrons travelling along initially close field lines will undergo a collision before travelling a single Kolmogorov length (collisional regime). Consequently, the trajectories of these electrons will not have diverged significantly from each other. In this case, χ_r is given by

$$\chi_r = D_{\mathrm{FL}} v_{\mathrm{th\,e}} \frac{\lambda_{\mathrm{e}}}{L_{\mathrm{c}}}, \tag{3.8}$$

where L_{c} is the parallel thermal correlation length [50].

In the absence of stochasticity (i.e. the field consists of nested flux surfaces), diffusion of both particles and heat is found experimentally to exceed the levels predicted by neo-classical transport theory [51]. This is thought to be due to turbulence and is known as anomalous transport. The Rechester–Rosenbluth theory predicts that in a stochastic field, the value of the radial thermal diffusivity χ_r should be greater than that predicted by neo-classical theory. However, this does not necessarily imply that the value of χ_r should be greater than experimentally observed anomalous values.

If the value of χ_r predicted by the Rechester–Rosenbluth theory for a stochastic field were to be greater than the anomalous value observed experimentally in the absence of stochasticity then the formation of a stochastic field would be expected to increase the radial thermal diffusivity and therefore lead to a reduction in temperature. On the other hand, if the value predicted by the Rechester–Rosenbluth theory were to be less than this anomalous value then the formation of a stochastic field would not be expected to have an effect on the temperature profile.

As mentioned in section 2.9, the application of RMPs does not lead to a reduction in temperature on MAST, despite having other effects on the plasma. The value of the radial thermal diffusivity χ_r predicted by the Rechester–Rosebluth theory was calculated for MAST to see whether it would be greater than the anomalous value observed experimentally in the absence of stochasticity and consequently whether a reduction in temperature would be expected.

3.6 Vacuum modelling using ERGOS

3.6.1 Kolmogorov length

A radial profile for the Kolmogorov length L_{K} in the edge of a MAST L-mode plasma with applied RMPs from 1.4 kA of current in the ELM coils was obtained by starting 100 field lines on each of five equilibrium flux surfaces and following these field lines for 40 toroidal turns. The distance d between pairs of field lines as measured in flux space, i.e. $d = (s^2 + \theta^{*2})^{1/2}$, was calculated and a figure for L_{K} was found by averaging over these pairs:

$$\frac{1}{L_{\mathrm{K}}} = \frac{1}{\langle L_{\parallel} \rangle} \left\langle \ln\left(\frac{d}{d_0}\right)\right\rangle , \tag{3.9}$$

where d_0 is the initial distance between the two field lines in a pair. Since $0 \leq \theta^* \leq 2\pi$ and within the plasma $0 \leq s \leq 1$, for the Kolmogorov length calculations, θ^* was normalized such that $0 \leq \theta^* \leq 1$ in order to prevent poloidal divergence of field lines dominating over radial divergence. To convert the distance d to a distance in real space, it could be mapped to radial distance at the midplane, for example. However, in this case, the ratio d/d_0 is the value that is used, and this mapping would not alter the value of this ratio.

Since the field lines do not need to be followed for many turns, all of them remain within the LCFS, enabling the field line tracing for the field line dispersion coefficient to be performed in the more numerically efficient field-aligned co-ordinates with just 400 toroidal discretization points. Provided sufficient toroidal discretization points are used, whether the calculation is performed in cylindrical polar co-ordinates or field-aligned co-ordinates has no effect on the results.

A radial profile for the electron mean free path λ_{e} in the plasma edge was obtained from temperature and density profiles measured using Thomson scattering. This was compared to the radial profile for the Kolmogorov length and it was found that $\lambda_{\mathrm{e}} \ll L_{\mathrm{K}}$ (figure 3.3), meaning that the edge of this

MAST L-mode plasma is in the collisional regime.

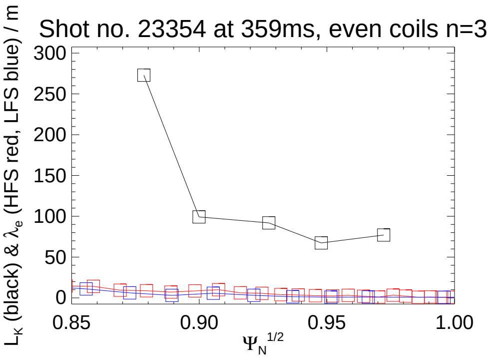

Figure 3.3 Comparison of L_K and λ_e.

3.6.2 Field line dispersion

A corresponding radial profile for the field line dispersion coefficient D_FL was calculated using a similar method. Once again, 100 field lines were started on each of the same five equilibrium flux surfaces and were followed for 40 toroidal turns, but rather than the distance between pairs of field lines, the radial excursion Δr of each field line was calculated instead, and a figure for D_FL was found by averaging over all 100 field lines started on each equilibrium flux surface:

$$D_\mathrm{FL} = \frac{\left\langle (\Delta r)^2 \right\rangle}{2 \left\langle L_\parallel \right\rangle}. \tag{3.10}$$

3.6.3 Radial thermal diffusivity

As has been established, the plasma is in the collisional regime, meaning that the radial thermal diffusivity χ_r is given by (3.8). Figure 3.5 shows that it ranges from ~ 0.02 to $\sim 0.04\,\mathrm{m}^2\,\mathrm{s}^{-1}$. This is much lower than the anamalous values measured experimentally on MAST of $\sim 1\,\mathrm{m}^2\,\mathrm{s}^{-1}$. Therefore, no reduction in temperature should be expected, in line with experimental results.

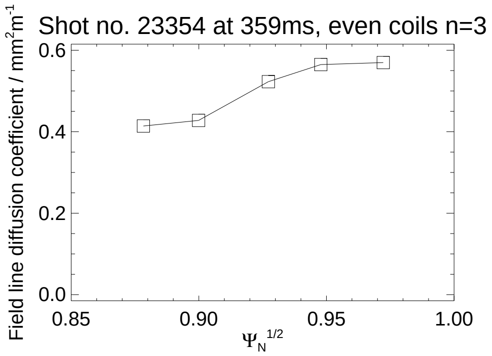

Figure 3.4 Radial profile for D_{FL}.

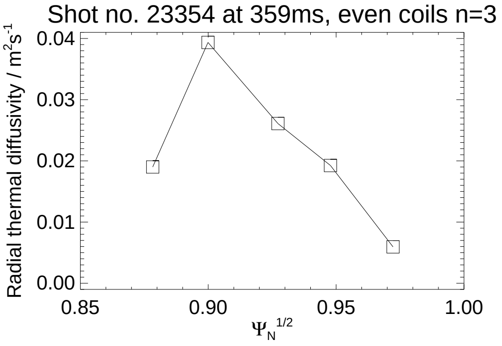

Figure 3.5 Radial profile for the value of χ_r predicted by the Rechester–Rosenbluth theory.

3.7 Summary

Radial profiles for the Kolmogorov length L_{K}, the field line dispersion coefficient D_{FL} and hence the radial thermal conductivity χ_r were obtained for the edge of a MAST L-mode plasma using vacuum modelling with the ERGOS code. The plasma discharge used was chosen for being a good example of density pump-out, suggesting that a stochastic field had formed within the plasma, in which case the Rechester–Rosenbluth theory would be applicable.

The values that were obtained for the radial thermal diffusivity are much lower than the anomalous values measured experimentally on MAST, meaning that no reduction in temperature should be expected. This is in agreement with experimental results.

The values that the Rechester–Rosenbluth theory gives for χ_r are much lower in the collisional regime than in the collisionless regime. The edge of MAST plasmas is always cold enough that the mean free path is quite short ($\lambda \propto T^2/n$) [52], so it might reasonably be expected that the collisional regime is always applicable on MAST and that the Rechester–Rosenbluth theory would always predict a value of χ_r lower than the anomalous values observed experimentally.

In H-mode plasmas, anomalous transport is lower than in L-mode, while the edge temperature (and hence both v_{th} and λ) is higher. This raises the possibility that the predicted value of χ_r could be greater than the anomalous experimental value. However, on MAST, the mean free path in H-mode is still not long enough for the plasma edge to be in the collisionless regime, so only a small increase in the predicted value of χ_r would be expected. In any case, this analysis was not carried out for H-mode because at the time, RMPs had not been observed to have an effect on MAST H-mode plasmas. However, it is possible that the predicted value of χ_r could be greater than the anomalous experimental value for an H-mode plasma in a tokamak with hotter plasmas. In that case, a decrease in the temperature profile would be expected.

Chapter 4

Stochastic magnetic fields formed by the application of RMPs

4.1 Density pump-out in MAST experiments

In this chapter, an analysis of the magnetic field structures formed by the application of $n = 3$ RMPs on MAST, including various parameters characterizing the degree of stochasticity in the plasma edge, is presented. Values for these parameters are calculated and compared with the amount of density pump-out observed in MAST experiments.

RMPs produced by the ELM coils were applied in L- and H-mode connected double-null (CDN) and lower single-null (LSN) discharges in both even parity (where fields produced by the upper and lower coils at the same toroidal location have the same sign) and odd parity (where fields produced by the upper and lower coils have opposite signs) coil configurations. The line-averaged electron density n_{e} was measured using interferometry, and densities in discharges with applied RMPs were compared to those in otherwise identical discharges without RMPs in order to test for density pump-out. Changes in line-averaged density as low as $\Delta n_\mathrm{e} = 5 \times 10^{17}\,\mathrm{m}^{-3}$ could be reliably detected using this method.

It has been found that the effects of RMPs on the plasma may depend on β_N or collisionality ν^* [43, 53]. For the L-mode plasmas presented here, $0.9 \leq \beta_\mathrm{N} \leq 2.8$ and $0.4 \leq \nu^*(\Psi_\mathrm{N} = 0.95) \leq 4.9$. For the H-mode plasmas, $3.4 \leq \beta_\mathrm{N} \leq 4.3$ and $0.14 \leq \nu^*(\Psi_\mathrm{N} = 0.95) \leq 0.18$, where Ψ_N is the normalized poloidal flux. These values of β_N can be compared with the no-wall limit of $\beta_\mathrm{N} = 4.25$ and the ideal-wall limit of $\beta_\mathrm{N} = 5.45$ for $n = 1$ modes, as calculated using the MISHKA-1 linear ideal MHD stability code [54].

Various parameters used to quantify the degree of stochasticity in the plasma edge were calculated using ERGOS and compared with the experimentally observed density pump-out. Calculations for some of these parameters involved field line tracing, which was performed using a Runge–Kutta algorithm. It should be noted that the number of discharges presented here is fairly small. However, although their spread is limited, all of the discharges were repeated to ensure that the results obtained were reproducible.

In all tokamaks, small misalignments and imperfections in the vessel can be sources of undesirable non-axisymmetric magnetic fields, known as error fields. These error fields – and in particular their $n = 1$ and $n = 2$ components, which can penetrate deep into the plasma – can lead to detrimental effects such as locked modes (see chapter 6). In order to mitigate such effects, MAST is equipped with a set of four ex-vessel error field correction coils (EFCCs), which are designed to produce a field that at least partially cancels the intrinsic error field.

Since the fields produced by EFCCs represent non-axisymmetric perturbations to the magnetic field, they may also be used as RMPs. In fact, ELM mitigation on JET was achieved using EFCCs [41, 42]. Therefore, both the intrinsic error field and the field produced by the EFCCs could influence the effect that RMPs have on MAST plasmas. In addition to the field produced by the ELM coils, all of the calculations presented in this chapter included both the field produced by the EFCCs and an estimate for the intrinsic error field. This estimate for the intrinsic error field was obtained by using a Hall probe to measure the radial, toroidal and vertical components of the magnetic field at different toroidal locations and calculating the distortion of the main poloidal field coils (P4/P5 coils) that would produce this field. Figure 4.1 shows poloidal cross-sections of the dominant Fourier harmonics of the field produced by the ELM coils and the field that results from the superposition of the field produced by the EFCCs and the estimate for the instrinsic error field, normalized to the value of the equilibrium magnetic field. It can be seen that the maximum value of the field produced by the ELM coils is around 0.3 % of the equilibrium toroidal field, compared to around 0.1 % for the field produced by the EFCCs and the intrinsic error field. The magnitude of the resonant component of the fields depends on the plasma configuration but is always somewhat lower (see section 4.2.2).

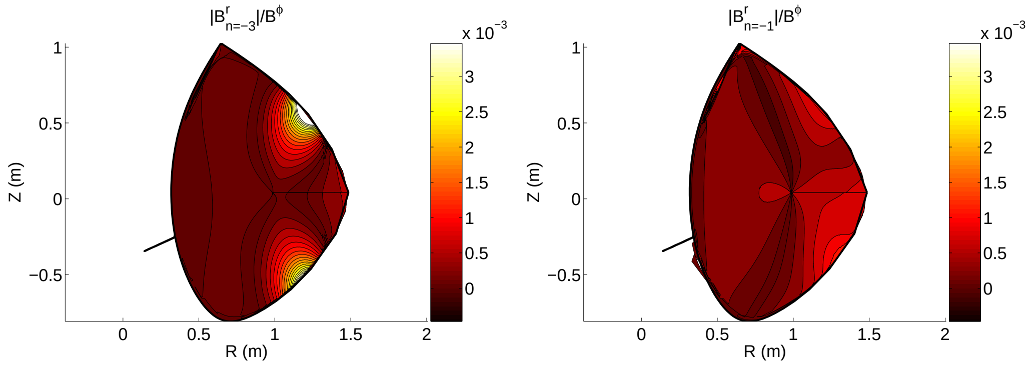

(a) (b)

Figure 4.1 Poloidal cross-sections of the dominant Fourier harmonics of (a) the field produced by the ELM coils and (b) the superposition of the field produced by the EFCCs and the estimate for the intrinsic error field, normalized to the value of the equilibrium magnetic field.

As charged particles travel along the field lines, they will pass through a region of higher magnetic field strength on the inboard side – known as the high-field side (HFS) – and a region of lower magnetic field strength on the outboard side – known as the low-field side (LFS) – of the tokamak. For the particles that have insufficient velocity parallel to the magnetic field, this change in magnetic field strength experienced by the particles acts as a magnetic mirror, and these particles become trapped on the LFS [55]. The presence of these trapped particles, combined with a radial density gradient, gives rise to a self-generated toroidal current in the plasma, known as the 'bootstrap current' [56]. This current will produce a poloidal magnetic field, altering the magnetic field structure. Therefore, since there is a considerable density gradient in the edge of H-mode plasmas, the bootstrap current might be expected to have a significant effect on the magnetic field structure in H-mode ERGOS calculations. However, a previous study [57] has shown the effect to be small, so the bootstrap current was not included in the EFIT equilibria used.

4.2 Vacuum modelling using ERGOS

4.2.1 Chirikov parameter

The Chirikov parameter $\sigma_{\mathrm{Chirikov}}$ is a measure of the overlap between two adjacent magnetic islands. It is defined as

$$\sigma_{\mathrm{Chirikov}} = \frac{\delta_1 + \delta_2}{\Delta_{1,\,2}}, \tag{4.1}$$

where δ_1 and δ_2 are the half-widths of adjacent magnetic islands and $\Delta_{1,\,2}$ is the distance between these islands in terms of the normalized radius $\Psi_{\mathrm{N}}^{1/2}$ [11]. It can be seen from the definition of $\sigma_{\mathrm{Chirikov}}$ that when $\sigma_{\mathrm{Chirikov}} > 1$, adjacent magnetic islands overlap and a stochastic field is formed.

The Chirikov parameter was calculated using vacuum modelling. Traditionally, only the magnetic islands formed by the dominant toroidal mode number have been used in calculations of $\sigma_{\mathrm{Chirikov}}$. This is because toroidal harmonics of different amplitudes can create islands of considerably different size, as can be seen in figure 4.2. If two magnetic islands have a considerably smaller

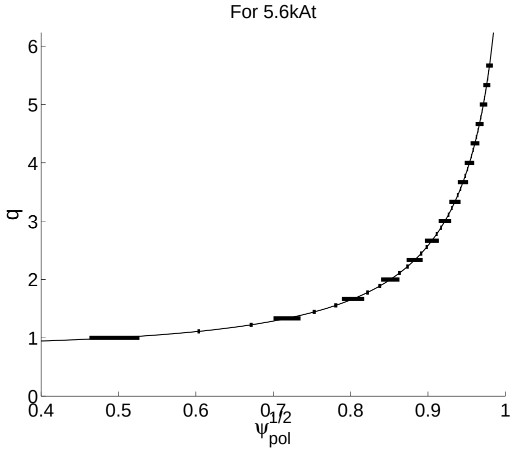

Figure 4.2 Radial profile of the saftey factor q with the widths of $n = 3$ and $n = 9$ (the harmonics of the field produced by the ELM coils with the largest amplitudes) islands shown as horizontal bars. The $n = 9$ islands are very narrow.

magnetic island situated between them, the values for $\sigma_{\mathrm{Chirikov}}$ obtained from (4.1) may be significantly lower than the value that would be obtained in the absence of the smaller island, as shown in figure 4.3. This is contradictory to the use of $\sigma_{\mathrm{Chirikov}}$ as a measure of the degree of stochasticity – the addition of a magnetic island cannot cause the field to become less stochastic, but it can result in lower values of $\sigma_{\mathrm{Chirikov}}$. Considerable variation in island width can also make the definition of ‘adjacent magnetic islands’ ambiguous since different pairs of islands may be considered adjacent depending on whether the locations of the island centres or of the island edges are used.

For these reasons, the values for $\sigma_{\mathrm{Chirikov}}$ given here were calculated using only $n = 3$ islands since this corresponds to the dominant toroidal mode number of the RMPs produced by the coil configurations used in these discharges. This ensures that nearby magnetic islands are all of a similar size, so these complications do not arise.

The width of the stochastic region was defined as the range of Ψ_{N} over which $\sigma_{\mathrm{Chirikov}} > 1$. Figure 4.4 shows how the change in electron density Δn_{e} normalized to the density n_{e} before the onset of pump-out varies with the width of the stochastic region. It can be seen that, for L-mode plasmas,

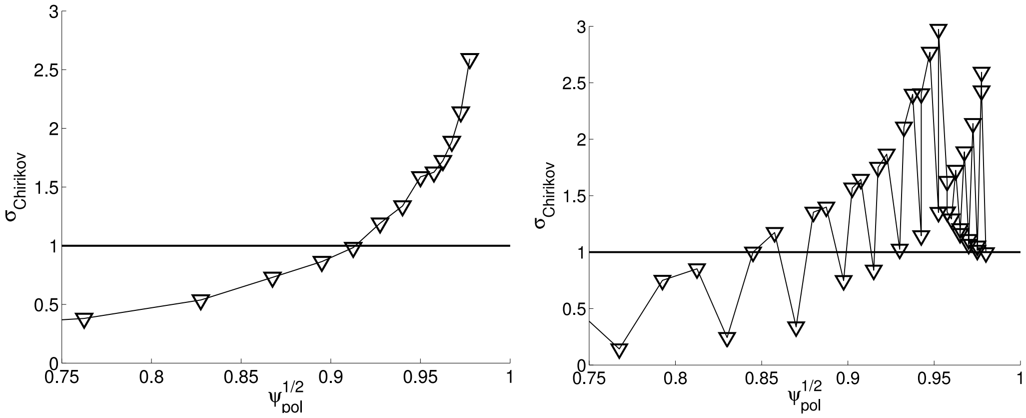

(a) (b)

Figure 4.3 Radial profiles for σ_{Chirikov} including (a) only $n = 3$ magnetic islands and (b) $n = 3$ and $n = 9$ (the harmonic of the field produced by the ELM coils with the second-largest amplitude) magnetic islands. The inclusion of more toroidal mode numbers with smaller magnetic islands causes the profile of σ_{Chirikov} versus $\Psi_{\text{N}}^{1/2}$ to contain more fluctuations.

density pump-out is well correlated with the width of the stochastic region. However, there is a poor correlation between the stochastic width and the occurrence of pump-out in H-mode.

4.2.2 Effective radial resonant field component

The effective radial resonant field component of the nth toroidal harmonic of the perturbed magnetic field normalized to the toroidal equilibrium magnetic field is given by

$$b^r_{\text{res}} = \frac{2\left|b^1_{m=qn,\,n}\right|}{R_0\left\langle\left|\boldsymbol{\nabla}\Psi_{\text{N}}^{1/2}\right|\right\rangle}, \tag{4.2}$$

where R_0 is the major radius, $\langle|\boldsymbol{\nabla}\Psi_{\text{N}}^{1/2}|\rangle$ is the average value of $|\boldsymbol{\nabla}\Psi_{\text{N}}^{1/2}|$ over an equilibrium flux surface and $b^1_{m=qn,\,n}$ is the resonant Fourier component in the spectrum of b^1, where b^1 is the component of the perturbed magnetic field perpendicular to the equilibrium flux surfaces normalized to the toroidal

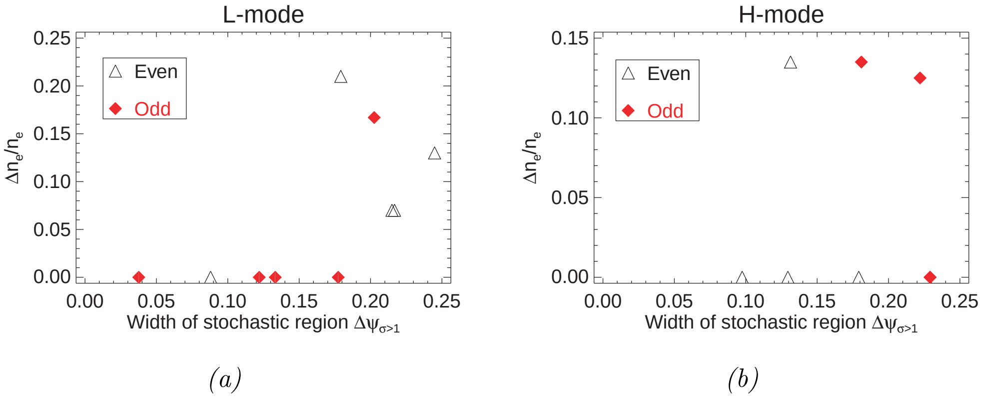

Figure 4.4 Density pump-out versus the width of the stochastic region defined as the range of Ψ_N over which $\sigma_{\text{Chirikov}} > 1$ for (a) L- and (b) H-mode plasmas. Open triangles represent discharges with even parity coil configurations; filled diamonds represent those with odd parity coil configurations.

equilibrium magnetic field, i.e.

$$b^1 = \frac{\boldsymbol{B}_1 \cdot \boldsymbol{\nabla}\Psi_{\mathrm{N}}^{1/2}}{\boldsymbol{B}_0 \cdot \boldsymbol{\nabla}\phi}, \tag{4.3}$$

where $\boldsymbol{B}_0$ and $\boldsymbol{B}_1$ are the equilibrium and perturbed magnetic field vectors respectively and ϕ is the toroidal angle [11].

b^r_{res} was calculated using vacuum modelling. It is unclear how to produce a meaningful figure based on values of b^r_{res} for a combination of different toroidal mode numbers, so only the dominant $n = 3$ toroidal mode number of the RMPs was used. A figure of merit for the effective radial resonant field component was obtained by taking the value of b^r_{res} at $\Psi_{\mathrm{N}}^{1/2} = 0.98$. This value was chosen because b^r_{res} can suddenly spike, drop or oscillate rapidly for greater values of $\Psi_{\mathrm{N}}^{1/2}$, as can be seen in figure 4.5. This is believed to be due to numerical error. Figure 4.6 shows that b^r_{res} is a reasonable indicator of density pump-out, especially in H-mode, where pump-out is more likely to occur when b^r_{res} exceeds $\sim 6 \times 10^{-4}$.

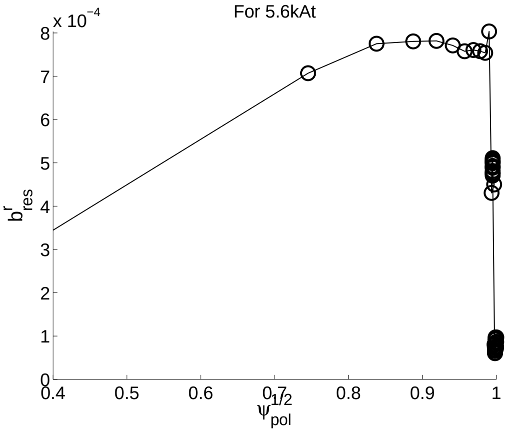

Figure 4.5 Radial profile for b^r_{res}, showing a steady increase throughout the plasma followed by a sharp drop at the very edge, which is not physical. Values for b^r_{res} were taken at $\Psi_{\mathrm{N}}^{1/2} = 0.98$ in order to avoid such numerical effects.

4.2.3 Width of the laminar region

The perturbed region in the plasma edge can be considered to consist of two distinct domains: a stochastic region and a laminar region. The stochastic region, located a little way inside the LCFS, contains magnetic field lines whose connection length L_{c} to the divertor is longer than the Kolmogorov length L_{K}, i.e. the field lines are confined to the plasma for longer than the scale length over which they separate from each other [58]. In contrast, the laminar region, located at the very edge of the plasma, contains some field lines for which $L_{\mathrm{c}} < L_{\mathrm{K}}$, i.e. these field lines leave the plasma more rapidly than they separate from each other.

Parallel flows along short open field lines to the divertor are expected to lead to increased transport [59]. In plasmas with wider laminar regions, a greater fraction of the plasma volume is connected to the divertor by these open field lines, and the average density within this volume is higher. Therefore, the width of the laminar region is expected to be correlated with the amount of density pump-out.

A sufficient number of field lines must be followed in order to obtain good

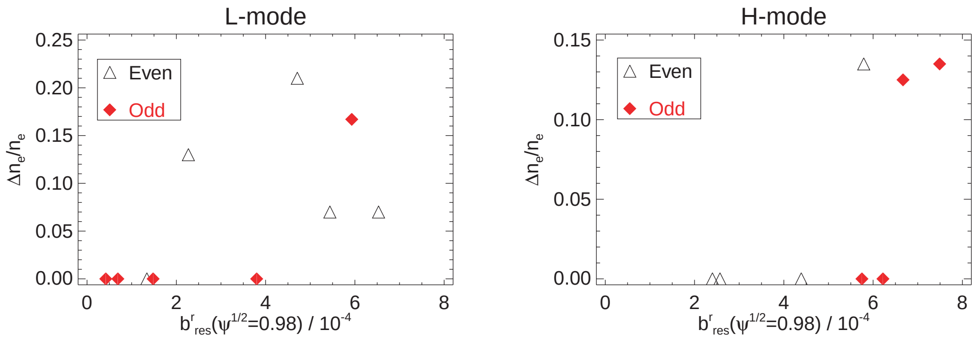

(a) *(b)*

Figure 4.6 Density pump-out versus the value of b^r_{res} at $\Psi_{\mathrm{N}}^{1/2} = 0.98$ for (a) L- and (b) H-mode plasmas. Open triangles represent discharges with even parity coil configurations; filled diamonds represent those with odd parity coil configurations.

statistics. For the width of the laminar region, only field lines that leave the plasma and reach the divertor are of interest, so the field lines were started on the divertor. For other metrics, radial profiles were obtained, so the field lines were started on equilibrium flux surfaces.

The width of the laminar region was calculated by tracing 10 000 field lines from the lower divertor for a length of 100 m, which is a typical value given by vacuum modelling for L_{K} in the edge of MAST plasmas with applied RMPs. By plotting the deepest radius that each field line reaches as a function of the co-ordinates of its starting point, divertor strike-point patterns can be generated, as seen in figure 4.7 (a). In this case, the colour of each point represents the lowest value of $\Psi_{\mathrm{N}}^{1/2}$ that was reached by the corresponding field line. With the application of RMPs, the strike-point patterns produced from field line tracing are split into multiple finger-like structures called lobes. This effect is known as strike-point splitting. Similar strike-point patterns are also observed experimentally as in figure 4.7 (b). The calculations were performed in cylindrical polar co-ordinates with 1000 toroidal discretization points.

The innermost extent of the laminar region was defined as the deepest pen-

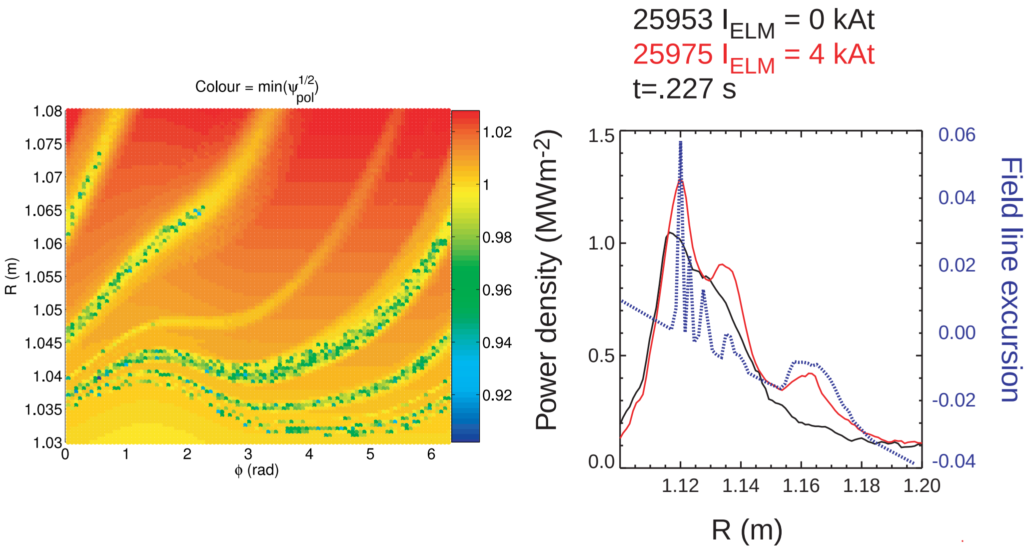

(a) *(b)*

Figure 4.7 (*a*) Divertor strike-point pattern produced by field line tracing. (*b*) Experimentally observed strike-point profiles at a single toroidal angle (solid lines). With the application of ELM coils (red solid line), strike-point splitting causes additional peaks to appear at the same locations as peaks in the excursion of traced field lines (dotted line).

etration of any of the field lines into the plasma. Figure 4.8 shows that, for L-mode plasmas, both the occurrence and amount of density pump-out are strongly correlated with the width of the laminar region. The laminar width is also a reasonable indicator of density pump-out in H-mode, with pump-out being more likely to occur when the width exceeds ~ 0.15.

4.2.4 Field line loss fraction

Another method of quantifying the degree of stochasticity in the plasma edge involves using vacuum modelling to trace field lines from a given equilibrium flux surface over a given length and noting the fraction of field lines lost from the plasma. The value of this field line loss fraction depends on the length over which the field lines are traced. In [60], it was found that on DIII-D, once the field lines had been followed for ~ 200 toroidal turns, any further

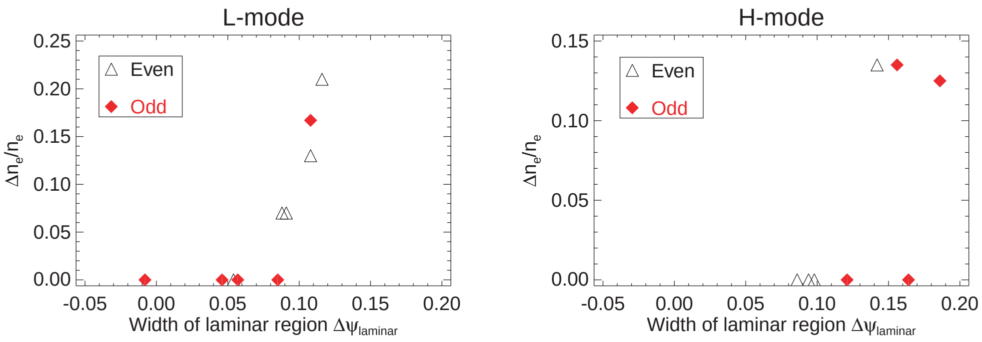

(a) (b)

Figure 4.8 Density pump-out versus the width of the laminar region defined as the deepest penetration of field lines into the plasma for (*a*) L- and (*b*) H-mode plasmas. Open triangles represent discharges with even parity coil configurations; filled diamonds represent those with odd parity coil configurations.

increase in the field line loss fraction with the length over which the field lines were traced was small, so the field lines were traced for 200 toroidal turns. For consistency with [60], field lines were also traced for 200 toroidal turns here. In order to test the effect of this value, field lines were traced for 400 toroidal turns and a poloidal cross-section of L_c was plotted (figure 4.9). It can be seen that $L_c < 200$ toroidal turns for most of the field lines lost from the very edge of the plasma, so these field lines are still counted as lost when only traced for 200 toroidal turns. However, most of the field lines lost from a little further into the plasma have $L_c > 200$ toroidal turns, so these field lines are not counted as lost. Consequently, tracing field lines for 200 toroidal turns results in the integrated field line loss fraction being more sensitive to field line loss from the very edge of the plasma.

In order to calculate the field line loss fraction for n_{tor} toroidal turns, where for the results given here $n_{\mathrm{tor}} = 200$, each field line was initially traced in the anti-clockwise (co-current) toroidal direction as viewed from above (the toroidal field is in the clockwise direction), either until it completed $\frac{1}{2}n_{\mathrm{tor}}$ toroidal turns or until lost from the plasma. It would then be traced from its starting point in the clockwise toroidal direction either until it completed

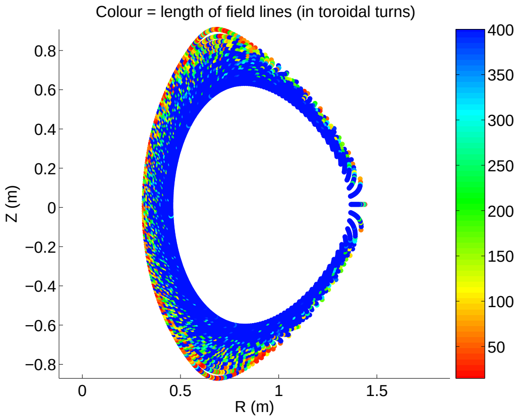

Figure 4.9 Poloidal cross-section of L_c.

n_{tor} toroidal turns in total (i.e. the number of toroidal turns completed in the clockwise direction plus the number of toroidal turns previously completed in the anti-clockwise direction) or until lost from the plasma. If the field line was lost in the clockwise direction but not in the anti-clockwise direction, it would then be traced further in the anti-clockwise direction either until it completed n_{tor} toroidal turns in total or until it was also lost in the anti-clockwise direction. Therefore, a field line that remains within the LCFS would be followed for $\frac{1}{2}n_{\mathrm{tor}}$ toroidal turns in each direction, making n_{tor} toroidal turns in total, whereas a field line lost immediately in one direction would be followed either for n_{tor} toroidal turns in the other direction or until it was also lost in that direction. Hence three values for the field line loss fraction were obtained – one for the fraction of field lines lost in the clockwise direction, one for the fraction lost in the anti-clockwise direction and one for the fraction lost in either the clockwise or the anti-clockwise direction (inclusive disjunction).

Figure 4.10 shows radial profiles for the three different field line loss fractions after 200 and 400 toroidal turns. It can be seen that there is little difference between the fraction of field lines lost in the clockwise direction and the fraction lost in the anti-clockwise direction. For the remainder of this thesis, ‘field line loss fraction’ will refer only to the fraction of field lines lost in either direction after 200 toroidal turns. As with the width of the laminar region, the field line tracing for the field line loss fraction was performed in cylindrical polar co-ordinates with 1000 toroidal discretization points.

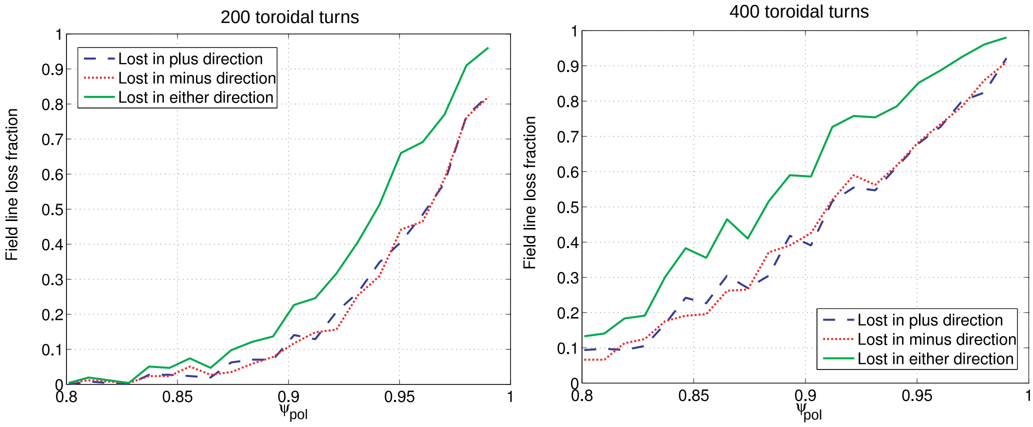

(a) (b)

Figure 4.10 Radial profiles for the fraction of field lines lost after (*a*) 200 and (*b*) 400 toroidal turns. The ‘plus direction’ is anti-clockwise and the ‘minus direction’ is clockwise as viewed from above.

A figure of merit for the field line loss fraction was obtained by integrating the fraction of field lines lost in either direction after 200 toroidal turns over Ψ_{N} from $\Psi_{\mathrm{N}}^{1/2} = 0.895$ to $\Psi_{\mathrm{N}}^{1/2} = 0.995$ (the closest data point to the LCFS), i.e. from $\Psi_{\mathrm{N}} \approx 0.80$ to $\Psi_{\mathrm{N}} \approx 0.99$:

$$\int_{\Psi_{\mathrm{N}}^{1/2}=0.895}^{0.995} \frac{N_{\mathrm{lost}}\left(\Psi_{\mathrm{N}}\right)}{N_0\left(\Psi_{\mathrm{N}}\right)} d\Psi_{\mathrm{N}}, \tag{4.4}$$

where $N_0(\Psi_{\mathrm{N}})$ is the number of field lines started on a given flux surface and $N_{\mathrm{lost}}(\Psi_{\mathrm{N}})$ is the number of those field lines that are lost from the plasma within 200 toroidal turns. Integrating the field line loss fraction over this region has no physical significance, but the result is directly proportional to the mean value of the field line loss fraction over this region. Figure 4.11 shows that the plots for the integrated field line loss fraction resemble those for b^r_{res}, both parameters being reasonable indicators of density pump-out, especially in H-mode, where pump-out is more likely to occur when the integrated field line loss fraction exceeds ~ 0.16.

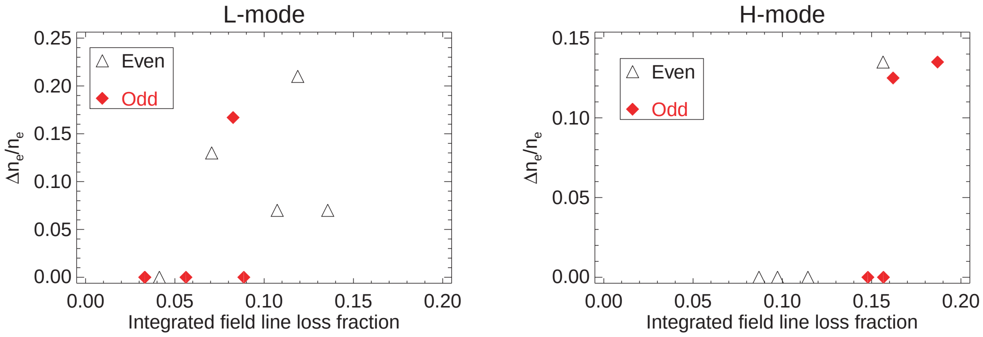

(a) *(b)*

Figure 4.11 Density pump-out versus the field line loss fraction integrated over Ψ_N from $\Psi_\mathrm{N}^{1/2} = 0.895$ to $\Psi_\mathrm{N}^{1/2} = 0.995$ for (a) L- and (b) H-mode plasmas. Open triangles represent discharges with even parity coil configurations; filled diamonds represent those with odd parity coil configurations.

4.2.5 Field line dispersion

By defining the field line dispersion coefficient D_FL as $\langle(\Delta r)^2\rangle/(2\langle L_\parallel\rangle)$ and by tracing field lines from different equilibrium flux surfaces, two-dimensional plots of D_FL as a function of radius and number of toroidal turns can be produced as in figure 4.12. From Poincaré plots such as figure 2.5 (b), it is apparent that the formation of magnetic islands corresponds to the radial displacement of field lines. Since magnetic islands form on rational surfaces, field line dispersion might therefore be expected to be increased in the vicinity of rational surfaces. This effect can be observed as the horizontal bands in figure 4.12. As in section 3.6, the field line tracing was performed in field-aligned co-ordinates.

As discussed in section 3.4 and shown in figure 3.2, in fields that are not fully stochastic, the radial excursion of field lines only follows a truly random walk process (i.e. $\langle(\Delta r)^2\rangle \propto L_\parallel$) over a certain number of toroidal turns, after which $\langle(\Delta r)^2\rangle$ increases more slowly and eventually levels off, i.e.

$$\lim_{L_\parallel\to\infty} \frac{\langle(\Delta r)^2\rangle}{2\left\langle L_\parallel\right\rangle} = 0. \tag{4.5}$$

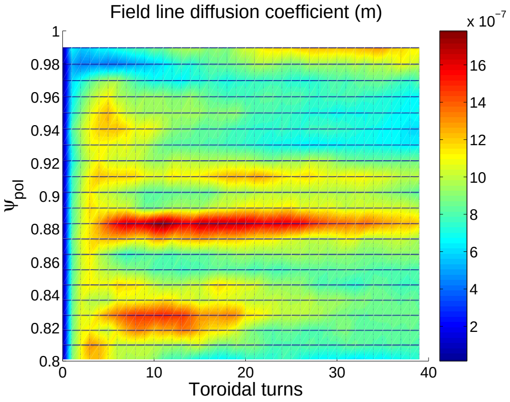

Figure 4.12 D_{FL} as a function of Ψ_{N} and number of toroidal turns.

Therefore, taking the value of D_{FL} for $L_{\|} \to \infty$ would not result in a meaningful figure of merit. However, obtaining a value representative of the local field line dispersion at each radial location would be useful. The value chosen was the maximum value of D_{FL} for each radial location in plots like figure 4.12, excluding the value after only a single toroidal turn. It can be seen that in figure 3.2, this value is approximately equal to the gradient of the linear part of the curve.

Radial profiles for the field line dispersion coefficient were produced as in figure 4.13. These profiles contain peaks corresponding to increased field line dispersion in the vicinity of rational surfaces due to the presence of magnetic islands. If such a region of high field line dispersion consists mainly of short open field lines, this field line dispersion could lead to increased transport due to parallel flows along these open field lines. Conversely, if a region of high field line dispersion consists mainly of closed field lines, the field line dispersion is likely to lead to increased field line mixing but not necessarily to increased transport or density pump-out.

A figure of merit for the field line dispersion coefficient was obtained by integrating over Ψ_{N} from $\Psi_{\mathrm{N}}^{1/2} = 0.895$ to $\Psi_{\mathrm{N}}^{1/2} = 0.995$ as for the field line loss fraction:

$$\int_{\Psi_{\mathrm{N}}^{1/2}=0.895}^{0.995} D_{\mathrm{FL,\,max}}\left(\Psi_{\mathrm{N}}\right) d\Psi_{\mathrm{N}}, \tag{4.6}$$

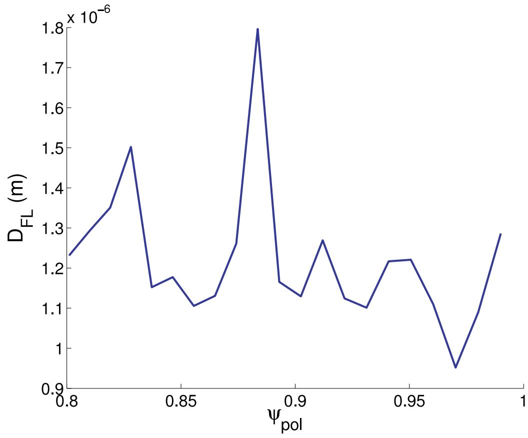

Figure 4.13 Radial profile for D_{FL}. The peaks show the increased field line dispersion in the vicinity of rational surfaces.

where $D_{\mathrm{FL,\,max}}(\Psi_{\mathrm{N}})$ is the maximum value of D_{FL} for a given Ψ_{N}. In order to include the effect of the fraction of open field lines, an additional figure of merit was obtained by multiplying the field line dispersion coefficient by the field line loss fraction to obtain a weighted field line dispersion coefficient and integrating over the same range of Ψ_{N}:

$$\int_{\Psi_{\mathrm{N}}^{1/2}=0.895}^{0.995} \frac{N_{\mathrm{lost}}\left(\Psi_{\mathrm{N}}\right)}{N_0\left(\Psi_{\mathrm{N}}\right)} D_{\mathrm{FL,\,max}}\left(\Psi_{\mathrm{N}}\right) d\Psi_{\mathrm{N}}. \tag{4.7}$$

As with the field line loss fraction, integrating over this region has no physical significance, but the result is directly proportional to the mean value over this region. Figures 4.14 and 4.15 show that there is a poor correlation between the occurrence of pump-out and the value of the field line dispersion coefficient or the weighted field line dispersion coefficient in both L- and H-mode.

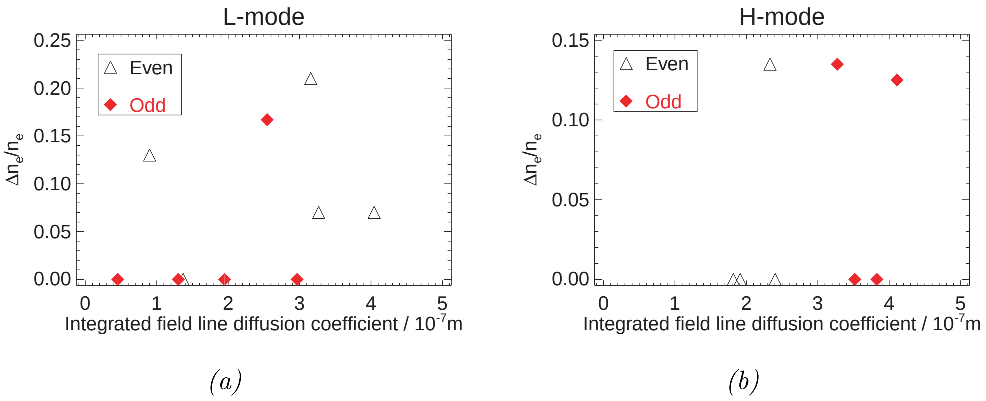

(a) (b)

Figure 4.14 Density pump-out versus D_{FL} integrated over Ψ_{N} from $\Psi_{\mathrm{N}}^{1/2} = 0.895$ to $\Psi_{\mathrm{N}}^{1/2} = 0.995$ for (a) L- and (b) H-mode plasmas. Open triangles represent discharges with even parity coil configurations; filled diamonds represent those with odd parity coil configurations.

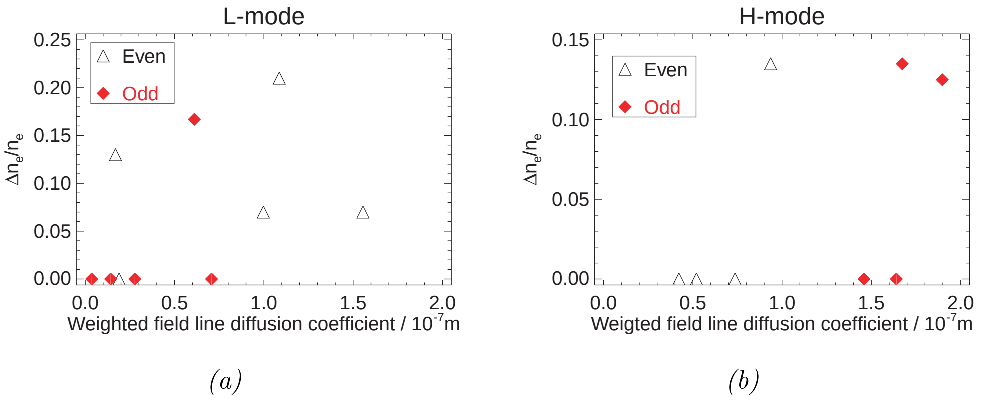

(a) (b)

Figure 4.15 Density pump-out versus D_{FL} weighted by the field line loss fraction integrated over Ψ_{N} from $\Psi_{\mathrm{N}}^{1/2} = 0.895$ to $\Psi_{\mathrm{N}}^{1/2} = 0.995$ for (a) L- and (b) H-mode plasmas. Open triangles represent discharges with even parity coil configurations; filled diamonds represent those with odd parity coil configurations.

4.3 Plasma response modelling using MARS-F

Since ERGOS is a vacuum code, it does not take into account any interaction between the plasma and the RMPs. In reality, the external magnetic fields drive currents in the plasma, which then generate additional magnetic fields that interact with the RMPs. In addition, the rotation of the plasma means that any interaction between an external perturbation and a particular 'packet' of plasma will vary over time and will therefore be averaged out to some extent. These two effects generally lead to the screening of external perturbations, although amplification can also occur [61].

The ideal MHD response to external magnetic fields is complete screening at corresponding rational surfaces and complete suppression of magnetic islands [62]. Therefore, resistive MHD is necessary for calculating a meaningful plasma response to external perturbations. MARS-F uses linear, single-fluid, resistive MHD equations to calculate the plasma response to RMPs in full toroidal geometry, including screening effects due to toroidal rotation [61]. MARS-F was used to calculate the plasma displacement $\boldsymbol{\xi}(\Psi_\mathrm{N}, \theta, \phi)$, where Ψ_N, θ and ϕ are the radial, poloidal and toroidal co-ordinates respectively. The component of the plasma displacement normal to the equilibrium flux surfaces is given by

$$\xi_\mathrm{n}\left(\Psi_\mathrm{N}, \theta\right) \mathrm{e}^{in\phi} = \boldsymbol{\xi}\left(\Psi_\mathrm{N}, \theta, \phi\right) \cdot \hat{\boldsymbol{a}}, \tag{4.8}$$

where n is the toroidal mode number of the perturbation and $\hat{\boldsymbol{a}}$ is the unit vector normal to the equilibrium flux surface. Figure 4.16 shows how $\xi_\mathrm{n}(\Psi_\mathrm{N} = 1)$ varies with θ for even parity and odd parity coil configurations for an L-mode connected double-null discharge with plasma current $I_\mathrm{P} = 400\,\mathrm{kA}$ and $q_{95} = 6.0$. In this case, the even parity coil configuration produces a poloidal profile for ξ_n with maxima near the X-points, whereas the odd parity configuration produces a poloidal profile with a maximum near the LFS midplane ($\theta = 0$). The location of these peaks does not simply depend on the parity of the coil configuration – for some discharges, the odd parity coil configuration produces peaks near the X-points while the even parity configuration produces a peak near the LFS midplane [62].

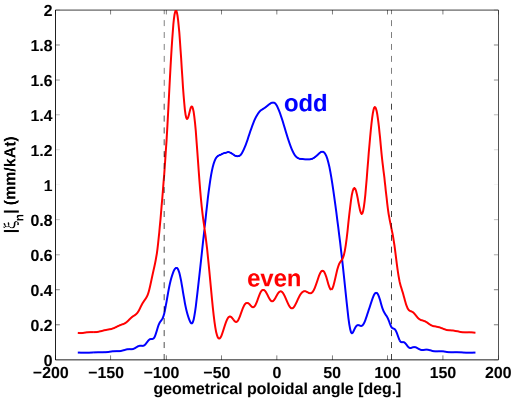

Figure 4.16 $\xi_\mathrm{n}(\Psi_\mathrm{N} = 1)$ as a function of geometric poloidal angle for even and odd parity coil configurations for an L-mode connected double-null discharge with plasma current $I_\mathrm{P} = 400\,\mathrm{kA}$ and $q_{95} = 6.0$. The dashed lines mark the locations of the X-points.

Figure 4.17 shows a plot of the amount of density pump-out as a function of the ratio of the value of ξ_n at the X-point peaks to its value at the LFS midplane. It can be seen that whenever this ratio exceeds ~ 1.5, density pump-out occurs, and that pump-out only occurs when this is the case. This criterion is a robust indicator of density pump-out and applies both to L- and H-mode plasmas [62]. There is only a weak correlation between the value of this ratio and the amount of density pump-out, but the amount of pump-out might be expected to be correlated with the magnitude of ξ_n at the X-point peaks rather than with this ratio. Furthermore, the value of this ratio does not depend on the strength of the perturbation. In the cases where the ratio exceeds ~ 1.5, density pump-out would not occur if the ELM coil current were reduced sufficiently, but the value of the ratio would remain unchanged. Therefore, it seems likely that this ratio represents a necessary but not sufficient condition for density pump-out.

MARS-F calculations of the poloidal harmonics triggered by the application of RMPs have revealed that these X-point peaks only occur when high-m

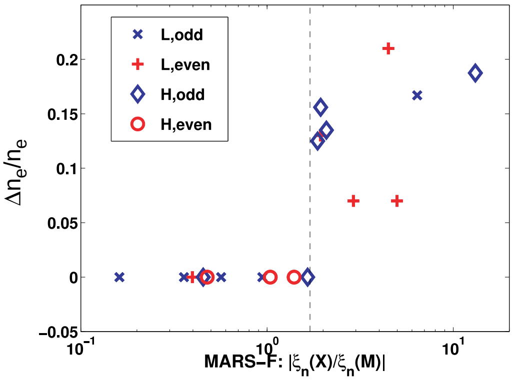

Figure 4.17 Density pump-out as a function of the ratio of the value of ξ_n at the X-point peaks to its value at the LFS midplane.

peeling-like modes are present, whereas LFS midplane peaks tend to occur when kink-like modes are present. A full explanation as to why these X-point peaks should lead to density pump-out would have to include particle transport mechanisms [62].

4.4 Summary

In MAST experiments with applied $n = 3$ RMPs, clear density pump-out has been observed in a wide range of L-mode plasmas and a few H-mode plasmas. The occurrence of pump-out is correlated to varying degrees with a range of measures of the level of stochasticity in the plasma edge, as calculated using vacuum modelling with ERGOS. Pump-out can be obtained in L-mode at lower values of these metrics than in H-mode.

None of these measures provides a single threshold value for pump-out that applies to both L- and H-mode plasmas. The only parameter to show a correlation with the amount of density pump-out is the width of the laminar region, and then only for L-mode plasmas.

In every case where there is some correlation between one of these parameters and the occurrence of density pump-out, the threshold value for pump-out is significantly higher for H-mode than for L-mode. This may be due to the fact that vacuum modelling does not include any screening of the RMPs, so if screening differs between L- and H-mode, and this screening is not included, different threshold values for L- and H-mode would be expected. This screening may depend on toroidal, $\boldsymbol{E} \times \boldsymbol{B}$ and electron diamagnetic rotation [63], which would be expected to be very different in MAST L-mode plasmas compared to H-mode plasmas.

It should be noted that there are no more than ten data points in any of these plots, so more data are required in order to be able to state conclusively the strength of each correlation. Since these experiments were carried out, six additional lower coils have been installed on MAST, making a wider range of coil configurations possible. This will provide increased flexibility and the prospect of achieving good alignment between the perturbation and the equilibrium magnetic field in a wider range of plasmas. It would be interesting to perform this analysis for different coil configurations to see whether the correlations still hold.

Plasma response modelling using MARS-F provides a robust criterion for the occurrence of density pump-out that applies both to L- and H-mode plasmas. The reason MARS-F modelling provides a single threshold value for pump-out while ERGOS modelling does not may be because MARS-F includes screening, which may differ between L- and H-mode. Possibilities for further work include taking the magnetic field structure from MARS-F, which includes the plasma response, and recalculating the parameters presented in this chapter using this magnetic field to see what effect the plasma response has on the values of these parameters.

Chapter 5

Lower single-null ELM mitigation experiments with $n = 4$ and $n = 6$ RMPs

5.1 Background

Previous lower single-null ELM mitigation experiments on MAST used $n = 3$ RMPs. The application of RMPs was observed to cause smaller, more frequent ELMs accompanied by density pump-out in a limited range of plasmas. An example is shown in figure 5.1. However, the RMPs typically caused stronger rotation braking than in double-null plasmas, with the toroidal velocity falling almost to zero, as can be seen in figure 5.2. This rotation braking was not just an edge effect but occurred across the whole plasma and resulted in back-transitions to L-mode.

There are two possible causes of this rotation braking: neo-classical toroidal viscosity (NTV) and $\boldsymbol{J} \times \boldsymbol{B}$ torque. Calculations showed that NTV effects were insufficient to cause the amount of braking observed, leading to the conclusion that $\boldsymbol{J} \times \boldsymbol{B}$ torque was at least partly responsible [64]. $\boldsymbol{J} \times \boldsymbol{B}$ torque acts on resonant surfaces, so it is unsurprising that it is related to

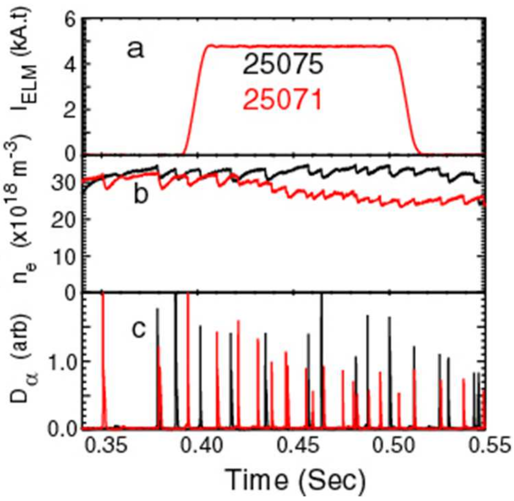

Figure 5.1 The application of $n = 3$ RMPs produced by the ELM coils (a) can lead to smaller, more frequent ELMs (c) accompanied by density pump-out (b).

RMPs. The magnitude of the $\boldsymbol{J} \times \boldsymbol{B}$ torque due to magnetic perturbations increases with increasing strength of the perturbed magnetic field.

With the six additional lower coils installed on MAST, $n = 4$ and $n = 6$ coil configurations using only the lower row of coils are now also possible. Since LSN plasmas are much closer to the lower row of coils than to the upper row, the loss of the upper coils should not greatly reduce the effect of RMPs on the plasma.

Figure 5.3 (a) shows profiles of σ_{Chirikov} for $n = 3$ (for six upper and six lower coils, and also for the twelve lower coils only), $n = 4$ and $n = 6$ coil configurations. It can be seen that the value of σ_{Chirikov} as calculated using vacuum modelling with ERGOS is greater for $n = 4$ and $n = 6$ than for $n = 3$ RMPs, suggesting that ELM mitigation may also be possible with $n = 4$ and $n = 6$ RMPs. The increased value of σ_{Chirikov} is partly due to the fact that RMPs with a greater toroidal mode number have more corresponding resonant surfaces. As a result, the resonant surfaces are closer together, which facilitates their overlapping.

Figure 5.3 (b) shows profiles of b^r_{res} for the same plasma and coil configurations

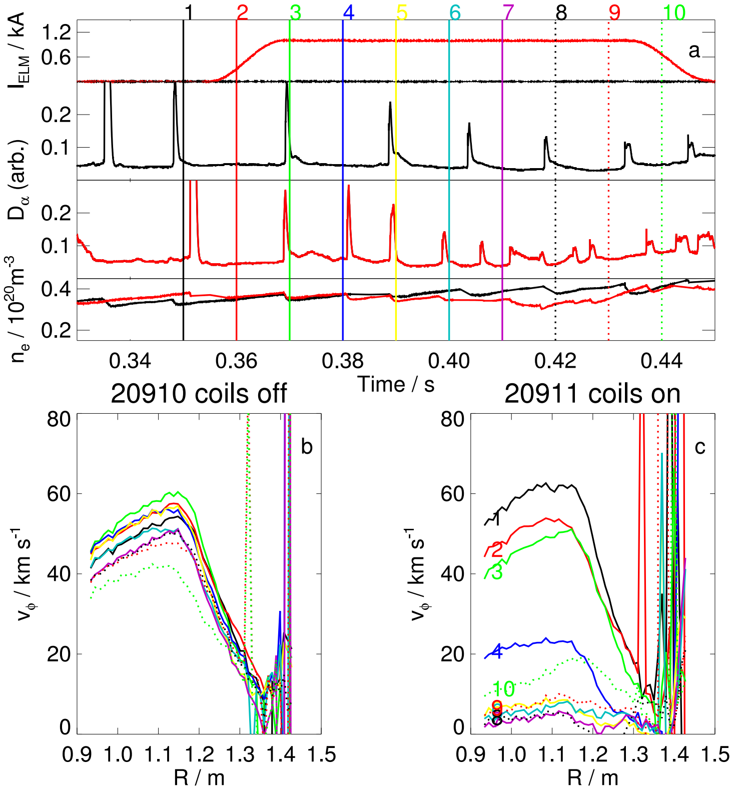

Figure 5.2 (a) Timing of the rotation measurements in relation to the application of the ELM coils and the effect on the ELMs. (b) Rotation profiles without and (c) with $n = 3$ RMPs, showing strong rotation braking across the whole plasma.

as figure 5.3 (a). It can be seen that the value of $b^r_{\rm res}$ for $n = 4$ and $n = 6$ RMPs is higher in the plasma edge but lower in the core than for $n = 3$ RMPs. This suggests that the magnitude of the $\boldsymbol{J} \times \boldsymbol{B}$ torque will also be lower in the plasma core than for $n = 3$ RMPs, so it may be expected to cause less core rotation braking. Therefore, it was hoped that experiments with $n = 4$ and $n = 6$ RMPs would lead to ELM mitigation with less severe rotation braking and would consequently avoid a back-transition to L-mode.

Figure 5.4 shows spectrum plots produced using ERGOS for a lower single-null plasma with $n = 3$ (with six upper and six lower coils, and also with the twelve lower coils only), $n = 4$ and $n = 6$ coil configurations. These spectrum plots can be thought of as a series of radial profiles for each poloidal

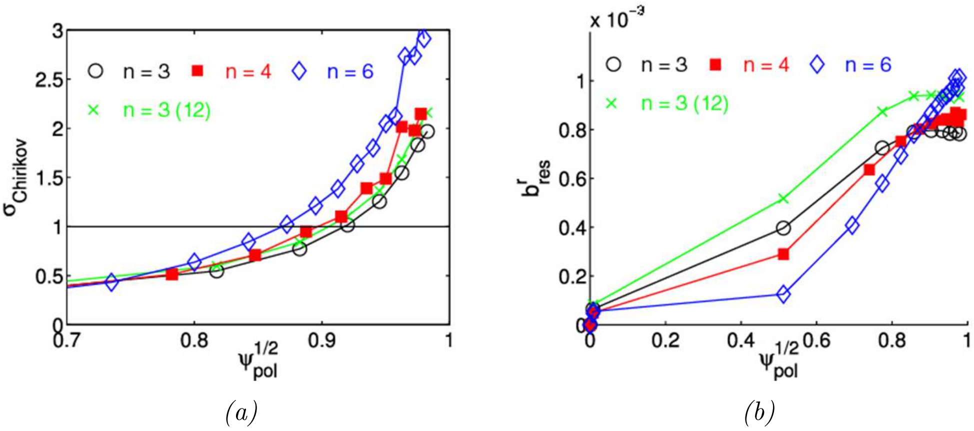

(a) (b)

Figure 5.3 Radial profiles for (a) σ_{Chirikov} and (b) b^r_{res}. Open circles represent $n = 3$ RMPs using six upper and six lower coils; filled squares represent $n = 4$ RMPs using twelve lower coils; open diamonds represent $n = 6$ RMPs using twelve lower coils; crosses represent $n = 3$ RMPs using twelve lower coils.

mode number of the magnitude of the Fourier harmonic $b^1_{m,n}$, where m is the corresponding poloidal mode number and n is the globally dominant toroidal mode number. b^1 is defined in (4.3) and is related to b^r_{res} according to (4.2). Overlaid is a curve showing the resonant poloidal mode number at each radial location, given by $m = qn$. Since only the globally dominant n is considered, it is constant and the curve is effectively the q-profile. Large values of $|b^1_{m,n}|$ directly beneath this curve correspond to large resonant components of b^1, whereas large values away from this curve correspond to large non-resonant components.

It can be seen from figure 5.4 that for $n = 3$ configurations, changing from six upper coils and six lower coils to just the twelve lower coils significantly increases the strength of both the resonant and non-resonant components of b^1 while also broadening the spectrum slightly. This overall increase in the strength of the perturbed field in the plasma is expected for this lower single-null discharge, which is much closer to the lower coils than it is to the upper coils, meaning that the average distance between the coils and the LCFS is reduced while the number of coils remains the same.

It can also be seen that as the dominant toroidal mode number of the coil configuration increases, the spectrum becomes broader and more concentrated towards the plasma edge. This concentration towards the edge is in agreement with the fact that the value of b^r_{res} for $n = 4$ and $n = 6$ RMPs is higher in the plasma edge but lower in the core than for $n = 3$ RMPs, hence rotation braking in the core is expected to be lower than for $n = 3$. The broader spectrum means that any effects of applying RMPs are expected to be less sensitive to the value of the safety factor q than with $n = 3$ RMPs.

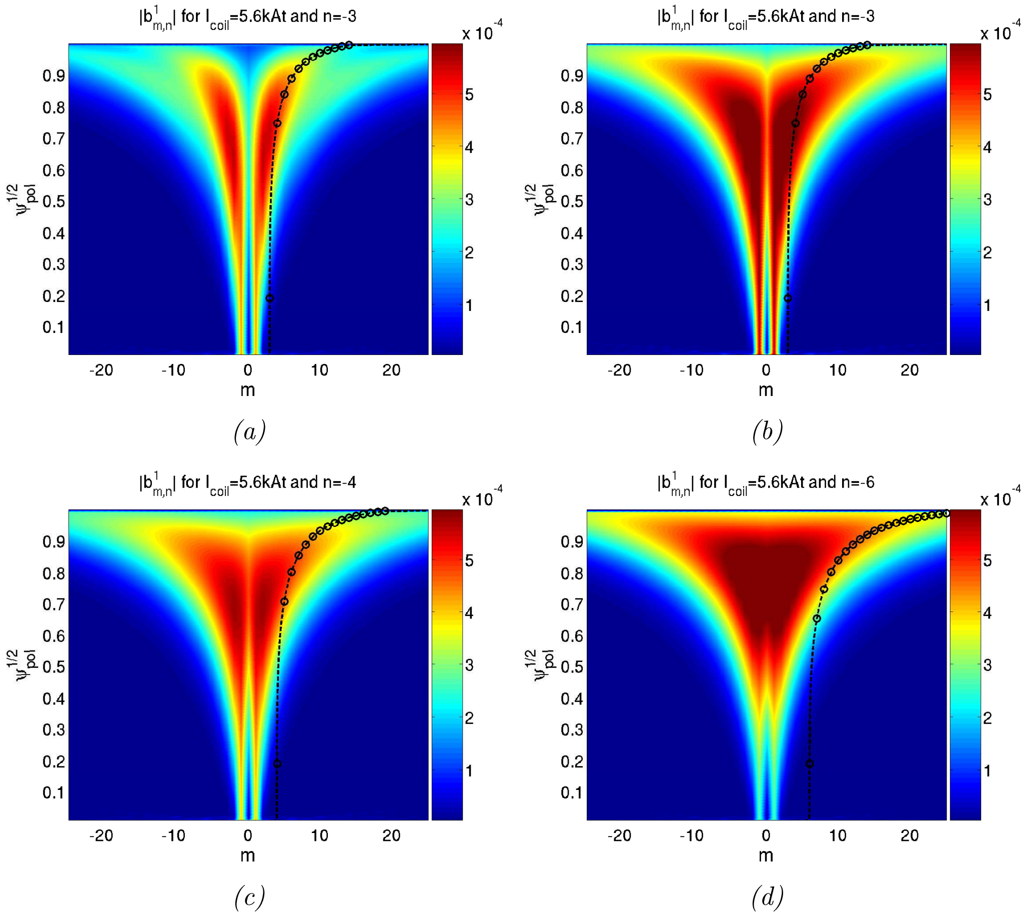

(a) *(b)* *(c)* *(d)*

Figure 5.4 Spectrum plots for (a) $n = 3$ (odd) coil configuration using six upper and six lower coils, and for (b) $n = 3$, (c) $n = 4$ and (d) $n = 6$ coil configurations, all using twelve lower coils only.

Lower single-null plasmas on MAST are subject to sawtooth-triggered ELMs, as can be seen in figure 5.5. Since RMPs have no effect on sawteeth, it seems doubtful that complete ELM suppression using RMPs will be possible with these plasmas. However, this does not preclude the possibility of ELM mitigation through the triggering of smaller, more frequent ELMs.

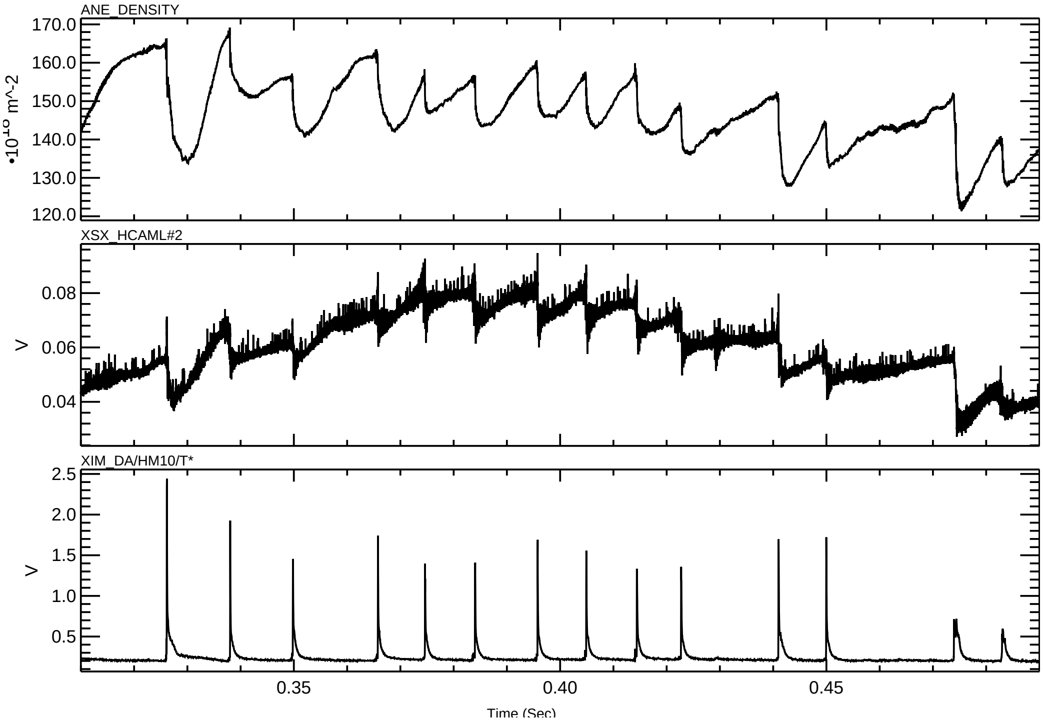

Figure 5.5 Sawteeth show up as sudden drops followed by gradual rises in the core soft X-ray data (middle). Each drop in the soft X-ray data corresponds to a loss of plasma from the core, which results in a similar drop in line-integrated density (top). In lower single-null plasmas on MAST, sawteeth trigger ELMs, which can be observed in the D_α data (bottom).

5.2 Effect of $n = 4$ RMPs

The $n = 4$ experiments were carried out with heating from two neutral beams. As with $n = 3$ RMPs, the application of $n = 4$ RMPs was observed to produce smaller, more frequent ELMs accompanied by density pump-out. This is shown in figure 5.6. In fact, this inverse relationship between the ELM frequency and the ELM energy loss is consistent across a range of plasmas and coil configurations for both natural and mitigated ELMs, as can be seen in figure 5.7 (*a*). It was found that there was a threshold ELM coil current for ELM mitigation or density pump-out to occur. Figure 5.7 (*b*) shows that above this threshold value, the ELM frequency increases with increasing ELM coil current.

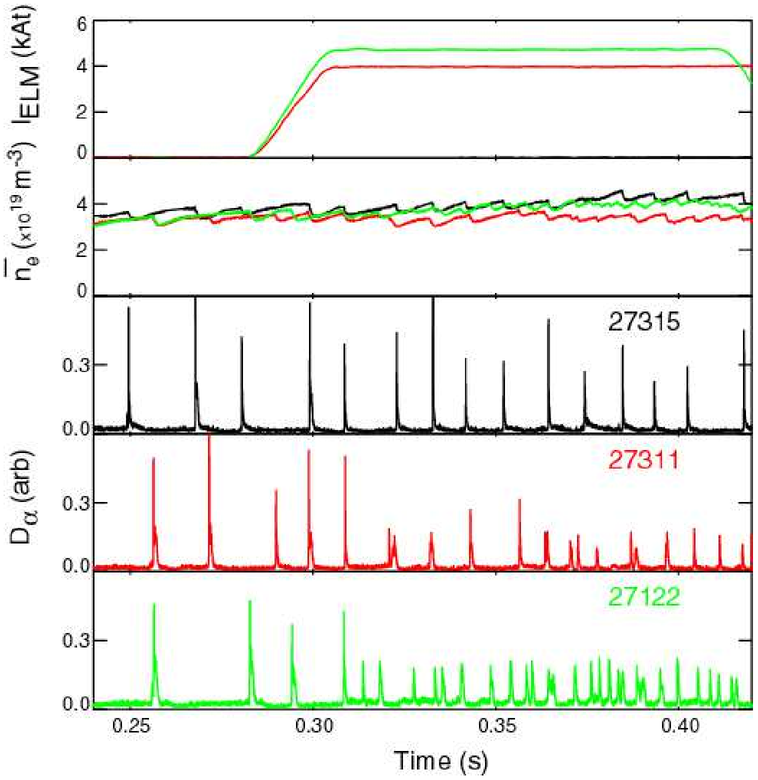

Figure 5.6 The application of $n = 4$ RMPs produced by the ELM coils (top) produces smaller, more frequent ELMs (27311 and 27122) compared to a reference shot (27315). This is accompanied by density pump-out (second from top).

Figure 5.8 shows the rotation braking to be almost as strong as for $n = 3$ RMPs, with the toroidal velocity similarly falling almost to zero across the whole plasma. However, the rotation braking does not cause a back-transition to L-mode as readily as for $n = 3$ RMPs, and there is a comfortable operational window in which ELM mitigation can be achieved without risk of a back-transition.

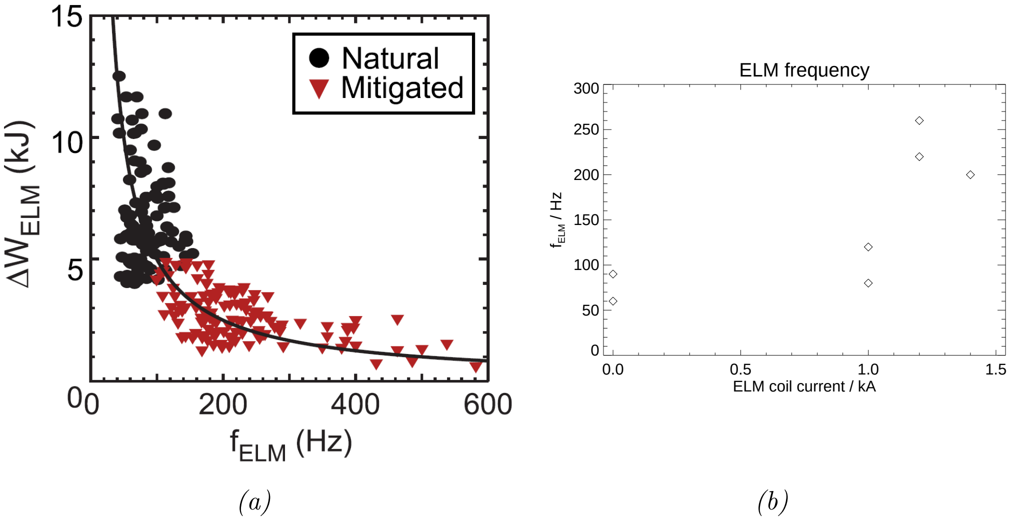

(a) *(b)*

Figure 5.7 (*a*) ELM energy loss ΔW_{ELM} as a function of ELM frequency f_{ELM} for both natural (circles) and mitigated (triangles) ELMs. ΔW_{ELM} was obtained from EFIT. From [65]. (*b*) ELM frequency increases with ELM coil current above a certain threshold.

Attempts were made to use gas puffing to refuel plasmas in which ELM mitigation and density pump-out had begun to occur. As can be seen in figure 5.9, it was found that refuelling could cause the density to recover without having an adverse effect on ELM mitigation. This shows that ELM mitigation is not simply a change in ELM type brought about by a change in the density.

A q-scan was carried out by varying the toroidal magnetic field B_ϕ in plasmas to which RMPs were applied. As shown in figure 5.10, the smallest, most frequent ELMs and the largest density pump-out were found to occur when B_ϕ was lowered to 0.52 T. The dependence of the ELM frequency on the value of B_ϕ is shown in figure 5.11 (*a*). Further reducing B_ϕ to 0.48 T was found to cause a back-transition to L-mode. Attempts were made to produce an effect on the plasma at $B_\phi = 0.48$ T while avoiding this back-transition by reducing the ELM coil current. However, no operational window was found between causing a back-transition and not having an effect on the plasma.

Since the width of the laminar region as calculated using ERGOS was found

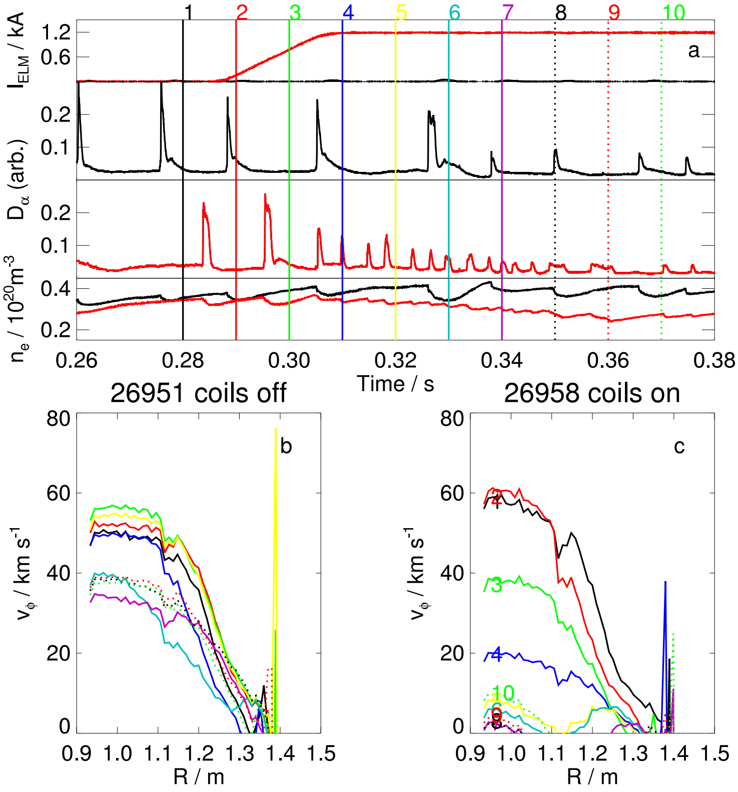

Figure 5.8 (*a*) Timing of the rotation measurements in relation to the application of the ELM coils and the effect on the ELMs. (*b*) Rotation profiles without and (*c*) with $n = 4$ RMPs, showing fairly strong rotation braking.

to be correlated with density pump-out in section 4.2, the width of the laminar region was calculated for different values of B_ϕ, and the results are shown in figure 5.11 (*b*). It can be seen that the widest laminar region was found to occur for $B_\phi = 0.56\,\mathrm{T}$, so in this case, the largest effect on the plasma does not correspond to the widest laminar region.

Figure 5.12 shows two discharges with 1 kA, $n = 4$ RMPs applied to plasmas with different values of B_ϕ. The first shot has $B_\phi = 0.55\,\mathrm{T}$ and both ELM mitigation and density pump-out occur, whereas the other shot has $B_\phi = 0.585\,\mathrm{T}$ and there is no effect on the ELMs or on the density. However, it can be seen that both plasmas undergo similar rotation braking. Therefore, the amount of rotation braking is not directly correlated with the occurrence

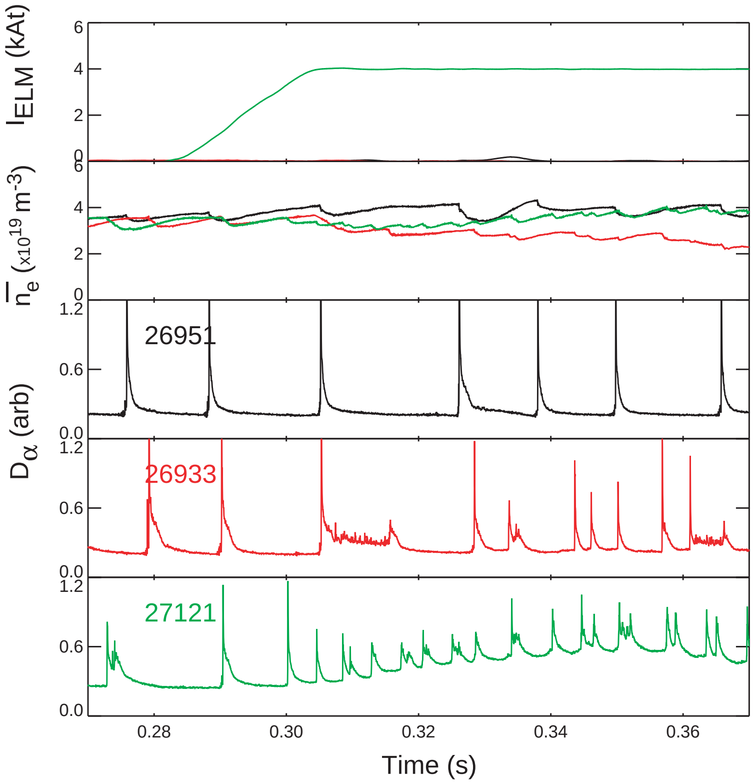

Figure 5.9 Without refuelling, the application of RMPs produced by the ELM coils (top) produces smaller, more frequent ELMs (26933) accompanied by density pump-out (second from top). When gas puffing is used to refuel the plasma, the smaller, more frequent ELMs are retained (27121), but the density recovers almost to the same level as without RMPs (26951).

of ELM mitigation or density pump-out. Furthermore, similar effects on both the ELM frequency and the density have been observed in double-null discharges but without any effect on the rotation. Finally, in the single-null discharges with heating from two neutral beams, i.e. the discharges for which the edge rotation data is not too noisy, it can be seen that even when considerable rotation braking occurs in the core, there is no significant effect on the edge rotation. The ELM frequency is expected to depend on conditions in the plasma edge. Therefore, since the rotation in the plasma edge does not change significantly, any change in ELM frequency is not simply due to a change in rotation [66].

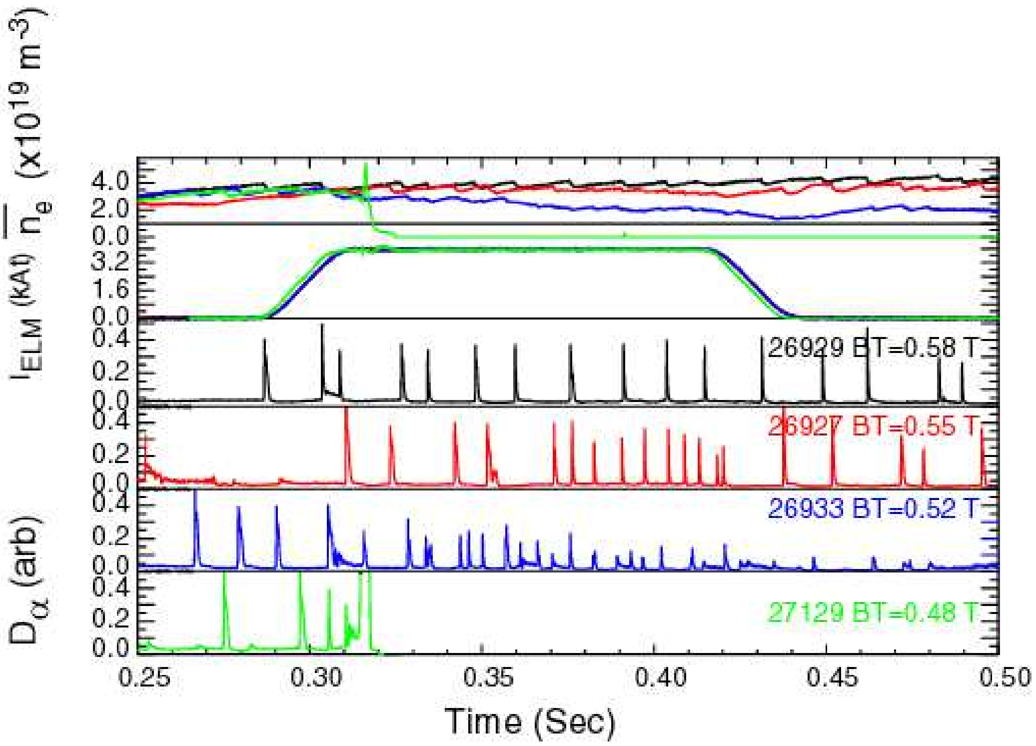

Figure 5.10 The application of RMPs to plasmas with different q-profiles causes varying levels of ELM mitigation and density pump-out. The largest effect occurs when $B_\phi = 0.52\,\mathrm{T}$.

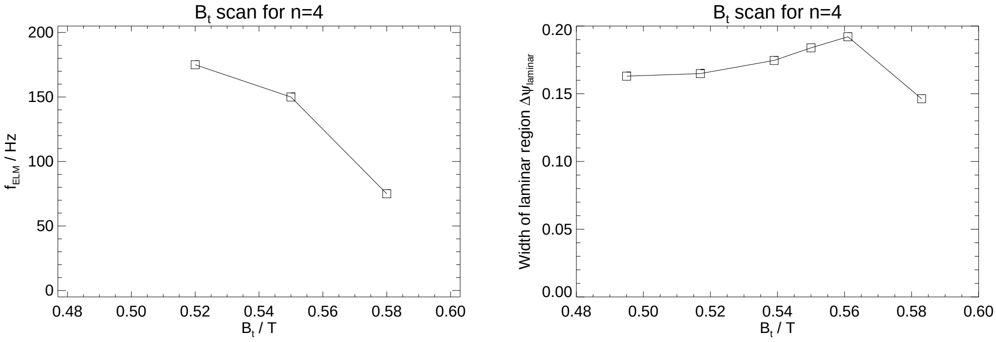

(a) *(b)*

Figure 5.11 (a) ELM frequency f_{ELM} and (b) width of the laminar region as a function of B_ϕ. The widest laminar region occurs for $B_\phi = 0.56\,\mathrm{T}$, whereas the ELM frequency is greatest for $B_\phi = 0.52\,\mathrm{T}$.

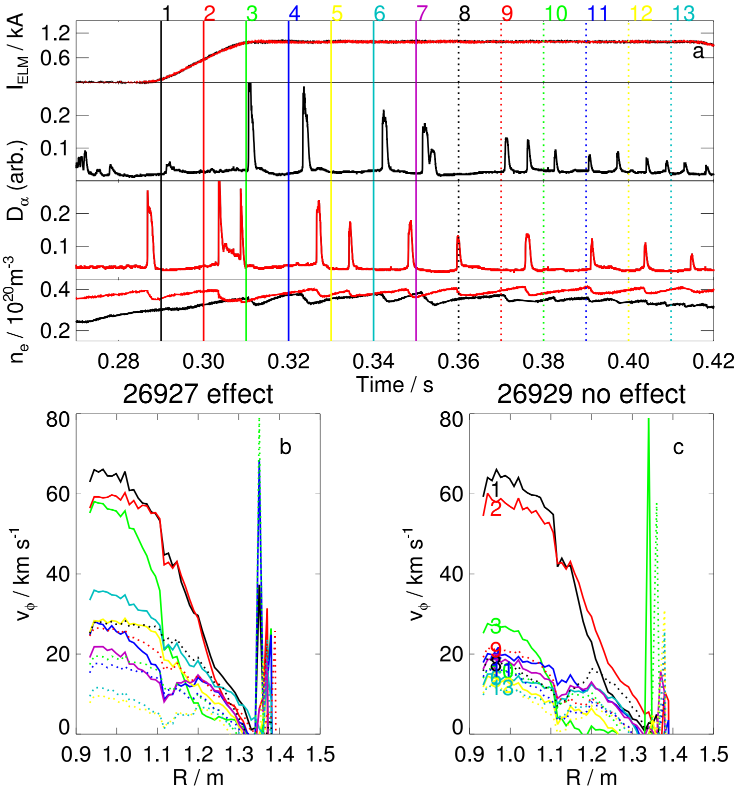

Figure 5.12 (a) Timing of the rotation measurements in relation to the application of the ELM coils and the effect on the ELMs. (b) Rotation profiles for a discharge displaying both ELM mitigation and density pump-out and (c) for a discharge displaying neither ELM mitigation nor density pump-out, showing a similar amount of rotation braking.

5.3 Effect of $n = 6$ RMPs

5.3.1 Experiments with one neutral beam

The first $n = 6$ lower single-null ELM mitigation experiments were carried out with heating from only one neutral beam. Again, the application of RMPs was observed to produce smaller, more frequent ELMs accompanied by density pump-out. This is shown in figure 5.13. It was found that there was a threshold ELM coil current between ~ 0.7 and $\sim 1.0\,\mathrm{kA}$ for ELM mitigation or density pump-out to occur. Figure 5.14 shows that above this threshold value, the ELM frequency and the amount of density pump-out both increase approximately linearly with ELM coil current.

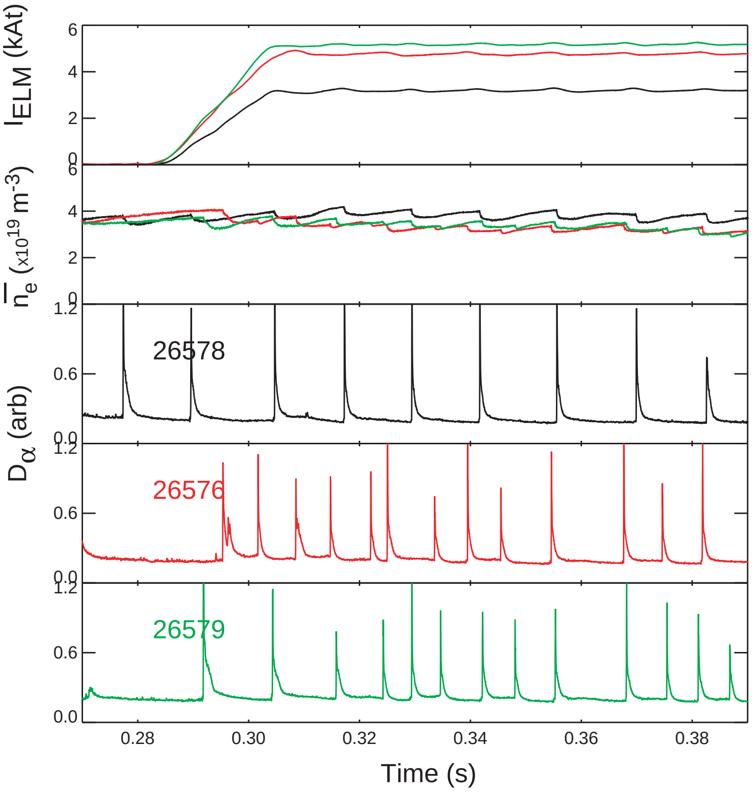

Figure 5.13 The application of $n = 6$ RMPs produced by the ELM coils (top) produces smaller, more frequent ELMs (lower three panes) accompanied by density pump-out (second from top).

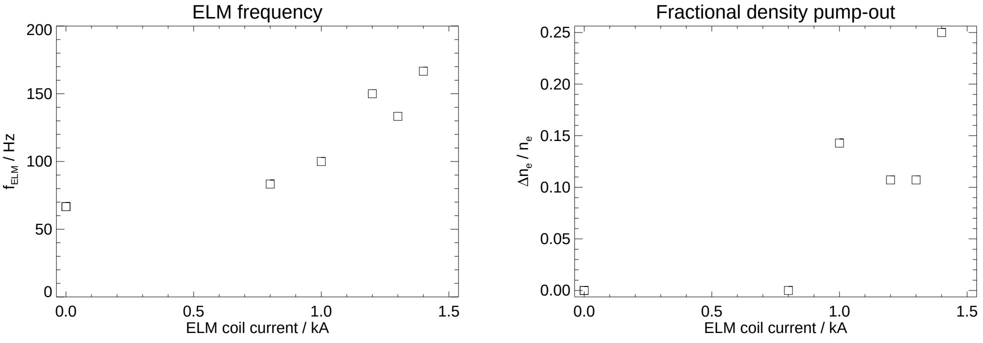

(a) *(b)*

Figure 5.14 (a) ELM frequency and (b) amount of density pump-out both increase roughly linearly with ELM coil current above a certain threshold.

The rotation braking is less severe than for $n = 3$ or $n = 4$ RMPs – it can be seen from figure 5.15 that the toroidal velocity decreases to $\sim 20\,\mathrm{km\,s^{-1}}$ rather than almost zero – and so ELM mitigation can be achieved while avoiding a back-transition to L-mode.

5.3.2 Experiments with two neutral beams

Later $n = 6$ lower single-null ELM mitigation experiments were carried out with heating from two neutral beams. Once again, the application of RMPs was observed to produce smaller, more frequent ELMs accompanied by density pump-out, as can be seen in figure 5.16. It was again found that there was a threshold ELM coil current for ELM mitigation or density pump-out to occur. Figure 5.17 compares the dependence of the ELM frequency on the ELM coil current for one-beam and two-beam plasmas.

The one-beam plasmas have $\beta_{\mathrm{N}} \approx 2.3$ while the two-beam plasmas have $\beta_{\mathrm{N}} \approx 3.3$, so comparing one- and two-beam plasmas is effectively carrying out a β_{N}-scan. It appears as though the threshold for an increase in ELM frequency with increasing ELM coil current may possibly be higher for two-beam plasmas. However, for the maximum ELM coil current of 1.4 kA, the

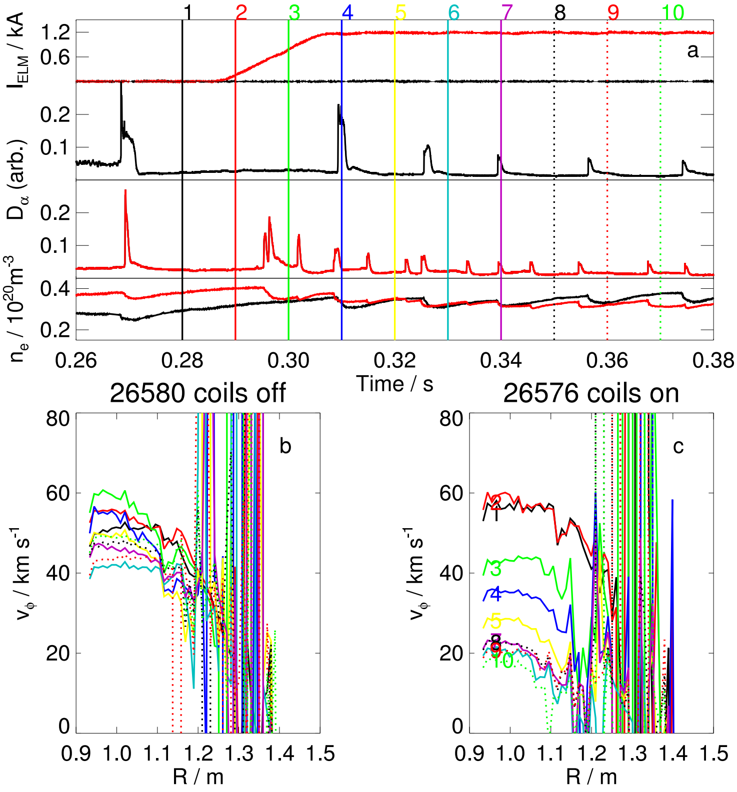

Figure 5.15 (a) Timing of the rotation measurements in relation to the application of the ELM coils and the effect on the ELMs. (b) Rotation profiles without and (c) with $n = 6$ RMPs, showing less severe rotation braking than for $n = 3$ or $n = 4$ RMPs.

ELM frequency is similar to that for one-beam plasmas. The large spread of the data, combined with the limited number of data points, means that the level of confidence in these conclusions is quite low.

The rotation braking for two-beam plasmas with $n = 6$ RMPs is similar to that for one-beam plasmas with $n = 6$ RMPs, as can be seen in figure 5.18, but the rotation measurements in the edge are better with two neutral beams. As with one neutral beam, the rotation braking is not severe enough to cause a back-transition to L-mode.

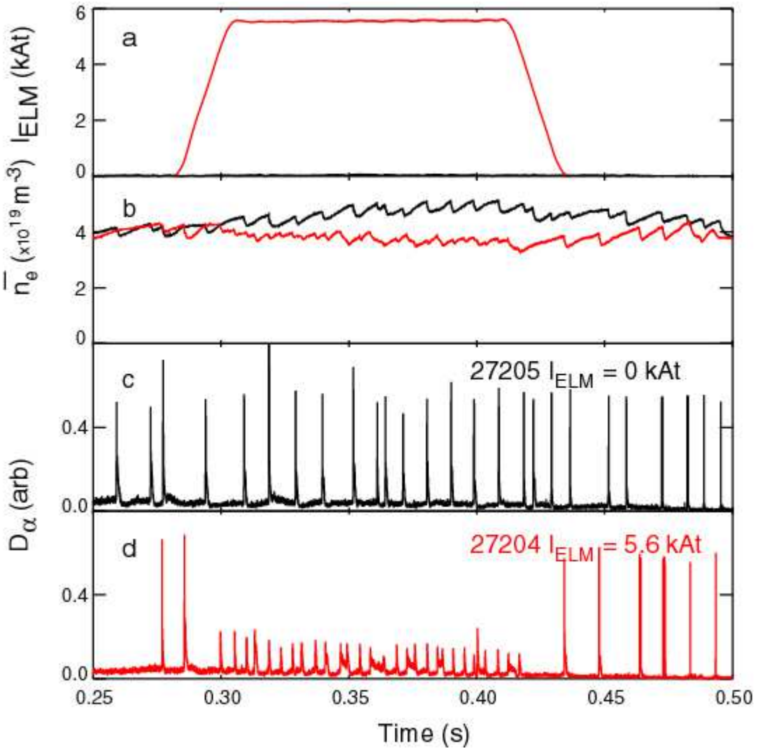

Figure 5.16 As with one neutral beam, the application of $n = 6$ RMPs produced by the ELM coils (a) produces smaller, more frequent ELMs (c and d) accompanied by density pump-out (b).

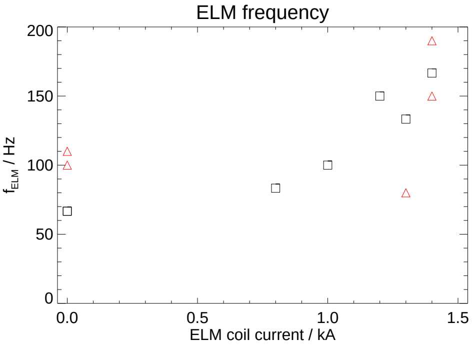

Figure 5.17 ELM frequency f_{ELM} versus ELM coil current. Squares represent discharges with one neutral beam; triangles represent those with two beams.

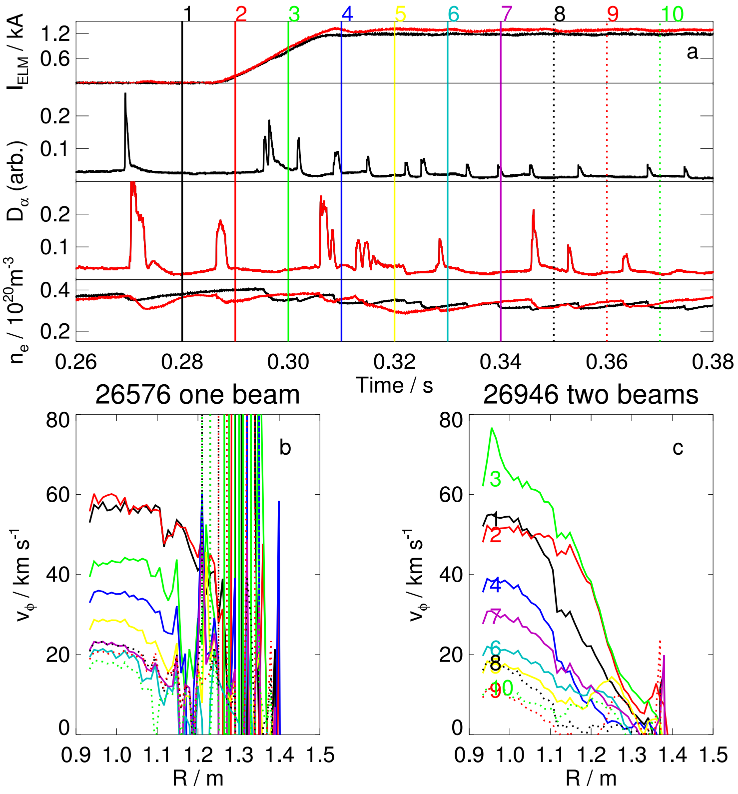

Figure 5.18 (a) Timing of the rotation measurements in relation to the application of the ELM coils and the effect on the ELMs. (b) Rotation profiles with $n = 6$ RMPs applied to a one-beam plasma and (c) to a two-beam plasma, showing a similar amount of rotation braking in each case.

5.4 Comparison of $n = 4$ and $n = 6$ RMPs

Figure 5.19 (a) shows a plot of ELM frequency versus ELM coil current for discharges with $n = 4$ and $n = 6$ RMPs. In the case of $n = 6$ RMPs, both one- and two-beam discharges are shown. In all cases, ELM frequency increases with ELM coil current above a certain threshold value. The spread of the points is quite large. This makes it difficult to say whether or not this threshold value depends on the number of neutral beams or the dominant toroidal mode number of the magnetic perturbation, or whether or not the increase in ELM frequency with ELM coil current is linear, except in the case of one-beam discharges with $n = 6$ RMPs, where there does appear to be a linear increase.

Figure 5.19 (b) shows a plot of the ratio of the toroidal velocity v_1 as the ELM coil current ramps up to the velocity v_2 20 ms later, which is used as a measure of rotation braking, for the same discharges as shown in figure 5.19 (a). The velocity values were taken at the radial location on the LFS where $q = 1$. This location was chosen partly because the rotation measurements for greater values of R in plasmas with only one beam are very noisy, and partly because the local minimum in the rotation profile at this location shows that resonant braking occurs on the $q = 1$ surface. Rotation braking also increases with ELM coil current above a certain threshold value. The spread of the points is again quite large, but it is clear that the greatest rotation braking occurs for $n = 4$ RMPs. As with ELM frequency, the one-beam discharges with $n = 6$ RMPs show the most convincing linear increase with ELM coil current.

In order to test whether the increase in ELM frequency shown in figure 5.19 (a) is really due to a direct correlation with ELM coil current or whether ELM frequency simply increases with decreasing toroidal rotation, ELM frequency was plotted against toroidal velocity for the discharges in figure 5.19 without applied RMPs, and the results are shown in figure 5.20. Plotting this data for discharges with applied RMPs would not be meaningful since the plasmas on which the RMPs have a greater effect would have both higher ELM frequencies and lower toroidal rotation, making it appear that ELM frequency increases with decreasing rotation whether or not that is in fact the case. Figure 5.20 shows that for discharges with two neutral beams, ELM frequency actually increases slightly with increasing toroidal velocity, showing that any increase in ELM frequency cannot have been caused by a decrease in toroidal rotation. More data points would be required to see whether this small increase is significant or whether there is in fact no correlation. For the one-beam discharges, the data points are too close together to draw any conclusion about the relationship between ELM frequency and toroidal rotation.

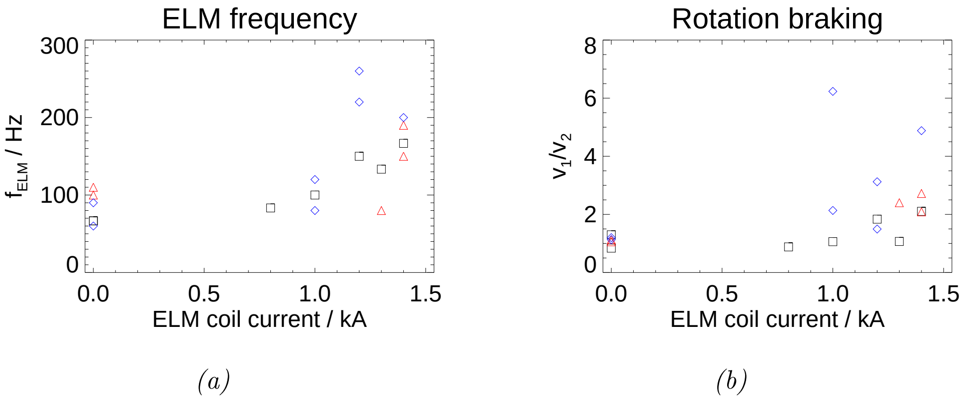

(a)

(b)

Figure 5.19 (a) ELM frequency f_{ELM} and (b) v_1/v_2 versus ELM coil current. Diamonds represent discharges with $n = 4$ RMPs; squares represent those with $n = 6$ RMPs and one neutral beam; triangles represent those with $n = 6$ RMPs and two beams.

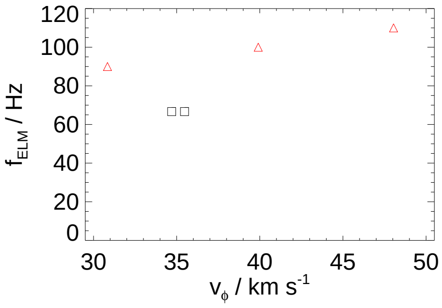

Figure 5.20 ELM frequency f_{ELM} versus toroidal velocity v_ϕ for plasmas without applied RMPs. Squares represent discharges with one neutral beam; triangles represent those with two beams.

Chapter 6

Effect of a locked mode on the magnetic field

6.1 Locked modes

Toroidal rotation in tokamaks tends to screen out the effect of any external deviations from axisymmetry such as the vessel wall or error fields, since any interaction between a particular 'packet' of plasma and a source of non-axisymmetry will be averaged out over each toroidal rotation that this packet completes.

However, the effect of these non-axisymmetries may be only partially screened, in which case an interaction between plasma instabilities and sources of non-axisymmetry may occur. Such an interaction could cause the toroidal rotation of the instability to slow down, which in turn would cause rotation braking across the whole plasma. The resulting lack of toroidal rotation could lead to the penetration of error fields or the growth of slowly rotating modes that then become stationary. Such modes are said to have 'locked' and are known as locked modes. Locked modes are generally detrimental and often result in termination of the plasma discharge [67].

A saddle coil is a single-turn coil used as a magnetic diagnostic. The name is derived from the shape of the coil. A changing magnetic flux through the loop of the coil causes a current to flow. The value of this current is directly proportional to the rate of change of magnetic flux through the loop. Therefore, by integrating the current signal over time, the value of the magnetic flux can be obtained. Dividing this by the area of the loop provides the (spatial) average value of the component of the magnetic field vector through each saddle coil perpendicular to the plane in which the loop sits. Due to the orientation of the saddle coils on MAST, this is the radial component.

MAST is equipped with a set of twelve midplane saddle coils that are evenly spaced in the toroidal direction. However, the coil in sector 9 is faulty, leaving a total of eleven functioning midplane coils. Figure 6.1 shows the typical behaviour of a plasma discharge during a locked mode. At the onset of the mode, the growth of a magnetic perturbation can be seen in the saddle coil signal, in this case corresponding to an $n = 1$ mode. This is accompanied by the loss of plasma density, an increase in divertor D_α emission and the elimination of sawteeth [67].

A 400 kA connected double-null MAST L-mode discharge displays a number of interesting features: divertor strike-point splitting, multiple peaks in the HFS temperature profile, flux tubes in the scrape-off layer (the region outside the LCFS) and a signal in the saddle coil data indicative of an $n = 1$ locked mode, as can be seen in figures 6.2 and 6.3. It is possible that this locked mode produces these features by modifying the magnetic field structure. To test this hypothesis, a locked mode was modelled as a current sheet on a rational surface and the effect of this current sheet on the magnetic field structure was calculated.

The divertor strike-point splitting was observed using infra-red (IR) measurements from the divertor, the temperature profile was measured using Thomson scattering, and the flux tubes in the scrape-off layer were observed using a camera with the divertor leg in its field of view. Figure 6.4 shows the location of the infra-red divertor measurements, the Thomson scattering

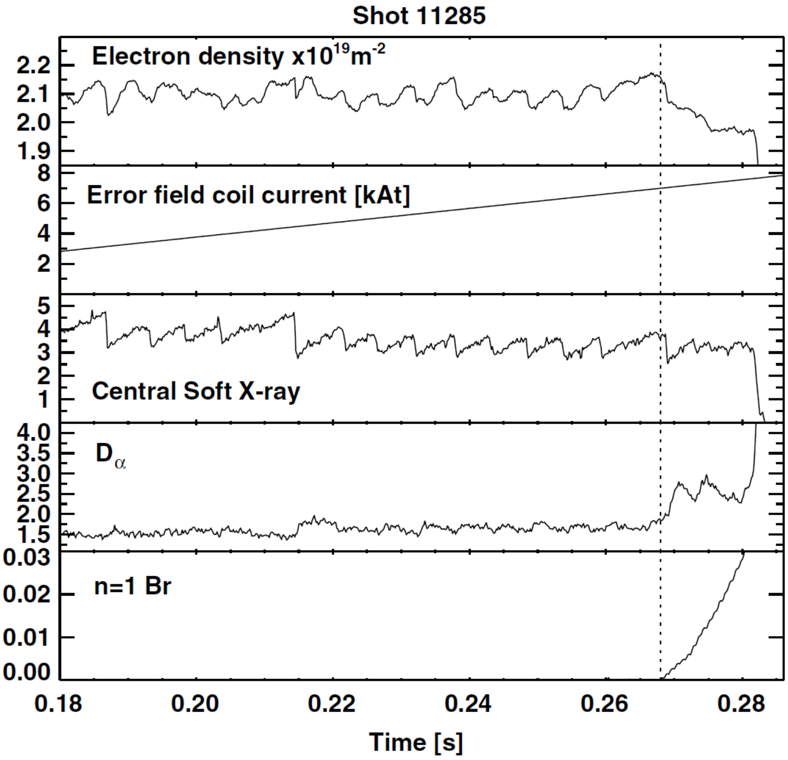

Figure 6.1 Example of a typical locked mode. From [67].

system and the camera used to image the divertor leg. It also illustrates the difference in the definition of the toroidal angle in ERGOS (anti-clockwise from East) and the conventional definition of the toroidal angle on MAST (clockwise from North).

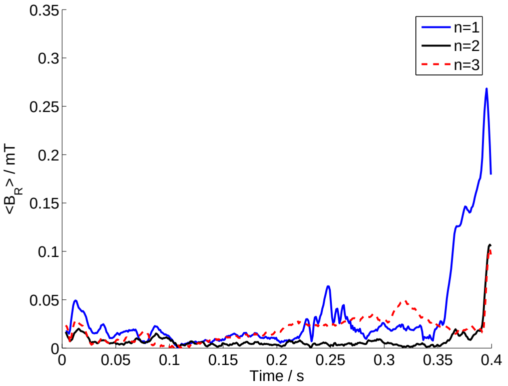

Figure 6.2 The saddle coil data show that an $n = 1$ mode grows from $\sim$ 350 ms followed by a sharp peak in the signals for all mode numbers around 395 ms.

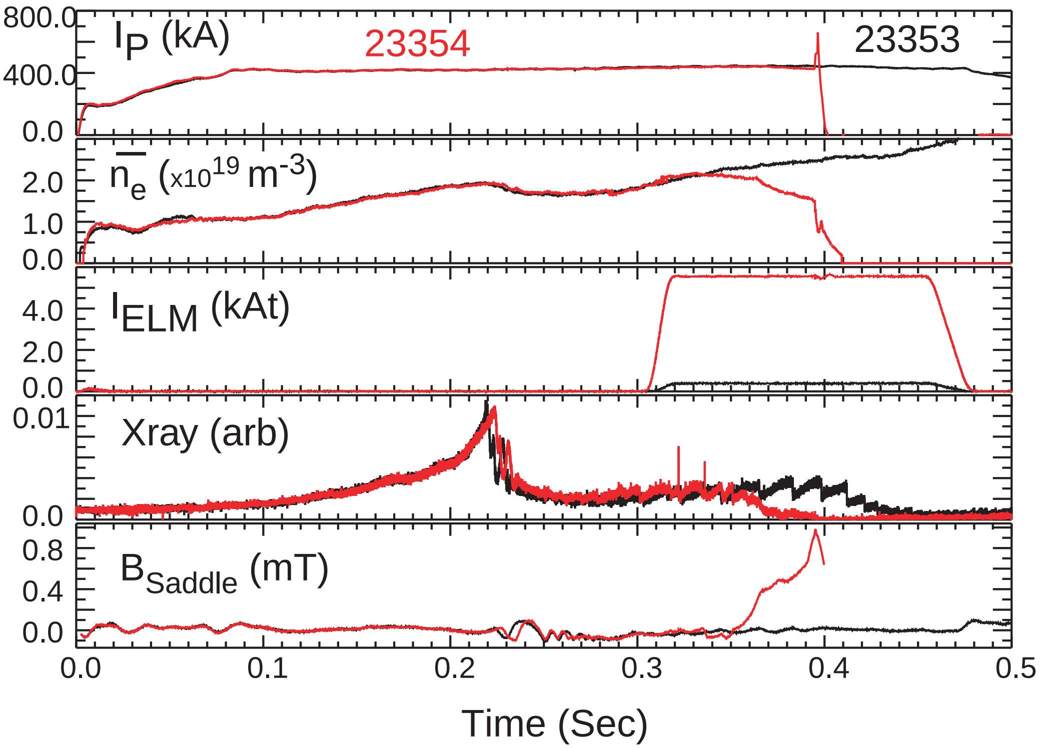

Figure 6.3 The application of RMPs triggers a mode that can be seen in the saddle coil data from $\sim$ 350 ms. This is accompanied by the elimination of sawteeth from the soft X-ray data and is followed by density pump-out from $\sim$ 365 ms and a disruption around 395–400 ms, as can be seen by the complete loss of plasma current.

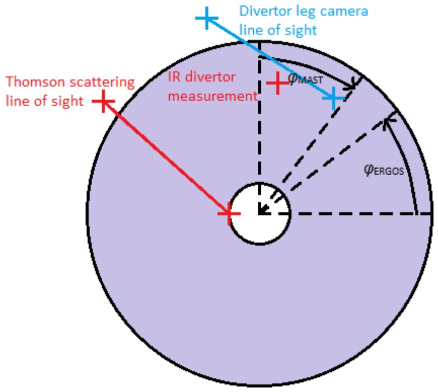

Figure 6.4 Plan view of a MAST plasma showing the location of the infrared divertor measurements, the Thomson scattering system and the camera used to image the divertor leg, and illustrating the different conventions regarding the toroidal angle.

6.2 Current sheet on a rational surface

6.2.1 Modelling the current sheet

Since the particles in a plasma are free to move along magnetic field lines but confined to gyrate about them, current flows more easily along field lines than perpendicular to them. On a rational surface, current flowing along a field line will join up on itself. Current can flow in one direction along some field lines and in the opposite direction along others. This would not be possible on an irrational surface since a single field line traces out a whole flux surface.

A current sheet parallel to the magnetic field on a rational surface can have poloidal and toroidal mode numbers m and n respectively, given by $m = qn$, where q is the safety factor on the flux surface. Such a current sheet will produce a perturbation to the magnetic field that will also have poloidal and toroidal mode numbers m and n respectively.

The amplitude, phase and toroidal mode number of the current sheet can be varied and the corresponding saddle coil signal calculated, which can be compared with the experimentally measured signal. The amplitude, phase and toroidal mode number of the current sheet can then be adjusted such that the simulated and experimental saddle coil signals match. The perturbation to the magnetic field that this current sheet produces can be calculated and the effect that this has on the magnetic field structure can be modelled using ERGOS.

6.2.2 Field produced by the current sheet

The current sheet is characterized by the surface current density $\boldsymbol{J}_S$, which is defined such that the current I crossing a curve C on some surface is given by

$$I = \int_C |\boldsymbol{J}_S \times d\boldsymbol{l}| \,, \tag{6.1}$$

where $\boldsymbol{dl}$ is a vector along the curve C.

This surface current density is constrained by the assumptions that $\boldsymbol{J}_S$ is parallel to the equilibrium magnetic field, that $\boldsymbol{\nabla} \cdot \boldsymbol{J} = 0$ (where $\boldsymbol{J}$ is the current density rather than the surface current density, i.e. not $\boldsymbol{\nabla} \cdot \boldsymbol{J}_S = 0$) and that $\boldsymbol{J}_S$ varies with poloidal and toroidal mode numbers m and n respectively, i.e. $|\boldsymbol{J}_S| \propto \exp[\mathrm{i}(m\theta^* + n\phi)]$, where ϕ is the toroidal angle and θ^* is the field-aligned poloidal angle.

The locked mode was modelled as an $m = 2$, $n = 1$ current sheet on the $q = 2$ surface. Figure 6.5 (a) shows how $\boldsymbol{J}_S$ varies across this surface. Since $\boldsymbol{J}_S$ represents an infintesimally thin surface current density, it is difficult to compare its magnitude with that of the equilibrium plasma current density in order to assess how large this perturbation is. Of course, in reality, a current sheet could not be infintesimally thin and might be expected to have approximately the same width as the magnetic islands on that flux surface. For comparison with the plasma current density, a current density $\boldsymbol{J}$ can be estimated by assuming a finite width for the current sheet and dividing $\boldsymbol{J}_S$ by this width. Figure 6.5 (b) shows a plot of this estimate for $\boldsymbol{J}$ assuming a current sheet width of 5 cm. It can be seen that the maximum value of $\boldsymbol{J}$ is of the order of $1\,\mathrm{MA\,m^{-2}}$. This is comparable with the plasma current density, showing that this current sheet indeed represents a very large perturbation to the equilibrium plasma current density. A comparison with the plasma current I_P is impossible since integrating $\boldsymbol{J}_S$ over the $q = 2$ surface to obtain a current yields a value of zero.

The perturbed magnetic field $\boldsymbol{B}_1$ produced by the current sheet was calculated using the Biot–Savart law:

$$\boldsymbol{B}_1 = \oint_S \frac{\mu_0}{4\pi} \frac{\boldsymbol{J}_S \times \boldsymbol{r}}{r^3} dS, \tag{6.2}$$

where S is the $q = 2$ surface, $\boldsymbol{r}$ is the distance from the surface element dS to the point where the value of $\boldsymbol{B}_1$ is to be calculated, and r is the magnitude of $\boldsymbol{r}$. $\boldsymbol{B}_1$ was then added to the equilibrium magnetic field $\boldsymbol{B}_0$. Figure 6.6 shows Poincaré plots of the resulting magnetic field. It can be seen that many

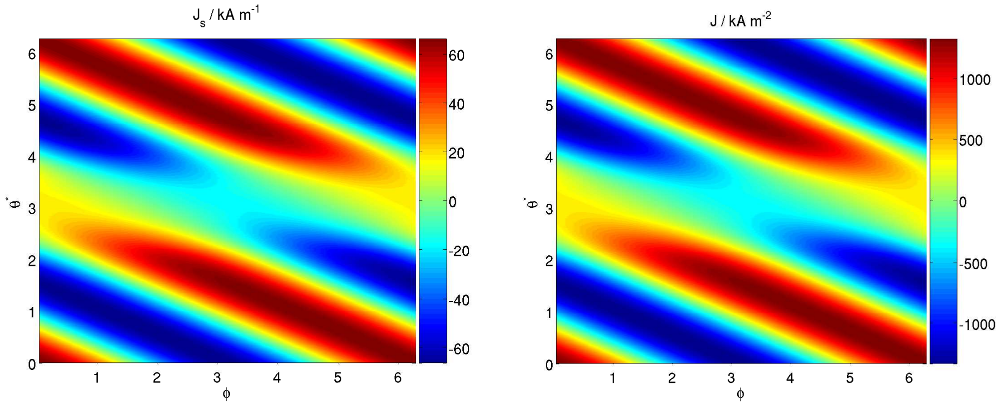

(a) (b)

Figure 6.5 (*a*) Surface current density $\boldsymbol{J}_S$ and (*b*) the corresponding current density $\boldsymbol{J}$ assuming a current sheet width of 5 cm as functions of toroidal and poloidal angles ϕ and θ^* respectively.

flux surfaces are distorted or destroyed throughout much of the plasma and that there is a very large magnetic island on the $q = 1$ surface, which at this toroidal angle appears in the shape of a crescent in (R, Z) co-ordinates.

The current sheet on the $q = 2$ surface would be expected to produce magnetic islands on this surface, but these islands are not visible in figure 6.6. This is because the perturbation is so strong that the islands are destroyed. In figure 6.7, the strength of the perturbation is reduced by a factor of 10 and the islands on the $q = 2$ surface are clearly visible.

Figure 6.8 shows a corresponding plot of the field line connection length near the upper X-point. A number of white areas are visible in the plasma edge. These white areas consist of field lines with very short connection length ($L_\mathrm{c} \approx 50\,\mathrm{m}$). The lobes in divertor connection length plots such as figure 6.14 (*a*) show corresponding boomerang-shaped regions of field lines with short connection length ($L_\mathrm{c} \approx 50\,\mathrm{m}$) through the plasma to the other divertor [59]. These field lines are not to be confused with the even shorter field lines outside of the lobes ($L_\mathrm{c} \lesssim 30\,\mathrm{m}$) that do not enter the plasma on their way from one divertor to the other and are not relevant to this discussion. The white areas of figure 6.8 show where field lines from the

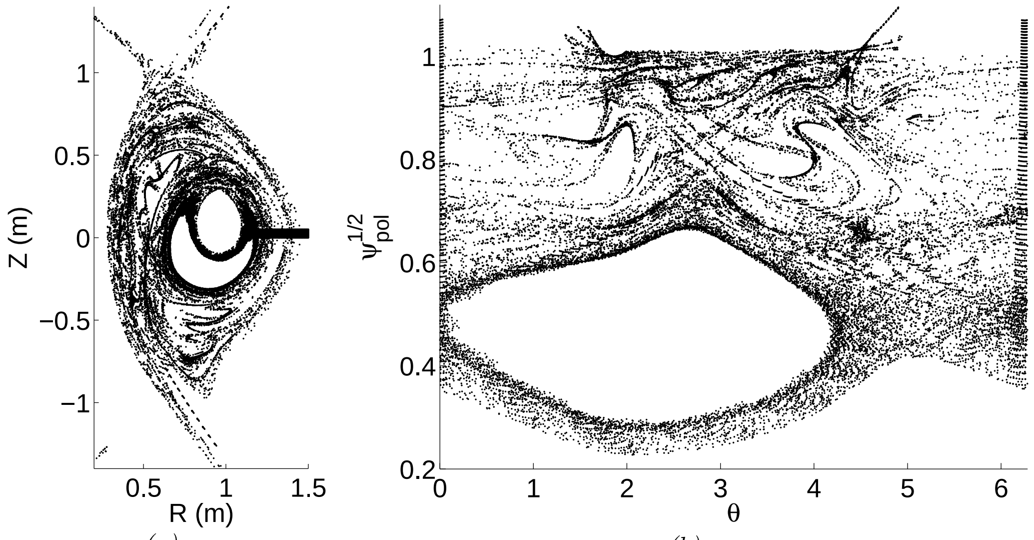

(a) *(b)*

Figure 6.6 Poincaré plots of the plasma containing the current sheet in (*a*) (R, Z) co-ordinates and (*b*) $(\Psi_{\rm N}^{1/2}, \theta)$ co-ordinates. Note that this is the geometrical angle θ rather than the field-aligned angle θ^*. Flux tubes are visible in the upper and lower divertor legs. In (*a*), the large crescent shape is a magnetic island on the $q = 1$ surface, the black rectangle on the LFS midplane is where the field lines are started, and the large circle in the core is a result of not starting any field lines this close to the core.

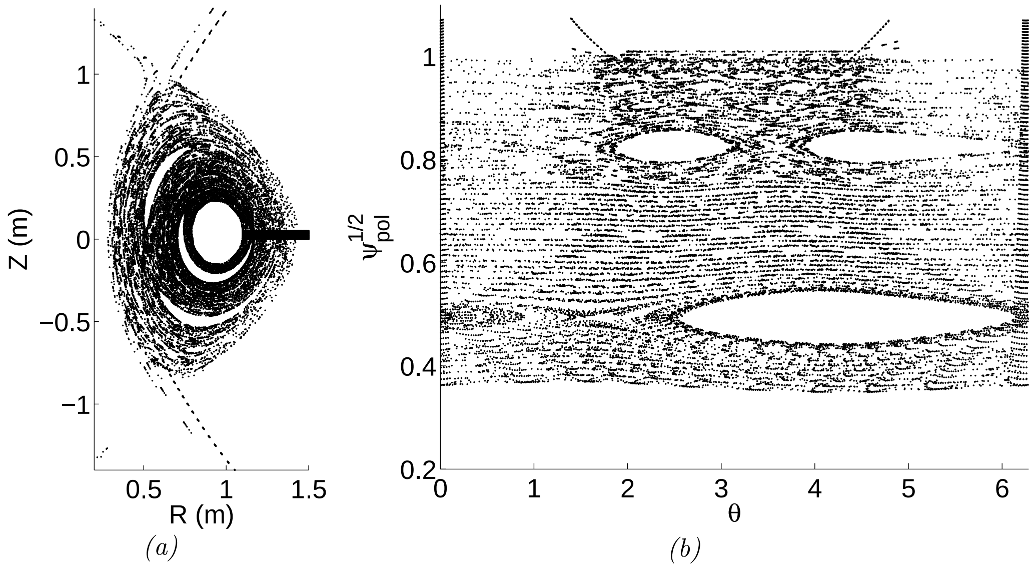

(a) *(b)*

Figure 6.7 Poincaré plots with the current in the current sheet reduced by a factor of 10. The magnetic islands on the $q = 2$ surface are now visible and the island on the $q = 1$ surface is no longer so large.

boomerang-shaped regions of the lobes perforate the plasma as they travel to the other divertor along very short paths [68]. Each bundle of such field lines forms what is known as a laminar flux tube [69]. The field lines in these flux tubes can also be observed just outside the equilibrium divertor legs in figures 6.6 and 6.7 as they travel between the plasma and the divertor.

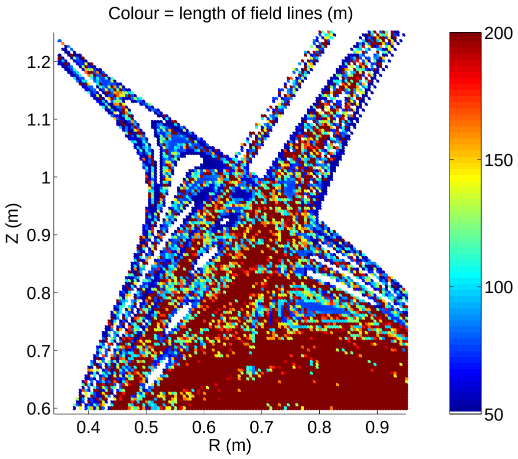

Figure 6.8 Connection length plot near the upper X-point. Flux tubes are visible as white areas in the plasma edge with very short connection length.

6.3 Saddle coil data

Figure 6.9 (a) shows the (spatial) average value of the radial component of the magnetic field vector $\langle B_R \rangle$ measured experimentally by the midplane saddle coil in each sector. There is no data from the saddle coil in sector 9 as it is faulty. An $n = 0$ offset has been subtracted from the data since it could not have been produced by the $n = 1$ locked mode. Figure 6.9 (b) shows the simulated saddle coil data from the current sheet. The amplitude and phase of the current sheet were adjusted to match the experimental data.

The strike-point splitting, the multiple peaks in the temperature profile and the flux tubes in the scrape-off layer were each observed at a particular toroidal angle. Since the effects of the locked mode on the magnetic field structure are non-axisymmetric, when looking at these modelled effects and comparing with the experimental data, it is important to look at the same toroidal angle as the experimental data were taken, or since the current sheet is the only source of non-axisymmetry in the model, at least at the same toroidal angle with respect to the locked mode.

In order for the field produced by the current sheet in the model to match

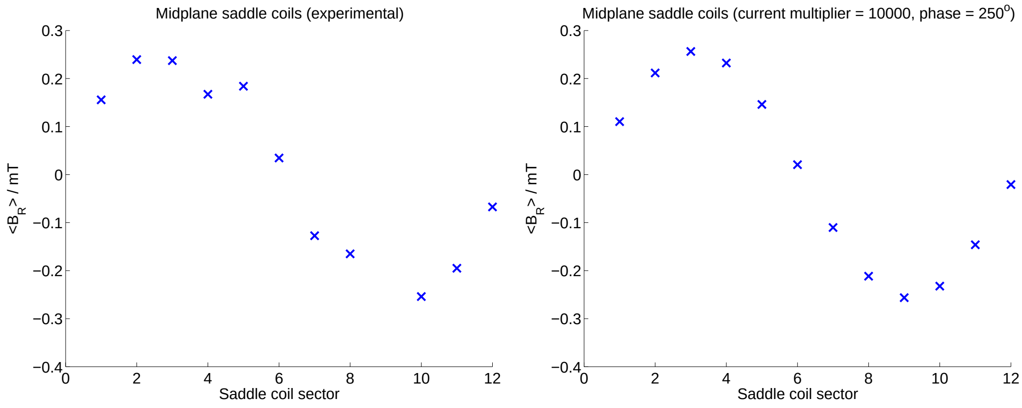

(a) *(b)*

Figure 6.9 (a) Experimental and (b) simulated saddle coil data. The amplitude and phase of the current sheet have been adjusted such that the simulated data match the experimental data.

that produced by the locked mode experimentally, it had to be rotated 250° in the clockwise direction. This is equivalent to rotating the angle at which we look for an effect on the magnetic field structure 250° in the anti-clockwise direction, which is more convenient in ERGOS and was therefore the method used here. For this reason, phrases such as "field lines started at 270°" and "Poincaré plot taken at 32.5°" actually refer to the equivalent angle with respect to the current sheet.

6.4 Connection length profile

Figure 6.10 shows HFS temperature profiles at 371 ms, 376 ms and 381 ms, i.e. from the onset of the locked mode, along with corresponding smoother, more typical temperature profiles from a reference shot for comparison. Multiple peaks and troughs in the profiles remain in the same location from each time point to the next, showing that they are not due to random fluctuations.

The toroidal angle at which the Thomson scattering measurements are taken varies with major radius from $\sim 305°$ on the LFS to $\sim 270°$ on the HFS. Figure 6.11 (a) shows a poloidal cross-section of the minimum connection length

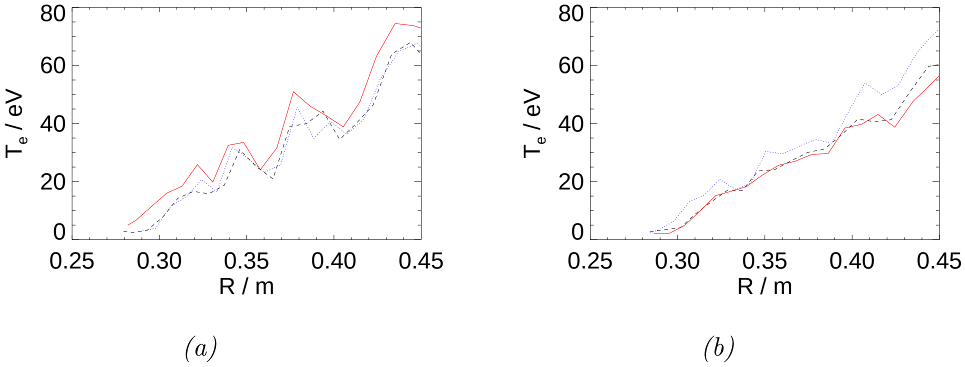

(a)

(b)

Figure 6.10 HFS temperature profiles at 371 ms (dashed line), 376 ms (solid line) and 381 ms (dotted line), showing (*a*) peaks and troughs that persist at the same locations for a period of over 10 ms and (*b*) smoother, more typical temperature profiles for a reference shot.

(i.e. the connection length in whichever is shorter out of the positive and negative toroidal directions at each point) of field lines started at 270° at the HFS midplane. The dashed line marks the height of the Thomson scattering measurements. It can be seen that there are regions of longer and shorter connection lengths. Parallel transport along the field lines from the comparatively cold divertor could be expected to cool the regions with shorter connection lengths, producing the dips seen in the temperature profiles in figure 6.10 (*a*). Figure 6.11 (*b*) was produced by averaging the connection length over the vertical direction in order to smooth out the very fine structure with large fluctuations. In the plasma, perpendicular transport would be expected to smooth out the effects of very fine magnetic structure in a similar way. The resulting connection length profile contains peaks and troughs qualitatively similar to those in figure 6.10.

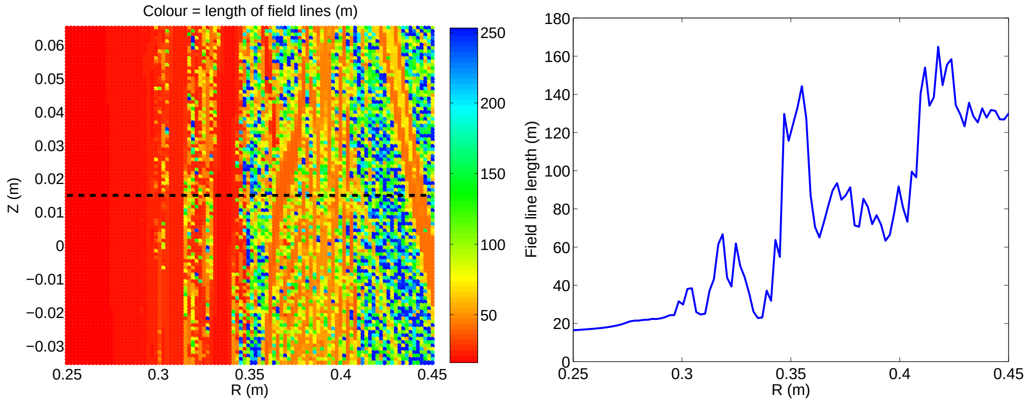

(*a*) (*b*)

Figure 6.11 (*a*) Poloidal cross-section of the minimum connection length, showing regions of longer and shorter connection length. (*b*) Averaging over the vertical direction produces a connection length profile similar to the temperature profiles in figure 6.10.

6.5 Strike-point splitting

The area where the plasma exhaust impacts upon the divertor is known as the strike-point. The plasma exhaust heats the divertor tiles, causing them to emit strongly in the infra-red region of the electromagnetic spectrum. Therefore, the strike-point can be seen in images taken using infra-red light, such as figure 6.12, which shows a clear splitting of the strike-point into two distinct lines.

Figure 6.13 (*a*) shows the temperature of the lower divertor calculated from infra-red measurements at a single toroidal angle as a function of major radius and time. It can be seen that the intensity of the emission suddenly increases around 370 ms – the time of the onset of the locked mode. From this time onwards, two clear peaks are observed, corresponding to strike-point splitting. The vertical band around 400 ms is caused by the plasma disruption. Figure 6.13 (*b*) shows the radial temperature proile 369 ms. The strike-point splitting can be clearly seen as two distinct peaks around 1.34 m and 1.39 m in the temperature profile.

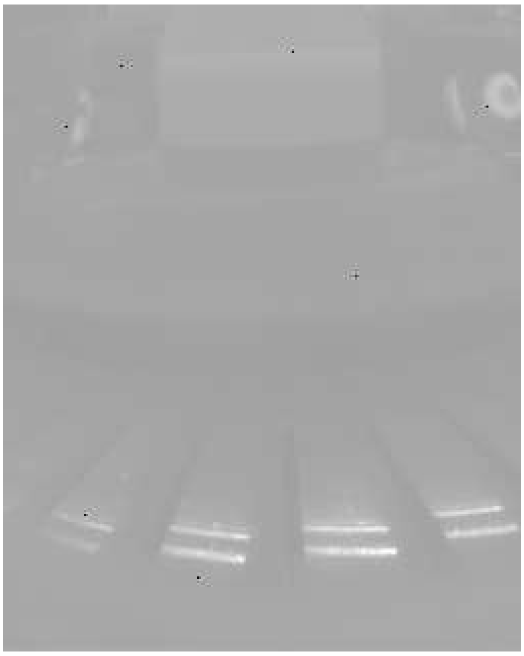

Figure 6.12 Infra-red image of the lower divertor, showing clear strike-point splitting.

The infra-red measurements used to produce figure 6.13 were taken at a toroidal angle of 19°. The relevant angle in ERGOS co-ordinates with respect to the current sheet is 321° or 5.60 rad. Figure 6.14 (a) is a plot of the length of field lines calculated using field line tracing as described in section 4.2.3. It shows the lower divertor strike-point pattern. The purely $n = 1$ field produced by the current sheet results in a strike-point pattern with just one lobe, although at first glance, it may appear as if there are multiple lobes as produced by the $n = 3$ perturbation in figure 4.7 (a). The lobe in figure 6.14 (a) is much longer than those produced by the ELM coils in section 4.2.3, and is so long that it completes several toroidal turns around the divertor, giving the appearance of multiple lobes. Note that the radial extent of figure 6.14 (a) is 20 cm, whereas that of figure 4.7 (a) is just 5 cm. The radial separation of the lobes (actually the same lobe on a different toroidal turn) in figure 6.14 (a) is several times greater than that of the lobes produced by the ELM coils in section 4.2.3. This may explain why strike-point splitting is more easily observed for locked modes than for RMPs.

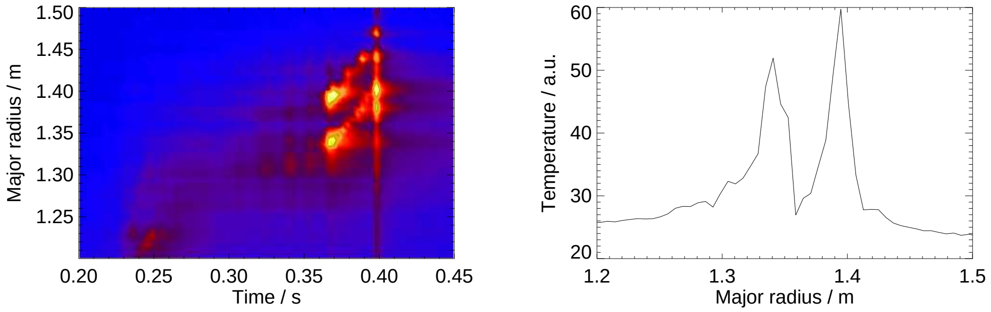

(a) (b)

Figure 6.13 (*a*) Temperature of the lower divertor as a function of major radius and time, calculated from infra-red measurements. (*b*) Radial temperature profile at 369 ms. Clear strike-point splitting can be seen.

The dashed line in figure 6.14 (*a*) marks $\phi = 5.60\,\mathrm{rad}$. Figure 6.14 (*b*) was produced by averaging the field line length profile from $\phi = 5.53\,\mathrm{rad}$ to $\phi = 5.67\,\mathrm{rad}$ in order to smooth out the very fine structure with large fluctuations, as for figure 6.11 (*b*). This is the equivalent of averaging from 15° to 23°. Again, perpendicular transport would be expected to smooth out the effects of very fine magnetic structure in a similar way, and the resolution of the infra-red camera would further smooth out the strike-point pattern. Figure 6.14 (*b*) shows two main peaks around 1.31 m and 1.38 m. These peaks are spaced 2 cm further apart than the peaks in figure 6.13 (*b*) and occur at a slightly lower major radius but show qualitative agreement with the experimental data.

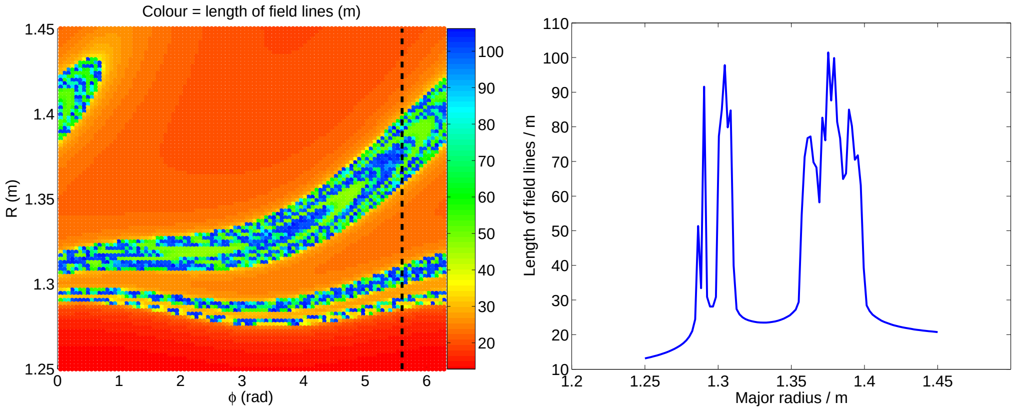

(a) (b)

Figure 6.14 (*a*) Plot of the length of field lines produced by field line tracing, showing a divertor strike-point pattern. The dashed line indicates $\phi = 5.60\,\mathrm{rad}$. (*b*) Field line length profile at $\phi = 5.60\,\mathrm{rad}$ showing peaks at 1.31 m and 1.36 m.

6.6 Flux tubes

Figure 6.15 shows the appearance of flux tubes in the upper divertor leg. If the location of the camera is $(R_{\mathrm{cam}}, \phi_{\mathrm{cam}})$ and the major radius of the strike-point is R_{SP} then the toroidal angle ϕ_{SP} at which the camera images the strike-point is given by

$$\phi_{\mathrm{SP}} = \phi_{\mathrm{cam}} + \arccos\left(\frac{R_{\mathrm{SP}}}{R_{\mathrm{cam}}}\right) \mod 360^\circ. \tag{6.3}$$

Figure 6.13 shows the strike-point to be around $R_{\mathrm{SP}} = 1.35\,\mathrm{m}$. The camera is at $\phi_{\mathrm{cam}} = 345^\circ$ and $R_{\mathrm{cam}} \approx 2\,\mathrm{m}$. Therefore, the angle at which the camera images the strike-point is $\phi_{\mathrm{SP}} = 32.5^\circ$.

Figure 6.6 shows a Poincaré plot taken at 32.5° of the plasma containing the current sheet. 800 field lines were followed for 40 turns. Flux tubes can be seen in the upper and lower outer divertor legs, and there is qualitative agreement between these flux tubes calculated using field line tracing and the ones observed experimentally shown in figure 6.15. Perturbed flux surfaces and a very large magnetic island on the $q = 1$ surface are also visible.

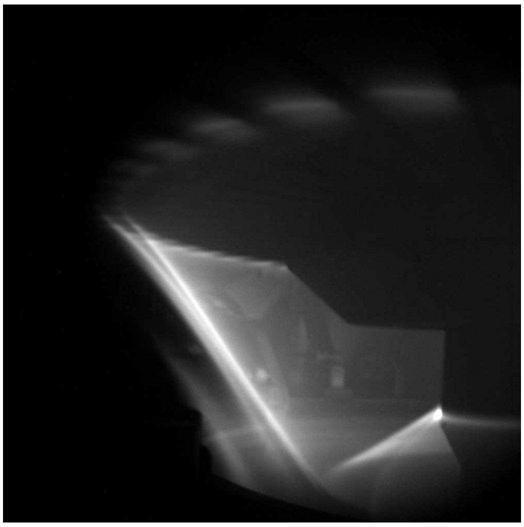

Figure 6.15 Camera image showing flux tubes in the upper divertor leg.

Chapter 7

Conclusion

7.1 Summary

The heat loads due to type-I ELMs on ITER would cause unacceptable damage to the divertor. Therefore, type-I ELMs must be either mitigated or suppressed. One possible way of achieving this is by using resonant magnetic perturbations (RMPs). The application of RMPs can cause the magnetic field in a plasma to become stochastic. In a stochastic field, field lines are no longer confined to flux surfaces, so parallel transport has a radial component and therefore radial transport is significantly enhanced. This could reduce the pedestal pressure gradient below the peeling-ballooning threshold gradient and thus eliminate ELMs. Therefore, RMPs could be used as a form of ELM suppression. On the other hand, RMPs could trigger instabilities in the plasma edge and cause ELMs to occur at lower pressure gradients earlier in the ELM cycle than they would naturally. These triggered ELMs would be smaller and more frequent than natural ELMs, so RMPs could also be used as a form of ELM mitigation.

Stochastic fields and ELM mitigation due to RMPs form the subject of this thesis. Chapter 1 provides an introduction to nuclear fusion and chapter 2 provides an overview of ELMs. In chapter 3, work is presented that relates to stochastic fields in L-mode plasmas. Specifically, the value that the Rechester–Rosenbluth theory predicts for the radial thermal diffusivity χ_r in a stochastized L-mode MAST plasma is calculated and compared with experimental values of χ_r. It was found that the predicted value was less than anomalous experimental values measured in the absence of stochasticity, meaning that no increase in χ_r due to the formation of a stochastic field should be expected. Therefore, no flattening of the temperature profile is predicted, which is in agreement with experimental results.

In chapter 4, various metrics characterizing the degree of stochasticity in both L- and H-mode plasmas were calculated using vacuum modelling and compared with the amount of density pump-out observed in those plasmas when RMPs were applied. None of these metrics provides a single threshold value for pump-out that applies to both L- and H-mode plasmas. The only parameter to show a correlation with the amount of density pump-out is the width of the laminar region, and then only for L-mode plasmas. However, plasma response modelling provides a robust criterion for the occurrence of density pump-out that applies both to L- and H-mode plasmas.

In chapter 5, the results of lower single-null H-mode ELM mitigation experiments using RMPs are presented. ELM mitigation was achieved using both $n = 4$ and $n = 6$ RMPs. Other effects of the RMPs on the plasma, such as density pump-out and rotation braking, were also measured. Refuelling of plasmas that had begun to undergo pump-out was successfully demonstrated and q-scans were performed by varying the toroidal magnetic field. ELM frequency and density pump-out were both found to increase with ELM coil current above a certain threshold.

In chapter 6, a locked mode triggered by RMPs is modelled as a current sheet on a rational surface. The magnetic field produced by the current sheet combines with the background magnetic field to produce a stochastic field. Various properties of this stochastic field are calculated – namely the connection length profile, footprint lobes and the shape of the perturbed separatrix. These properties are compared with experimental effects observed in the plasma – namely multiple peaks in the HFS temperature profile, strike-point splitting and the appearance of flux tubes. A good agreement is found between the experimental data and the modelling.

7.2 Further work

The analysis carried out in chapter 3 could be repeated for a tokamak with hotter plasmas and therefore a longer mean free path in the plasma edge. In that case, it is possible that the predicted value for the radial thermal diffusivity could be greater than the anomalous experimental value and consequently a decrease in the temperature profile would be expected. A comparison with experimentally observed temperature profiles would be interesting.

Chapter 4 highlights the shortcomings of vacuum modelling and the power of plasma response modelling. More plasma response modelling should be carried out firstly to improve predictions as to when ELM mitigation or suppression will occur, secondly to improve understanding of the mechanism behind ELM mitigation and suppression using RMPs, and thirdly to improve understanding of the evolution of mitigated and natural ELMs. Plasma response modelling could also be used to investigate other effects such as rotation braking and the effect that this has on ELM mitigation and suppression. In addition, the field line tracing algorithm used to calculate several of the parameters correlated with density pump-out could be implemented with magnetic fields from MARS-F that include the plasma response.

Finally, ELM mitigation experiments must continue across a range of tokamaks in combination with modelling in preparation for effective mitigation or suppression of ELMs on ITER, which will be essential for ITER to be a success.

Bibliography

[1] MacKay D J C 2008 *Sustainable Energy – without the hot air* (Cambridge: UIT) pp 177–185 ISBN 978-0-9544529-3-3 URL `www.withouthotair.com`

[2] MacKay D J C 2008 *Sustainable Energy – without the hot air* (Cambridge: UIT) pp 235–239 ISBN 978-0-9544529-3-3 URL `www.withouthotair.com`

[3] MacKay D J C 2008 *Sustainable Energy – without the hot air* (Cambridge: UIT) pp 73–75 ISBN 978-0-9544529-3-3 URL `www.withouthotair.com`

[4] Wesson J 2004 *Tokamaks* (Oxford: Oxford University Press) pp 24–25 (*International Series of Monographs on Physics* no 118) 3rd ed ISBN 0-19-850922-7

[5] Wesson J 2004 *Tokamaks* (Oxford: Oxford University Press) p 2 (*International Series of Monographs on Physics* no 118) 3rd ed ISBN 0-19-850922-7

[6] Hamacher T and Bradshaw A M 2001 Fusion as a future power source: recent achievements and prospects *18th World Energy Congress* (Buenos Aires)

[7] Chen F F 1983 *Introduction to Plasma Physics and Controlled Fusion* vol 1 (New York: Springer) pp 3–4 2nd ed ISBN 0-306-41332-9

[8] Chen F F 1983 *Introduction to Plasma Physics and Controlled Fusion* vol 1 (New York: Springer) p 1 2nd ed ISBN 0-306-41332-9

[9] Nemchinsky V A and Severance W S 2006 *J. Phys. D: Appl. Phys.* **39** R423

[10] Chen F F 1983 *Introduction to Plasma Physics and Controlled Fusion* vol 1 (New York: Springer) p 13 2nd ed ISBN 0-306-41332-9

[11] Nardon E 2007 *Edge localized modes control by resonant magnetic perturbations* Ph.D. thesis Ecole Polytechnique and CEA Cadarache URL `www.imprimerie.polytechnique.fr/Theses/Files/Nardon.pdf`

[12] Shimada M *et al.* 2007 *Nucl. Fusion* **47** S1

[13] Wesson J 2004 *Tokamaks* (Oxford: Oxford University Press) p 588 (*International Series of Monographs on Physics* no 118) 3rd ed ISBN 0-19-850922-7

[14] Smith S P 2010 *Magnetohydrodynamic stability spectrum with flow and a resistive wall* Ph.D. thesis Princeton University URL `www.grin.com/en/doc/243356/magnetohydrodynamic-stability-spectrum-with-flow-and-a-resistive-wall`

[15] Wesson J 2004 *Tokamaks* (Oxford: Oxford University Press) p 186 (*International Series of Monographs on Physics* no 118) 3rd ed ISBN 0-19-850922-7

[16] Bécoulet M *et al.* 2003 *Plasma Phys. Control. Fusion* **45** A93

[17] Connor J W 1998 *Plasma Phys. Control. Fusion* **40** 531

[18] Suttrop W 2000 *Plasma Phys. Control. Fusion* **42** A1

[19] Wesson J 2004 *Tokamaks* (Oxford: Oxford University Press) p 58 (*International Series of Monographs on Physics* no 118) 3rd ed ISBN 0-19-850922-7

[20] Wesson J 2004 *Tokamaks* (Oxford: Oxford University Press) p 79 (*International Series of Monographs on Physics* no 118) 3rd ed ISBN 0-19-850922-7

[21] Chen F F 1983 *Introduction to Plasma Physics and Controlled Fusion* vol 1 (New York: Springer) pp 58–68 2nd ed ISBN 0-306-41332-9

[22] Chen F F 1983 *Introduction to Plasma Physics and Controlled Fusion* vol 1 (New York: Springer) pp 184–186 2nd ed ISBN 0-306-41332-9

[23] Freidberg J P *Ideal Magnetohydrodynamics* (New York and London: Plenum Press) pp 21–22

[24] Chen F F 1983 *Introduction to Plasma Physics and Controlled Fusion* vol 1 (New York: Springer) p 179 2nd ed ISBN 0-306-41332-9

[25] Wesson J 2004 *Tokamaks* (Oxford: Oxford University Press) p 306 (*International Series of Monographs on Physics* no 118) 3rd ed ISBN 0-19-850922-7

[26] Wesson J 2004 *Tokamaks* (Oxford: Oxford University Press) pp 309–311 (*International Series of Monographs on Physics* no 118) 3rd ed ISBN 0-19-850922-7

[27] Huysmans G T A 2005 *Plasma Phys. Control. Fusion* **47** B165

[28] Snyder P B, Wilson H R, Ferron J R, Lao L L, Leonard A W, Mossessian D, Murakami M, Osborne T H, Turnbull A D and Xu X Q 2004 *Nucl. Fusion* **44** 320

[29] Eisberg R and Resnick R 1985 *Quantum Physics of Atoms, Molecules, Solids, Nuclei, and Particles* 2nd ed (John Wiley & Sons)

[30] Kamiya K *et al.* 2007 *Plasma Phys. Control. Fusion* **49** S43

[31] Zohm H 1996 *Plasma Phys. Control. Fusion* **38** 105

[32] Doyle E J, Groebner R J, Burrell K H, Gohil P, Lehecka T, Luhmann Jr N C, Matsumoto H, Osborne T H, Peebles W A and Philipona R 1991 *Phys. Fluids B* **3** 2300

[33] Bécoulet M *et al.* 2005 *Nucl. Fusion* **45** 1284

[34] Lang P T *et al.* 2004 *Nucl. Fusion* **44** 665

[35] Lang P T *et al.* 2006 *Czech. J. Phys.* **56** 12

[36] Maingi R *et al.* 2009 *Phys. Rev. Lett.* **103** 075001

[37] Wesson J 2004 *Tokamaks* (Oxford: Oxford University Press) p 108 (*International Series of Monographs on Physics* no 118) 3rd ed ISBN 0-19-850922-7

[38] Nardon E, Bécoulet M, Huysmans G and Czarny O 2007 *Phys. Plasmas* **14** 092501

[39] Evans T E *et al.* 2004 *Phys. Rev. Lett.* **92** 235003

[40] Evans T E *et al.* 2008 *Nucl. Fusion* **48** 024002

[41] Liang Y *et al.* 2007 *Phys. Rev. Lett.* **98** 265004

[42] Liang Y *et al.* 2010 *Nucl. Fusion* **50** 025013

[43] Suttrop W *et al.* 2011 *Phys. Rev. Lett.* **106** 225004

[44] Kirk A *et al.* 2010 *Nucl. Fusion* **50** 034008

[45] Kirk A *et al.* 2011 *Plasma Phys. Control. Fusion* **53** 065011

[46] Tamain P, Kirk A, Nardon E, Dudson B, Hnat B and the MAST team 2010 *Plasma Phys. Control. Fusion* **52** 075017

[47] Nardon E *et al.* 2007 *J. Nucl. Mater.* **363–365** 1071–1075

[48] Lao L L, St John H, Stambaugh R D, Kellman A G and Pfeiffer W 1985 *Nucl. Fusion* **25** 11

[49] Rechester A B, Rosenbluth M N and White R B 1979 *Phys. Rev. Lett.* **42** 1247

[50] Rechester A B and Rosenbluth M N 1978 *Phys. Rev. Lett.* **40** 38

[51] Wesson J 1987 *Tokamaks* (Oxford: Oxford University Press) p 84 (*Oxford Engineering Science Series* no 20) 1st ed ISBN 0-19-856328-0

[52] Wesson J 2004 *Tokamaks* (Oxford: Oxford University Press) p 733 (*International Series of Monographs on Physics* no 118) 3rd ed ISBN 0-19-850922-7

[53] Fenstermacher M E *et al.* 2008 *Phys. Plasmas* **15** 056122

[54] Mikhailovskii A B, Huysmans G T A, Sharapov S E and Kerner W O K 1997 *Plasma Phys. Rep.* **23** 844

[55] Wesson J 1987 *Tokamaks* (Oxford: Oxford University Press) p 74 (*Oxford Engineering Science Series* no 20) 1st ed ISBN 0-19-856328-0

[56] Wesson J 1987 *Tokamaks* (Oxford: Oxford University Press) p 94 (*Oxford Engineering Science Series* no 20) 1st ed ISBN 0-19-856328-0

[57] Nardon E *et al.* 2009 *J. Nucl. Mater.* **390–391** 773–776

[58] Abdullaev S S, Jakubowski M, Lehnen M, Schmitz O and Unterberg B 2008 *Phys. Plasmas* **15** 042508

[59] Schmitz O *et al.* 2008 *Plasma Phys. Control. Fusion* **50** 124029

[60] Mordijck S, Owen L W and Moyer R A 2010 *Nucl. Fusion* **50** 034006

[61] Liu Y Q, Kirk A and Nardon E 2010 *Phys. Plasmas* **17** 122502

[62] Liu Y Q, Kirk A, Gribov Y, Gryaznevich M P, Hender T C and Nardon E 2011 *Nucl. Fusion* **51** 083002

[63] Nardon E, Tamain P, Bécoulet M, Huysmans G and Waelbroeck F L 2010 *Nucl. Fusion* **50** 034002

[64] Liu Y Q *et al. to be published in Plasma Phys. Control. Fusion*

[65] Thornton A J, Kirk A, Chapman I T, Harrison J R and the MAST team *to be published in J. Nucl. Mater.*

[66] Kirk A *et al. submitted to Plasma Phys. Control. Fusion*

[67] Howell D F, Hender T C and Cunningham G 2007 *Nucl. Fusion* **47** 1336

[68] Wingen A, Evans T E and Spatschek K H 2009 *Nucl. Fusion* **49** 055027

[69] Schmitz O *et al.* 2008 *Nucl. Fusion* **48** 024009